ELEMENTA
Science of the Anthropocene

Ahmed, S, et al. 2023. Modelling the coupled mercury-halogen-ozone cycle in the central Arctic during spring. *Elem Sci Anth*, 11: 1. DOI: https://doi.org/10.1525/elementa.2022.00129

RESEARCH ARTICLE

Modelling the coupled mercury-halogen-ozone cycle in the central Arctic during spring

Shaddy Ahmed[1,*], Jennie L. Thomas[1,*], Hélène Angot[1,2,3], Aurélien Dommergue[1], Stephen D. Archer[4], Ludovic Bariteau[5,6], Ivo Beck[2], Nuria Benavent[7], Anne-Marlene Blechschmidt[8], Byron Blomquist[5,6], Matthew Boyer[9], Jesper H. Christensen[10], Sandro Dahlke[11], Ashu Dastoor[12], Detlev Helmig[3,13], Dean Howard[3,5,6], Hans-Werner Jacobi[1], Tuija Jokinen[9,14], Rémy Lapere[1], Tiia Laurila[9], Lauriane L. J. Quéléver[9], Andreas Richter[8], Andrei Ryjkov[12], Anoop S. Mahajan[15], Louis Marelle[16], Katrine Aspmo Pfaffhuber[17], Kevin Posman[4], Annette Rinke[11], Alfonso Saiz-Lopez[7], Julia Schmale[2], Henrik Skov[10], Alexandra Steffen[18], Geoff Stupple[18], Jochen Stutz[19], Oleg Travnikov[20], and Bianca Zilker[8]

Near-surface mercury and ozone depletion events occur in the lowest part of the atmosphere during Arctic spring. Mercury depletion is the first step in a process that transforms long-lived elemental mercury to more reactive forms within the Arctic that are deposited to the cryosphere, ocean, and other surfaces, which can ultimately get integrated into the Arctic food web. Depletion of both mercury and ozone occur due to the presence of reactive halogen radicals that are released from snow, ice, and aerosols. In this work, we added a detailed description of the Arctic atmospheric mercury cycle to our recently published version of the Weather Research and Forecasting model coupled with Chemistry (WRF-Chem 4.3.3) that includes Arctic bromine and chlorine chemistry and activation/recycling on snow and aerosols. The major advantage of our modelling approach is the online calculation of bromine concentrations and emission/recycling that is required to simulate the hourly and daily variability of Arctic mercury depletion. We used this model to study coupling between reactive cycling of mercury, ozone, and bromine during the Multidisciplinary drifting Observatory for the Study of Arctic Climate (MOSAiC) spring season in 2020 and evaluated results compared to land-based, ship-based, and remote sensing observations. The model predicts that elemental mercury oxidation is driven largely by bromine chemistry and that particulate mercury is the major form of oxidized mercury. The model predicts that the majority (74%) of oxidized mercury deposited to land-based snow is re-emitted to the atmosphere as gaseous elemental mercury, while a minor fraction (4%) of oxidized mercury that is deposited

[1] Université Grenoble Alpes, CNRS, IRD, Grenoble INP, IGE, Grenoble, France
[2] Extreme Environments Research Laboratory, Ecole Polytechnique Federale de Lausanne (EPFL) Valais Wallis, Sion, Switzerland
[3] Institute of Arctic and Alpine Research, University of Colorado, Boulder, CO, USA
[4] Bigelow Laboratory for Ocean Sciences, East Boothbay, ME, USA
[5] Cooperative Institute for Research in Environmental Sciences, University of Colorado, Boulder, CO, USA
[6] NOAA, Physical Sciences Laboratory, Boulder, CO, USA
[7] Department of Atmospheric Chemistry and Climate, Institute of Physical Chemistry Rocasolano, CSIC, Madrid, Spain
[8] Institute of Environmental Physics, University of Bremen, Bremen, Germany
[9] Institute for Atmospheric and Earth System Research/INAR-Physics, Faculty of Science, University of Helsinki, Helsinki, Finland
[10] Department of Environmental Science, iClimate, Aarhus University, Roskilde, Denmark
[11] Alfred Wegener Institute (AWI), Helmholtz Centre for Polar and Marine Research, Potsdam, Germany
[12] Air Quality Research Division, Environment and Climate Change Canada, Dorval, Quebec, Canada
[13] Current address: Boulder AIR, Boulder, CO, USA
[14] Climate and Atmosphere Research Centre (CARE-C), The Cyprus Institute, Nicosia, Cyprus
[15] Indian Institute of Tropical Meteorology, Ministry of Earth Sciences, Pune, India
[16] LATMOS/IPSL, Sorbonne Université, UVSQ, CNRS, Paris, France
[17] NILU–Norwegian Institute for Air Research, Kjeller, Norway
[18] Environment and Climate Change Canada, Toronto, Ontario, Canada
[19] Department of Atmospheric and Oceanic Sciences, University of California, Los Angeles, CA, USA
[20] Meteorology Synthesizing Centre-East, EMEP, Moscow, Russia

* Corresponding authors:
Email: shaddy.ahmed@univ-grenoble-alpes.fr; jennie.thomas@univ-grenoble-alpes.fr

to sea ice is re-emitted during spring. Our work demonstrates that hourly differences in bromine/ozone chemistry in the atmosphere must be considered to capture the springtime Arctic mercury cycle, including its integration into the cryosphere and ocean.

Keywords: Arctic, Ozone, Mercury, Bromine, Cryosphere, Atmosphere

1. Introduction

Each spring halogens released from snow, sea ice, and sea salt aerosols cause the depletion of boundary layer ozone (O_3) and mercury (Hg) in the Arctic (Oltmans, 1981; Barrie, 1986; Barrie et al., 1988; Bottenheim et al., 1990; Schroeder et al., 1998; Lindberg et al., 2001; Skov et al., 2004; Simpson et al., 2007; Abbatt et al., 2012; Wang et al., 2019). Depletion occurs when halogens and other radicals in the atmosphere oxidize elemental mercury, Hg(0) to Hg(II), which is much shorter-lived and is taken up directly onto aerosols, snow, ice and the open ocean (Selin, 2009; Douglas et al., 2012). Oxidized mercury present in particles is also removed to ice, snow, and the ocean via both wet and dry deposition. Once deposited to the Arctic Ocean, mercury can undergo transformation to more toxic forms, including methylmercury, that are harmful to ecosystems and human health (Driscoll et al., 2013). The main form of atmospheric Hg is long-lived, gaseous Hg(0), emitted from both anthropogenic (e.g., coal burning and artisanal gold mines) and natural sources (e.g., volcanoes; Lindberg and Stratton, 1998; Arctic Monitoring and Assessment Programme [AMAP], 2011). Anthropogenic Hg sources in the Arctic are estimated to be less than 1% of global Hg emissions to air, with most Arctic Hg(0) originally from emissions from distant sources (Durnford et al., 2010; Skov et al., 2020; Dastoor et al., 2022b). Understanding the fate of Arctic Hg that involves air-surface exchange processes remains a challenge, including integration of mercury from the atmosphere into the cryosphere and ocean, storage of oxidized mercury in snow and ice, and photochemical re-emissions of mercury back to the atmosphere.

Developing models that describe diurnal variation and cycling of mercury in the lowest part of the Arctic atmosphere has remained a challenge because of the complexity of chemical and physical processes involved. In addition, closely coupled chemical cycles, such as halogens, have recently been improved within Arctic atmospheric models (e.g., Yang et al., 2008; Yang et al., 2010; Toyota et al., 2011; Falk and Sinnhuber, 2018; Fernandez et al., 2019; Yang et al., 2019; Marelle et al., 2021; Herrmann et al., 2022; Swanson et al., 2022). **Figure 1** illustrates the main chemical processes of Hg in the Arctic boundary layer. During atmospheric mercury depletion events (AMDEs), Hg(0) is oxidized forming gaseous oxidized mercury, Hg(II), and particulate mercury species, Hg(p), which are deposited to the cryosphere via dry and wet processes (Lindqvist and Rodhe, 1985; Brooks et al., 2006; Skov et al., 2006; Ariya et al., 2015). AMDEs are linked to high concentrations of reactive bromine (e.g., Br_2, Br, BrO, HOBr, and $BrONO_2$), activated from trace amounts of oceanic bromide on snow and ice surfaces (Lu et al., 2001; Brooks et al., 2006; Sommar et al., 2007; Stephens et al., 2012; Wang et al., 2019). This process occurs simultaneously with the well-studied depletion of surface ozone, known as ozone depletion events (e.g., ODEs; Barrie et al., 1988; Platt and Hönninger, 2003; Simpson et al., 2007; Abbatt et al., 2012; Simpson et al., 2015). Upon deposition of Hg to snow, a fraction can be photoreduced and re-emitted back into the atmosphere as Hg(0) (e.g., Poulain et al., 2004; Brooks et al., 2006; Kirk et al., 2006; Skov et al., 2006; Sommar et al., 2007; Ferrari et al., 2008; Dommergue et al., 2010; Durnford and Dastoor, 2011; Steffen et al., 2013; Douglas and Blum, 2019). Chemical transformation between Hg(0), Hg(II), and Hg(p) can occur rapidly and is driven by several factors including oxidant and aerosol concentrations, air temperature, and solar radiation (Ariya et al., 2015). Currently, many models are limited in capturing the behaviour of Hg in Arctic spring due to: (1) uncertainties in the mercury chemical mechanism; (2) use of offline-calculated oxidant concentrations including reactive bromine; (3) a lack of detailed halogen chemistry/emission processes over snow and sea ice; and/or (4) poorly represented Arctic boundary layer meteorology (Angot et al., 2016; Travnikov et al., 2017).

Bromine is a central species in Arctic O_3 and Hg(0) depletion and is considered to be the major oxidant driving AMDEs (Wang et al., 2019). Elevated Br concentrations in the Arctic are known to occur due to the uptake and emission of reactive bromine on surfaces, which occurs via an autocatalytic process on snow, ice, and aerosols known as the "bromine explosion" (Simpson et al., 2007; Simpson et al., 2015). Two main bromine activation mechanisms in the Arctic have been proposed and tested in 3D chemical transport models. The first method, proposed by Toyota et al. (2011), involves the activation of bromide in the top layer of the snowpack, triggered by ozone deposition or heterogeneous recycling of HOBr and $BrONO_2$ (Toyota et al., 2011; Falk and Sinnhuber, 2018; Fernandez et al., 2019; Herrmann et al., 2021; Marelle et al., 2021; Swanson et al., 2022). The second method involves the release of bromine from sea salt aerosols (SSA), formed via sublimation of lofted blowing snow (as proposed by Yang et al., 2008; Yang et al., 2010; Huang and Jaeglé, 2017; Rhodes et al., 2017; Huang et al., 2018; Yang et al., 2019; Huang et al., 2020; Yang et al., 2020). As both mechanisms have important impacts on reactive bromine and ozone concentrations in the Arctic, they need to be considered in models for springtime chemistry.

Descriptions of mercury in models often differ in their treatment of physical and chemical processes, partly due to current knowledge gaps (Ariya et al., 2015). Multimodel intercomparisons are therefore useful to assess the

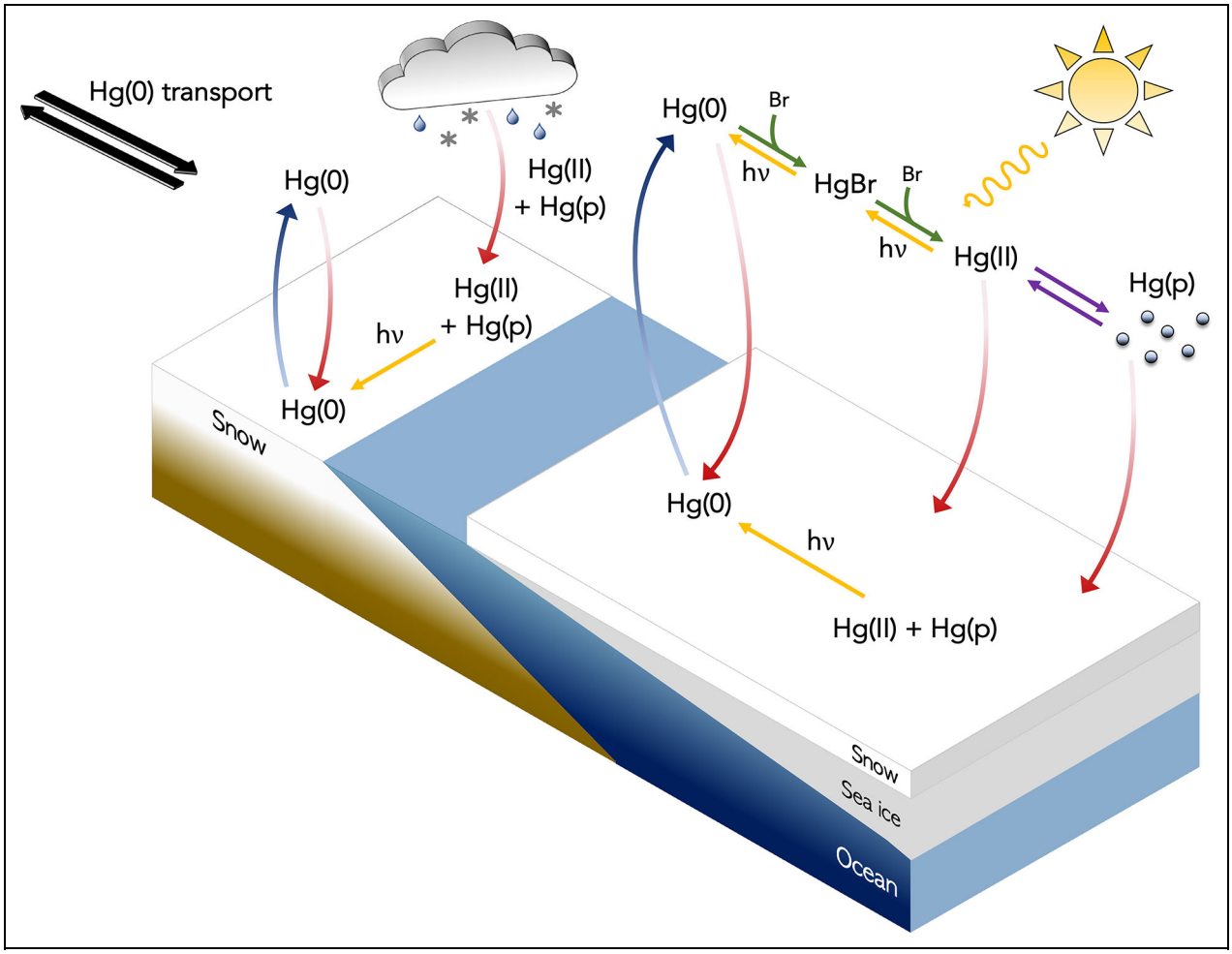

Figure 1. Overview schematic of Arctic mercury chemical processes represented in the model WRF-Chem 4.3.3. Hg(0) denotes gaseous elemental mercury, Hg(II) is gaseous oxidized mercury, and Hg(p) represents particulate mercury.

impacts of different model parameterizations on the behaviour of atmospheric Hg (Angot et al., 2016; Travnikov et al., 2017; Dastoor et al., 2022a). Arctic-focused model intercomparisons have shown that several models are capable of simulating the seasonality in surface Hg(0) concentrations (spring minima and summer maxima); however, they can underestimate the amplitude of the seasonal variation (Angot et al., 2016; Dastoor et al., 2022a). Several factors are likely to contribute to this disparity, which underscores some of the limitations of current global models. First, most global models that include Hg chemistry use monthly averaged oxidant fields to simulate Hg(0) oxidation (Holmes et al., 2010; Durnford et al., 2012; Song et al., 2015; Horowitz et al., 2017; Shah et al., 2021). For the purpose of studying springtime mercury chemistry, this approach is inadequate as it neglects the diurnal variability of oxidants, including bromine, in the Arctic (Angot et al., 2016). Secondly, the low spatial and temporal resolution of global models may not sufficiently resolve the local chemistry and emissions occurring that contribute to AMDEs during spring (Toyota et al., 2014). Bromine production mechanisms from snow and sea ice, which are crucial for polar atmospheric chemistry, can therefore be inaccurately represented. In comparison to global models, regional models are computationally less expensive at high spatial resolution and can calculate oxidant concentrations online, making them ideal tools for studying AMDEs.

We recently updated our Arctic-specific version of the regional Weather Research and Forecasting model coupled with Chemistry (WRF-Chem) model (Marelle et al., 2021) to include the atmospheric mercury cycle described in Shah et al. (2021). This version of WRF-Chem 4.3.3 currently includes detailed bromine emissions from both Arctic surface snow and blowing snow, previously shown to improve model representation of Arctic ODEs (Marelle et al., 2021). In this dedicated Arctic study, we investigated the impacts of polar bromine activation on springtime Hg and O_3 chemistry and depletion, during spring 2020. To evaluate the model, we compared with data from Arctic stations and from the central Arctic obtained on board the Research Vessel (RV) *Polarstern* during the Multidisciplinary drifting Observatory for the Study of Arctic Climate (MOSAiC) campaign in spring 2020 (Shupe et al., 2022). The new mercury developments and WRF-Chem model setup are presented in Section 2, with the observations used to evaluate the model described in Section 3. In Section 4, we evaluate the model against meteorological and chemical observations

Table 1. Modelled tropospheric Hg budget during the simulation period (March 14 to April 14, 2020)

Species	Budget (Mg)	Contribution (%)[a]
Hg(0)	927	95.6
Hg(I)	1.34×10^{-4}	<0.1 (100)
HgBr	9.69×10^{-5}	72.3
HgBrO	2.49×10^{-5}	18.6
HgOHO	8.94×10^{-6}	6.7
HgOH	3.34×10^{-6}	2.5
HgClO	2.98×10^{-9}	<0.1
HgCl	2.50×10^{-9}	<0.1
Hg(II)	42.8	4.4 (100)
Hg(p)	27.1	63.2
HgX[b]	15.0	35.1
HgOHOH	0.567	1.3
HgBrOH	0.165	0.4
HgBrBrO	1.44×10^{-3}	<0.1
$HgBr_2$	1.35×10^{-3}	<0.1
HgBrClO	1.90×10^{-4}	<0.1
HgBrCl	2.01×10^{-4}	<0.1
HgClClO	1.78×10^{-4}	<0.1
HgOHClO	1.42×10^{-4}	<0.1
HgClOH	1.28×10^{-4}	<0.1
$HgBrNO_2$	9.10×10^{-5}	<0.1
HgOHBrO	6.68×10^{-5}	<0.1
HgClBrO	6.41×10^{-5}	<0.1
$HgBrHO_2$	5.63×10^{-5}	<0.1
$HgOHNO_2$	5.54×10^{-5}	<0.1
$HgClNO_2$	5.53×10^{-5}	<0.1
$HgClHO_2$	4.43×10^{-5}	<0.1
$HgOHHO_2$	4.06×10^{-5}	<0.1
Total	970	100

[a]Percent contributions of each Hg(I) and Hg(II) species are represented as a fraction of the total Hg(I) and Hg(II) budget.

[b]HgX denotes gas-phase Hg(II) volatilized from Hg(p) (treated as $HgCl_2$ in the model).

from MOSAiC. In Section 5, we assess the model performance compared to other Arctic observations, as well as discuss the simulated pan-Arctic impacts. Finally, the outcomes and conclusions are presented in Section 6.

2. WRF-Chem model

2.1. Implementation of mercury chemistry in WRF-Chem

We extended the work of Marelle et al. (2021) by including Hg gas-phase chemistry and photolysis (Section 2.1.1), heterogeneous uptake to aerosols and clouds (Section 2.1.2), dry and wet deposition processes (Section 2.1.3), and Hg(0) re-emission from continental snow and snow on sea ice (Section 2.1.4). These updates are based largely on the latest developments in other Hg chemical transport models (e.g., Holmes et al., 2010; Amos et al., 2012; Fisher et al., 2012; Fisher et al., 2013; Gencarelli et al., 2014; Horowitz et al., 2017; Shah et al., 2021), which were implemented in the WRF-Chem model here. The model developments presented in this study are publicly available as Ahmed et al. (2022).

2.1.1. Hg gas-phase chemistry and photoreduction

Atmospheric Hg(0) oxidation is understood to proceed via several pathways; however, the relative importance of each oxidant on the global Hg budget remains a subject of debate (Subir et al., 2011; Ariya et al., 2015). Determining the kinetics and speciation of oxidized mercury is an ongoing analytical challenge due to very low atmospheric Hg(II) concentrations (picograms per cubic meter) and limitations in instrument sensitivity (Hynes et al., 2009; Subir et al., 2011). Here, we included gas-phase oxidation of Hg(0) via Br, Cl, and OH to the Statewide Air Pollution Research Center, 1999 version (SAPRC-99; Carter, 2000) chemical mechanism in WRF-Chem, following the chemistry scheme of Shah et al. (2021). We have used the SAPRC-99 chemical mechanism for this study due to the demonstrated performance of this setup for Arctic ozone inland (see Figure 15 from Petäjä et al., 2020) and during bromine-mediated ozone depletion events (see Figures 3 and 4 from Marelle et al., 2021). Chemical concentrations (including oxidants such as OH and Br) are calculated online in the WRF-Chem model. Hg gas-phase reactions are added to a previously developed chemical mechanism (Marelle et al., 2021), which includes chlorine and bromine gas-phase chemistry, using the Kinetic PreProcessor (KPP, Sandu and Sander, 2006). Hg(0) oxidation is treated as a two-step process, first forming a Hg(I) intermediate, which can be reduced to Hg(0) (via photoreduction or thermal dissociation) before undergoing further oxidation to Hg(II) (Goodsite et al., 2004, 2012). All oxidized Hg species included in the model are listed in **Table 1** (column 1).

The role of atmospheric Hg(II) reduction in the global Hg cycle is also uncertain, as rate constants are based largely on theoretical estimates yet to be verified experimentally (Goodsite et al., 2004; Balabanov et al., 2005; Dibble et al., 2012; Goodsite et al., 2012; Saiz-Lopez et al., 2018; Saiz-Lopez et al., 2019; Sitkiewicz et al., 2019; Dibble et al., 2020; Francés-Monerris et al., 2020; Khiri et al., 2020; Gómez Martn et al., 2022). Recent modelling studies have shown that atmospheric Hg(II) reduction must be considered in models to match observational estimates of total gaseous mercury lifetime against deposition (Horowitz et al., 2017; Shah et al., 2021; Zhang and Zhang, 2022). We therefore added to WRF-Chem photoreduction reactions of Hg(I) and Hg(II) species, following the implementation of Shah et al. (2021). Photochemical rates were calculated, using the FastJ photolysis scheme in WRF-Chem (Wild et al., 2000), from computationally

derived quantum yields (ϕ) and absorption cross sections (σ) of Hg(I) and Hg(II) species. For Hg(I), we used $\phi = 0$ for non-dissociative transitions in the wavelength range of 270–460 nm, and $\phi = 1$ for transitions in the 460–800 nm range, as in Saiz-Lopez et al. (2019). Values of σ for Hg(I) species were also taken from Saiz-Lopez et al. (2019). For Hg(II), values of ϕ were taken from Francés-Monerris et al. (2020) and σ values were taken from Saiz-Lopez et al. (2018). We did not include the photoreduction of Hg(p) as the rate of this reaction remains highly uncertain.

2.1.2. Heterogeneous uptake and gas-particle partitioning

Surface uptake of gas-phase Hg(II) onto aerosols and clouds is an important process for the formation of Hg(p) in the Arctic, particularly during spring (Steffen et al., 2013; Steffen et al., 2014). Uptake and volatilization of Hg(II) to/from surfaces is a complex process influenced by several variables including temperature, fine particle concentration, and aerosol chemical composition (Subir et al., 2012). We used a parameterized approach to represent Hg heterogeneous chemistry in WRF-Chem, using the 8-bin sectional aerosol scheme MOSAIC (Model for Simulating Aerosol Interactions and Chemistry, not related to the MOSAiC expedition) (Zaveri et al., 2008). We included the heterogeneous uptake of all Hg(II) species onto aerosols and liquid clouds. This process is treated as a kinetic process with the uptake rate, k_{het}, calculated for each aerosol size bin and summed to obtain a total heterogeneous uptake rate, following Equation 1 (Schwartz, 1986; Jacob, 2000):

$$k_{\text{het}} = \sum_{i}^{n=8} A_i \left(\frac{r_i}{D_g} + \frac{4}{\nu\alpha} \right)^{-1} \quad (1)$$

where k_{het} is the total reactive uptake rate (s^{-1}), A_i and r_i are the effective mean aerosol surface area (cm^2/cm^3_{air}) and aerosol radius (cm) for aerosols in size bin i, D_g is the diffusion coefficient ($cm^2\ s^{-1}$), ν is the mean molecular speed (cm s^{-1}) and α is the mass accommodation coefficient (unitless). We assumed $\alpha = 0.1$ for uptake of all Hg(II) species onto aerosols and liquid clouds, following Shah et al. (2021). For liquid clouds, we calculated the uptake rate in a similar way to Equation 1, using the average cloud droplet surface area and radius for A and r, respectively (see Figure S1 for average modelled surface values). For computational efficiency, Hg(p) was not explicitly modelled in the aerosol-phase and was treated here as an additional gas-phase species.

We also included the conversion of Hg(p) on aerosols back to gas-phase Hg(II) via volatilization. This process is parameterized based on the empirical gas-particle equilibrium of Amos et al. (2012) and is considered only for fine-mode aerosols ($\leq 2.5\ \mu$m), corresponding to the first 6 MOSAIC aerosol size bins. This empirical equilibrium, described by Amos et al. (2012), defines the ratio of Hg(II) and Hg(p) available as a function of particulate matter ($PM_{2.5}$) concentration and air temperature. Volatilized Hg(II) gas, denoted as HgX, is treated in the model as $HgCl_2$, which does not photolyze at tropospheric wavelengths (Saiz-Lopez et al., 2018).

2.1.3. Dry and wet deposition of mercury

The transformation between Hg(0), Hg(II), and Hg(p) has important consequences on the dry and wet deposition rates of Hg over the Arctic (Zhang et al., 2009). We included dry deposition for the added Hg species, Hg(0), Hg(II), and Hg(p), excluding Hg(I) species as they are thermally unstable and short-lived intermediates. Dry deposition of Hg(0) is calculated based on the Wesley resistance scheme (Wesely, 1989) and is implemented using four species-specific parameters: the Henry's law constant (H^*); the Henry's law temperature correction factor (DHR); a surface reactivity factor (f_0); and the molecular diffusivity (dvj). For Hg(0), we used values of $H^* = 0.11$ mol m^{-3} hPa^{-1} and DHR = 4800 K from Clever et al. (1985), $f_0 = 1.0 \times 10^{-5}$ from Selin et al. (2008), and dvj = 0.071 cm^{-2} s^{-1} based on the inverse square root of the molar mass of Hg(0). Henry's law constants for Hg(II) species are less well known, and so we assumed a dry deposition velocity of 0.1 cm s^{-1} for all Hg(II) species based on estimates of reactive gaseous mercury dry deposition to ice surfaces (Lindberg et al., 2002; Skov et al., 2006; Zhang et al., 2009). Measurements of the dry deposition velocity of Hg(p) currently remain limited; however, previous results have shown that Hg(p) deposits several times slower than Hg(II) (Poissant et al., 2004; Zhang et al., 2012). We therefore assumed a dry deposition velocity of 0.01 cm s^{-1} for Hg(p), but we note that this assumption should be revised in future work as more measurements become available.

We also added to the model wet removal of Hg(II) and Hg(p) considering both in-cloud (washout) and below-cloud (rainout) scavenging. Hg(II) is highly soluble; however, the Henry's law constants for each individual species remain relatively unknown. We therefore assumed the wet scavenging rates of Hg(II) and Hg(p) to be equal to that of HNO_3, based on similarities in solubility and on previous Hg modelling work (Seigneur et al., 2004; Gencarelli et al., 2014). This assumption is an imperfect simplification and should be revised in future developments of the model.

2.1.4. Hg(0) re-emission from snow and sea ice

The fate of deposited Hg(II) to the Arctic snowpack remains a major scientific question, with reported Hg(0) re-emission ranging between 40% and 90% of deposited Hg(II) during AMDEs (Lalonde et al., 2002; Poulain et al., 2004; Brooks et al., 2006; Kirk et al., 2006; Skov et al., 2006; Sommar et al., 2007; Ferrari et al., 2008; Dommergue et al., 2010; Durnford and Dastoor, 2011; Steffen et al., 2013; Douglas and Blum, 2019). The amount of Hg(0) re-emitted can depend on several factors including the chemical composition of snow, the amount of solar radiation, snow temperature, liquid water content of snow, and snowpack ventilation and gas transport (Steffen et al., 2002; Lalonde et al., 2003; Poulain et al., 2004; Ferrari et al., 2005; Dommergue et al., 2007; Steffen et al., 2013; Mann et al., 2015a; Mann et al., 2015b; Mann et al., 2018). Here, we added a description of Hg(0) re-emission from both land-based snow and snow on sea ice. Total reactive

mercury (RM), where RM = Hg(II) + Hg(p), that has been deposited to the snow surface is tracked in the model and stored as a surface reservoir. We assumed 60% of deposited RM at the surface is photoreducible and available for re-emission under sunlit conditions, following Holmes et al. (2010) and Fisher et al. (2012). The sensitivity of this value was tested by performing a simulation with 100% of RM in snow available for re-emission. The rate of Hg(0) re-emission from land-based snow and snow on sea ice is parameterized in the model following Equations 2 and 3, respectively:

$$R_{Hg^0}^{snow} = k_{red}^{snow} \times \cos(SZA) \times f_{snow} \quad (2)$$

$$R_{Hg^0}^{sea\ ice} = k_{red}^{sea\ ice} \times \cos(SZA) \times f_{sea\ ice} \quad (3)$$

where $R_{Hg^0}^{snow}$ and $R_{Hg^0}^{sea\ ice}$ are the rates of Hg(0) re-emission (s^{-1}) from land-based snow and snow on sea ice, respectively; k_{red}^{snow} and $k_{red}^{sea\ ice}$ are the net reduction rate constants of RM (s^{-1}) from land-based snow and snow on sea ice, respectively; cos(SZA) is the cosine of the solar zenith angle (dimensionless); and f_{snow} and $f_{sea\ ice}$ are the fractions of each grid cell (0 − 1, dimensionless) covered by snow or sea ice, respectively. For land-based snow, we used $k_{red}^{snow} = 2.5 \times 10^{-5}\ s^{-1}$ (0.09 h^{-1}), following Poulain et al. (2004), and for snow on sea ice we assumed a lower value of $k_{red}^{sea\ ice} = 2.8 \times 10^{-7}\ s^{-1}$ (0.001 h^{-1}) based on a mid-range value from observational estimates (Durnford and Dastoor, 2011), following Fisher et al. (2012). Current estimates of k_{red} in Arctic snow samples have a large variability, with reported values ranging from 7×10^{-6} to 0.6 h^{-1} (Poulain et al., 2004; Dommergue et al., 2007; Mann et al., 2015b; Mann et al., 2018). Part of this variability can be explained by differences in measurement techniques, with some values reporting gross Hg(II) photoreduction rate constants, thereby neglecting the effects of in-snow Hg(0) oxidation (e.g., Mann et al., 2015b; Mann et al., 2018). The values of k_{red} used here are therefore tentative estimates to be examined further in future studies. A temperature dependence was applied for Hg(0) re-emissions, where re-emission is only active for snow-covered grid cells with a skin temperature below 0°C. We also applied a fractional sea ice cutoff of 75% for Hg(0) re-emission, in which grid cells below this sea ice threshold do not re-emit Hg(0), following similar descriptions of Br_2 emissions in Marelle et al. (2021).

2.2. Model setup

2.2.1. Model domain and simulation period

We set up the model for the dates between March 1 and April 14, 2020, during leg 3 of the MOSAiC expedition. In mid- to late April 2020, warm air intrusions were observed reaching the *Polarstern*, transporting pollution from southern latitudes to the central Arctic (Dada et al., 2022). We therefore excluded this period from our model simulation as these events require a detailed evaluation of pollution transport which is beyond the scope of this study. The first 2 weeks of model output are considered spin-up and are not included in the analysis (see Section 4.2). A horizontal resolution of 100 × 100 km is used to encompass the entire Arctic (model domain shown in **Figure 2**) with a vertical resolution of 72 levels up to a pressure of 50 hPa. Details about the model setup are given below and are selected based on extensive testing for the Arctic from previous studies (Marelle et al., 2017; Marelle et al., 2021). A summary of the specific model chemistry and physics options selected are given in **Table 2**.

2.2.2. Initial and boundary conditions

Initial and boundary conditions for meteorology were obtained from the National Centers for Environmental Prediction Final Analysis (NCEP FNL; National Centers for Environmental Prediction, 2000) and we applied spectral nudging within and above the boundary layer. The boundary layer scheme and land surface model used are the Mellor–Yamada Nakanishi Niino Level 2.5 Scheme (MYNN; Nakanishi and Niino, 2009) and the Noah Land Surface Model (Noah-LSM; Tewari et al., 2004), respectively. These options were selected as they were found to give the best representation of boundary layer dynamics in the Arctic from a number of different WRF dynamics configurations (Marelle et al., 2021). Furthermore, we included an additional sea ice thickness variable from the TOPAZ4b model to better simulate surface temperatures over sea ice (EU Copernicus Marine Service Information, 2022).

Initial and boundary conditions for chemical concentrations were set using data from the global CAM-Chem model (Buchholz et al., 2019; Emmons et al., 2020). We also included an initial and boundary concentration of atmospheric Hg(0), obtained from model output simulated by an ensemble of four chemical transport models (see Section 3.4). More details about the model ensemble and its performance in the Arctic can be found in Dastoor et al. (2022a). Concentrations of RM were initialized as zero and were allowed to reach a natural equilibrium during the model spin-up period.

2.2.3. Interactive halogen emissions and recycling

We considered bromine emissions from snow/ice and aerosols using both surface snow and blowing snow sources of reactive bromine emissions and recycling, as described in Marelle et al. (2021). These are interactive parameterizations within the model that calculate Br_2 emissions online. Specifically, the surface snow mechanism calculates the emission of Br_2 following the deposition of ozone to the snowpack over sea ice (Toyota et al., 2011). This process is accelerated under sunlit conditions compared to dark conditions. The blowing snow mechanism calculates the release of Br_2 and sea salt aerosols from the sublimation of lofted snow under windy conditions (wind speeds >7 m s^{-1}; Yang et al., 2008; Yang et al., 2019). Finally, heterogeneous recycling of bromine on all frozen surfaces is also considered in this work, following Marelle et al. (2021). These interactive bromine emissions were evaluated in Marelle et al. (2021) by comparing with Arctic ozone observations, including in the central Arctic from ice-tethered buoys (O-Buoys; Knepp et al., 2010; Halfacre et al., 2014), showing a good representation of springtime ozone depletion.

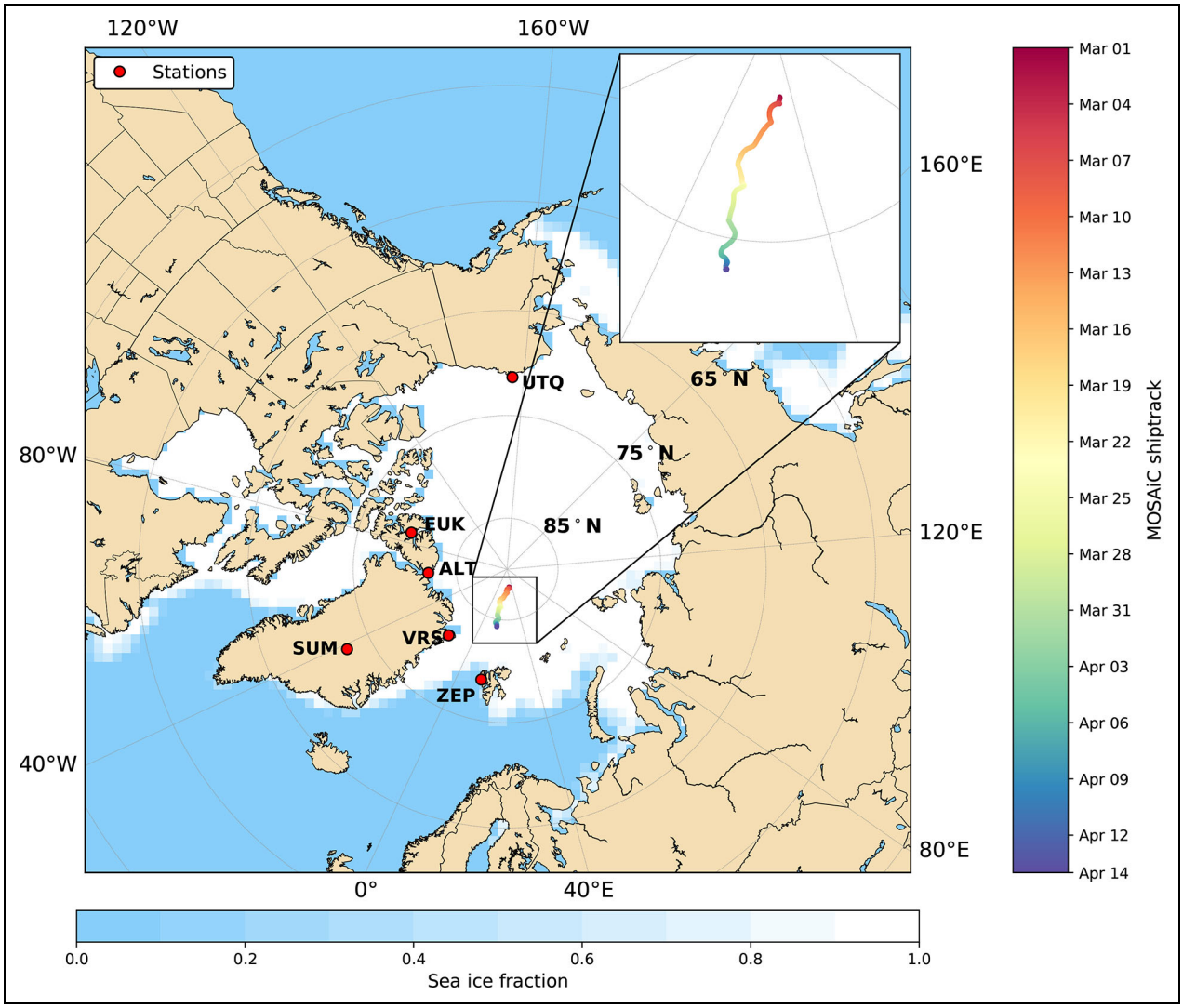

Figure 2. WRF-Chem model domain. The MOSAiC *Polarstern* shiptrack between March 1 and April 14, 2020, is shown together with the sea ice fraction at the beginning of the simulation (March 1, 2020). Stations used for the model comparison are indicated with red markers (UTQ = Utqiaġvik, Alaska; EUK = Eureka, Canada; ALT = Alert, Canada; VRS = Villum Research Station, Station Nord, Greenland; SUM = Summit, Greenland; and ZEP = Zeppelin Observatory, Svalbard).

2.2.4. Emission inventories

Biogenic emissions are calculated online using the Model of Emissions of Gases and Aerosols from Nature (MEGAN; Guenther et al., 2012). Fire emissions were obtained from the Fire INventory from NCAR version 2.5 (FINNv2.5; Wiedinmyer et al., 2011; Wiedinmyer et al., 2023) and anthropogenic emissions are from the global ECLIPSEv6b inventory (Evaluating of the Climate and Air Quality Impacts of Short-Lived Pollutants version 6b; Klimont et al., 2017). ECLIPSEv6b includes revised international shipping emissions compared to previous versions of the inventory, relevant for capturing local Arctic emission sources. We further added anthropogenic emissions of Hg(0), Hg(II), and Hg(p) from the global anthropogenic mercury emissions inventory for 2015 (Steenhuisen and Wilson, 2022). This inventory was prepared as part of the 2018 AMAP/UNEP Global Mercury Assessment (GMA; AMAP/UN Environment, 2019) and groups emissions into four distinct sectors: fuel combustion, industrial sectors, waste from intentional use, and artisanal and small-scale gold mining (Steenhuisen and Wilson, 2019, 2022). To include anthropogenic emissions of gas-phase Hg(II) in the model, we assumed that these emissions are evenly distributed between each gas-phase Hg(II) species in the model.

3. Measurement data

3.1. MOSAiC observations

The MOSAiC expedition took place on board the *Polarstern* icebreaker, between October 2019 and September 2020, and is the largest scientific exploration of the Arctic to date. A comprehensive suite of measurements were made during drift through the Arctic Ocean to better understand the links between the atmosphere, sea ice, and ocean (Nicolaus et al., 2022; Rabe et al., 2022; Shupe et al., 2022). This extensive dataset provides a unique insight into the chemical behaviour of the atmosphere in the central Arctic. More details about the MOSAiC campaign

Table 2. WRF-Chem 4.3.3 model namelist options and inputs

Physics and Meteorology	Model Option
Planetary boundary layer	MYNN 2.5 level TKE scheme (Nakanishi and Niino, 2009)
Surface layer	MYNN (Nakanishi and Niino, 2009)
Land surface	Noah LSM (Tewari et al., 2004)
Microphysics	Morrison (Morrison et al., 2009)
SW radiation	RRTMG (Iacono et al., 2008)
LW radiation	RRTMG (Iacono et al., 2008)
Cumulus parameterization	KF-CuP (Berg et al., 2015)
Meteorology initial and boundary conditions	NCEP FNL (National Centers for Environmental Prediction, 2000)
Chemistry and Aerosol	**Model Option**
Gas-phase chemistry	SAPRC-99 (Carter, 2000; Marelle et al., 2021)
Aerosols	MOSAIC 8 bins (Zaveri et al., 2008)
	With VBS-2 SOA formation and aqueous chemistry
Photolysis	Fast-J (Wild et al., 2000)
Chemical initial and boundary conditions	CAM-Chem (Buchholz et al., 2019; Emmons et al., 2020)
Hg(0) initial and boundary conditions	Global model ensemble
Emissions	**Model Input**
Hg emissions	Global Mercury Assessment 2018
	(Steenhuisen and Wilson, 2019, 2022)
Anthropogenic emissions	ECLIPSEv6b (Klimont et al., 2017)
Fire emissisions	FINNv2.5 (Wiedinmyer et al., 2011; Wiedinmyer et al., 2023)
Biogenic emissions	MEGAN (Guenther et al., 2012)

can be found in Shupe et al. (2022). For the purpose of our modelling study, we used a subset of meteorological and chemical observations made during MOSAiC which are introduced below.

3.1.1. Meteorological observations

Continuous surface meteorological measurements were made onboard the *Polarstern* at various locations and heights. Measurements of air temperature and relative humidity were made at a height of 29 m above sea level using a Vaisala HMP155 probe. Wind speed and wind direction were measured at 39 m above sea level using an ultrasonic anemometer. The meteorological measurement data used here to evaluate the WRF-Chem model are available at Schmithüsen (2021).

Radiosondes (model Vaisala RS41-SGP) measuring temperature, humidity, and winds were routinely launched every 6 hours throughout the whole expedition (Maturilli et al., 2021). During synoptic events of special interest, such as major storms, the launch frequency was enhanced up to three-hourly. The launches were performed from the helicopter deck of the *Polarstern*, approximately 12 m above the sea level, so the data do not capture the lowermost part of the boundary layer. Furthermore, polluted data may exist in the lowermost approximate 100 m, in cases when the sonde flew through the ship's exhaust fan or was otherwise influenced by the ship's presence.

3.1.2. Elemental mercury observations

As described in Angot et al. (2022b), Hg(0) measurements were performed in the University of Colorado sea-container laboratory using a Tekran 2537B analyzer. Only Hg(0) was collected and analyzed (as opposed to total gaseous mercury) as cation-exchange membranes were used to remove potential divalent Hg species. All instruments located within this container were automatically backflushed with zero-air when wind direction was more than ± 130 degrees from the ship bow to prevent any contamination of the sampling line by the ship exhaust. This backflushing explains the presence of gaps in the Hg(0) time series. The Hg(0) dataset can be accessed at Angot et al. (2022a).

3.1.3. Ozone observations

Ozone ambient-air mole fractions were monitored in three different sea-container laboratories using commercial instruments. The three individual ozone time series were cross-evaluated and used to generate the hourly averaged merged dataset used in this study. This merged dataset limits gaps in the ozone time series (as opposed to the Hg(0) time series; see above). More information can be found in Angot et al. (2022b). The O_3 dataset can be accessed at Angot et al. (2022c).

3.1.4. BrO observations

The Multi-Axis Differential Optical Absorption Spectroscopy (MAX-DOAS) technique (Lohberger et al., 2004; Plane and Saiz-Lopez, 2006; Platt and Stutz, 2008) was used to make observations of BrO during the MOSAiC expedition. The instrument (Prados-Roman et al., 2015) has an external telescope used to collect scattered sunlight connected to an indoor spectrometer using an optical fibre. The outdoor unit consisted of a telescopic lens (focal length of 200 mm, diameter 50.8 mm), which focused light onto an optical fibre. The optical fibre was connected to the indoor unit consisting of a spectrometer (Princeton Instruments SP500i) and a Charge-Coupled Device detector (camera CCD Princeton Instruments Pixis 400B). The instrument was placed at a height of 15 m from the sea surface and an inclinometer was used to correct the measured elevation angles using the actual pitch and roll of the instrument during the expedition. The solar spectra were then

analysed using the QDOAS software (Fayt et al., 2011) to retrieve the absorption due to the oxygen dimer (O_4) and BrO at different viewing elevation angles, using the zenith spectra as a reference (see Figure S2). The resulting Differential Slant Column Densities (DSCDs) are the difference of the slant column densities (SCDs) in the viewing direction and the SCD in the zenith direction. The DOAS retrieval settings are given in Table S1, and an example of the DOAS fit can be found in Benavent et al. (2022). The AC-2 radiative transfer model (Benavent, 2020) was then used to derive mixing ratios of BrO by estimating the path length from the O_4 DSCDs. This is a two-step process where the O_4 DSCDs are used to estimate the light path length and subsequently the mixing ratio of BrO is estimated. Considering that in most cases BrO was above the detection limit only at the lowermost angles (<3 degrees), an average mixing ratio across the first kilometer is computed due to lack of information above it. Photographs of sky conditions were used to filter the data for blowing snow and broken cloud cover to avoid multiple scattering effects, which can lead to the incorrect conversion of DSCDs into mixing ratios.

3.2. Arctic stations

3.2.1. Mercury observations

Measurements of total gaseous mercury at Villum Research Station (Station Nord, Greenland), Zeppelin Observatory (Svalbard), and the Dr. Neil Trivett Global Atmosphere Watch Observatory (Alert, Nunavut, Canada) were performed using Tekran 2537 instruments and are part of ongoing long-term monitoring efforts (e.g., MacSween et al., 2022). Teflon inlet filters were used to remove gaseous oxidized mercury during sampling, but it is possible that small amounts of Hg(II) are measured by the analyzers. This contribution is assumed to be small, relative to the overall Hg(0) signal, and therefore these measurements are henceforth referred to as Hg(0). Hg(II) and Hg(p) measurements at Alert were made using a Tekran 1130/1135 speciation unit, sampled at a 2-hour time resolution and reported on a 3-hour time interval (Steffen et al., 2014). More information on the instrumental setup and quality control procedures can be found elsewhere (Berg et al., 2013; Steffen et al., 2014; Angot et al., 2016; Skov et al., 2020).

3.2.2. Ozone observations

Surface ozone data from Villum (Greenland) and Zeppelin (Svalbard) were retrieved from the EBAS database (http://ebas-data.nilu.no/default.aspx). All measurements were performed using commercial UV absorption instruments (detection limit of 1 ppb). Surface ozone data from Utqiaġvik (Alaska), Summit (Greenland), and the Polar Environment Atmospheric Research Laboratory (Eureka, Nunavut, Canada) were provided by the NOAA Global Monitoring Laboratory (https://www.esrl.noaa.gov/gmd/ozwv/surfoz/data.html). These measurements are also performed using a commercial UV absorption instrument. More information can be found in Platt et al. (2022).

3.3. Satellite BrO observations

Satellite BrO data of the high-resolution TROPOspheric Monitoring Instrument (TROPOMI) on the Sentinel-5 Precursor (S5P) satellite were used to retrieve total BrO columns by applying the method from Seo et al. (2019). To obtain the tropospheric BrO Slant Column Density (SCD), the stratospheric part was removed from the total column using the stratospheric correction method described in Theys et al. (2011). It requires stratospheric ozone and NO_2 columns from TROPOMI and the tropopause height, which were taken from the NCEP Reanalysis 1 product (Kalnay et al., 1996). The tropospheric BrO Vertical Column Densities (VCDs) were obtained from the tropospheric SCDs using an air mass factor suitable for a surface BrO layer of 400 m thickness over a bright surface. As a result, boundary layer BrO over dark surfaces such as open oceans may be underestimated.

3.4. Global model ensemble output

Simulations for the MOSAiC year (Oct 2019 to Sept 2020) were performed with the multi-model ensemble (GLEMOS, GEOS-Chem, GEM-MACH-Hg, and DEHM) used for the recent Global Mercury Assessment (Arctic Monitoring and Assessment Programme/UN Environment, 2019) and Arctic Monitoring and Assessment Programme reports (AMAP, 2021). A description of the four models can be found in Dastoor et al. (2022a), along with a full evaluation of their performances in the Arctic. A subset of this simulation (March–April 2020) was used to provide initial boundary conditions of Hg(0) in the model simulation presented here.

4. Model evaluation with MOSAiC observations

We evaluated the hourly model outputs against meteorological and chemical measurements made onboard the *Polarstern* during MOSAiC. We used several metrics to provide a comparison between the model and observations, including the Pearson correlation coefficient (r), root-mean-square error (RMSE), and mean bias error (MBE). Performance metrics between the model and the MOSAiC observations are given in **Table 3**.

4.1. Simulated meteorological conditions during MOSAiC

Polar boundary layer stability is crucial in modulating atmospheric chemical composition near the surface via impacts on vertical mixing, surface emissions, and chemistry. Accurately modelling boundary layer structure is therefore necessary to investigate surface chemistry and air-snow exchange processes. We evaluated the meteorological configuration of the model by comparing the simulated boundary layer meteorology with observations obtained onboard the *Polarstern*. **Figure 3** shows the comparison between the simulated and observed meteorology for several variables including air temperature, relative humidity, wind speed, and wind direction. Simulated variables were extracted at the nearest model grid cell to the location of the ship. Modelled air temperatures are largely in good agreement with the observations ($r = 0.85$; **Figure 3a**), despite a mean positive bias (MBE = 1.95 K)

slightly overestimating both warm and cold periods. The model also shows good performance in simulating surface wind speeds ($r = 0.97$) and wind directions, with the exception of relative humidity ($r = 0.31$), which is biased low (MBE $= -7.69\%$).

Table 3. Goodness-of-fit statistics between model and observations along the MOSAiC shiptrack

Variable	r^a	RMSE[b]	MBE[c]
Surface air temperature	0.85	2.67 K	1.95 K
Vertical air temperature			
05:00	0.97	0.59 K	−0.14 K
11:00	0.94	0.57 K	−0.20 K
17:00	0.94	0.58 K	−0.08 K
23:00	0.96	0.42 K	−0.08 K
Relative humidity	0.31	9.49%	−7.69%
Wind speed	0.97	1.03 m s^{-1}	−0.15 m s^{-1}
Hg(0)	0.81	0.24 ng m^{-3}	−0.09 ng m^{-3}
O_3	0.82	6.53 ppb	0.35 ppb
BrO	0.42	11.85 ppt	9.78 ppt

[a]Correlation coefficient.

[b]Root mean square error.

[c]Mean bias error.

To evaluate the vertical structure of the boundary layer, we compared the average simulated and observed temperature profiles above the *Polarstern* (**Figure 4**). Radiosondes were launched from the ship up to four times a day at regular intervals: 05:00, 11:00, 17:00, and 23:00 UTC (to the nearest hour). In total, 119 radiosondes were launched during the simulated period. **Figure 4** shows the comparison between the mean observed and simulated temperature profiles. For this comparison, we have interpolated the model output to the hour/location of the sonde releases and averaged all profiles available for each daily release time (05:00, 11:00, 18:00, 23:00 UTC); we show the lowest two kilometers of the atmosphere to focus on the near-surface atmosphere representation in the model. The purpose of this comparison is to provide an indication of overall model performance in simulating the vertical structure of the polar boundary layer. At each time interval, the model shows good agreement with the mean observed vertical temperature profiles, within the standard deviation range of the observations. In the lowest 250 m, we find a positive bias of 1–2°C in the model, consistent with the warm bias in **Figure 3a**. This warm bias can be associated with the presence of near-surface temperature inversions, common in the Arctic. The difficulty in capturing these inversions is not unique to our model, and is a challenge facing many models and reanalyses (Graham et al., 2019). Similar comparisons between modelled and observed vertical profiles of winds and relative humidity (Figures S3–S5) also show good model

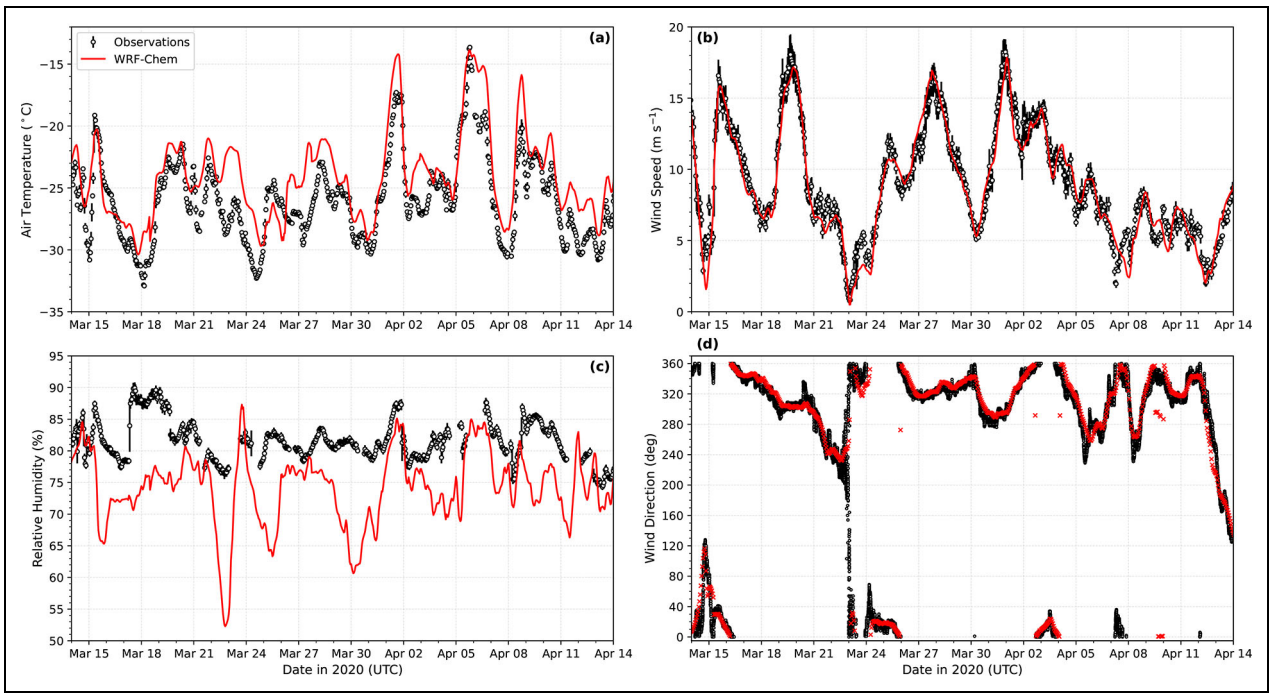

Figure 3. Model comparison of meteorological variables with MOSAiC observations. Hourly averages of observed (black) and simulated (red) boundary layer meteorology of (a) air temperature (29 m above sea level, asl); (b) wind speed (39 m asl); (c) relative humidity (29 m asl); and (d) wind direction (39 m asl, 1-minute measurements plotted) during MOSAiC. Standard deviation of the observations are shown by the black bars. Simulated values are extracted at the closest grid cell to the shiptrack.

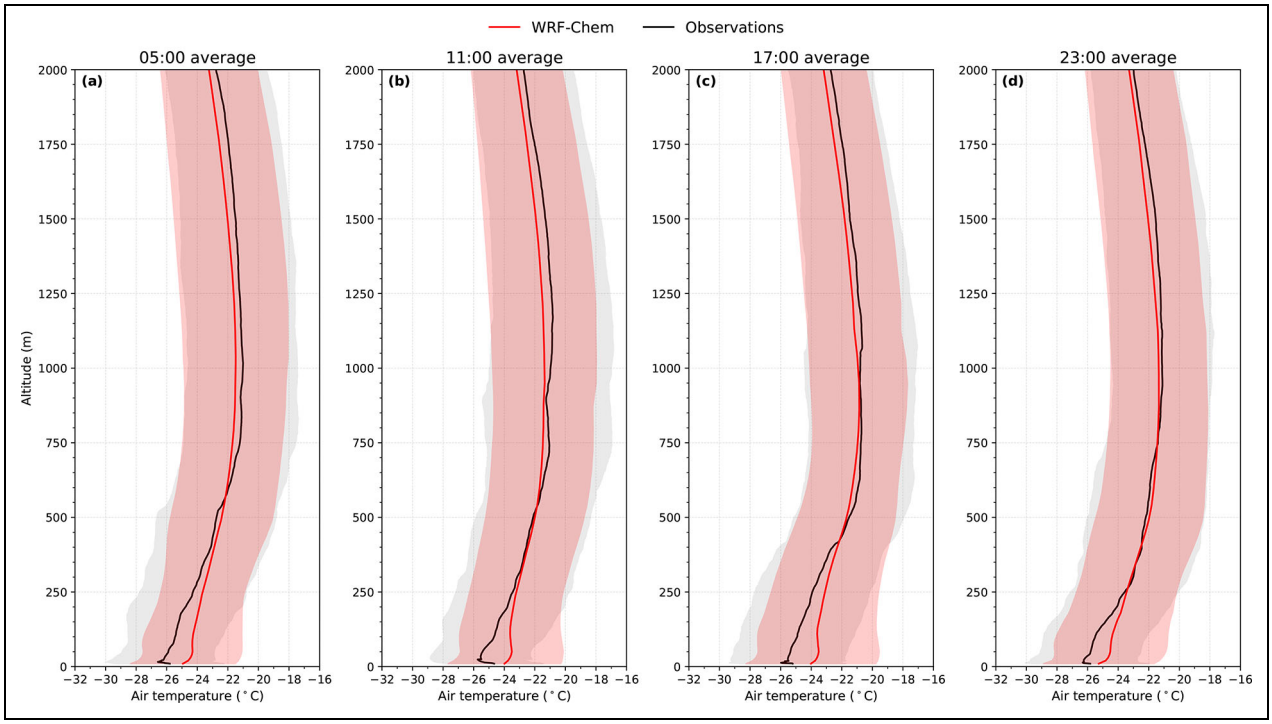

Figure 4. Model comparison of vertical temperature profiles with MOSAiC radiosonde observations. Mean vertical air temperature profile from radiosonde observations (black) released above the MOSAiC shiptrack and simulated by WRF-Chem (red) during the simulation period (March 14 to April 14, 2020). Model values are extracted at the closest grid cell to the location of each radiosonde flight path. Data are averaged by time interval during the simulated period (to the nearest hour) at (a) 05:00 UTC, (b) 11:00 UTC, (c) 17:00 UTC, and (d) 23:00 UTC. Shaded areas represent the standard deviation of the observed and model averages.

performance in simulating the vertical structure of the boundary layer, despite some differences in the lowest 250 m. Overall, we show that the model performs well in simulating the observed springtime meteorology in the central Arctic, necessary for modelling boundary layer chemistry.

4.2. Mercury, ozone, and bromine evaluation with MOSAiC observations

To evaluate the model, we compared modelled surface Hg(0), O_3, and BrO with observations made onboard the *Polarstern* (**Figure 5**). Performance metrics are shown in **Table 3**. We also note here that a 2-week model spin-up time was selected based on the time needed to stabilize the chemical state of Hg(0) and O_3 in the central Arctic (grey shaded area in **Figure 5**). Observations of Hg(0) show extended periods of depletion (**Figure 5a**), defined as Hg(0) < 1 ng m^{-3} (Angot et al., 2016) and concentrations were frequently recorded below 0.5 ng m^{-3}. Similarly, intense depletion of ozone was observed (**Figure 5b**), where O_3 was regularly below 10 ppb and depletion lasted multiple days, particularly in late March/early April. This level of Hg(0) and O_3 depletion is indicative of enhanced surface chemistry and emissions of bromine from sea ice, capable of sustaining the depletion over an extended period of time. There is also a strong correlation between the observations of Hg(0) and O_3 ($r = 0.91$), suggesting depletion of both species is driven by bromine, as reported in a previous Arctic measurement study (Wang et al., 2019). Hg(0) concentrations during periods of missing measurement data (e.g., March 18–23 and March 31 to April 3) are therefore likely to be consistent with O_3 concentrations, which exhibit regular depletion during these periods. Our model predicts substantial depletion of both Hg(0) and O_3, in relatively good agreement with the observations ($r = 0.81$ and $r = 0.82$ for Hg(0) and O_3, respectively). In particular, the model is able to capture the prolonged periods of Hg(0) and O_3 depletion in late March/early April. However, simulated Hg(0) has a small negative bias (MBE $= -0.09$ ng m^{-3}), potentially due to high bromine-initiated oxidation, and the model also underestimates certain periods of ozone recovery (e.g., March 21–23). Comparing the simulated time series of Hg(0) and O_3, we find a very strong correlation ($r = 0.99$), indicating oxidation by Br is the major process in the model.

To further assess the extent of bromine-initiated oxidation of Hg(0) and O_3, we compared the average modelled BrO in the lowest 1 km of the atmosphere to MAX-DOAS observations (**Figure 5c**). The TROPOMI tropospheric column BrO is shown along the MOSAiC ship track as a reference for comparison (right axis in **Figure 5c**). We highlight here that there is some uncertainty in directly comparing the lowest 1 km of model data with the MAX-DOAS measurements; however, this uncertainty is difficult to quantify. Our model predicts high BrO concentrations above the shiptrack of up to 40 ppt. The observed concentrations are up to a factor of 5 times smaller than the

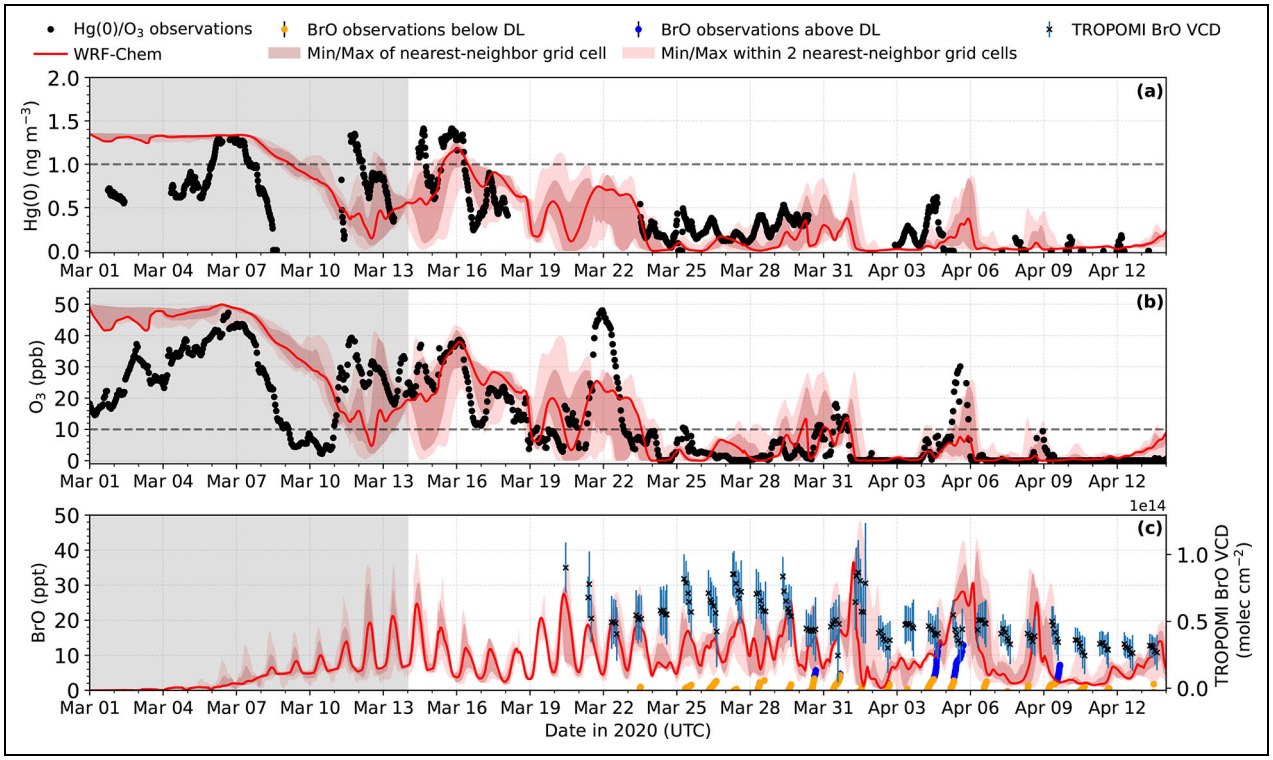

Figure 5. Model comparison of chemical species measured during MOSAiC. Surface measurements during MOSAiC (black) of (a) 30-min averaged Hg(0) concentration and (b) hourly averaged O_3 concentration. Simulated concentrations by WRF-Chem plotted in red. (c) BrO observed by MAX-DOAS (left axis, yellow: below detection limit; and blue: above detection limit) and TROPOMI (right axis) during MOSAiC and simulated by WRF-Chem (0–1 km average). TROPOMI data are the total tropospheric column plotted as the average values recorded within 150 km of the MOSAiC shiptrack with standard deviation shown by the error bars. WRF-Chem simulated values are extracted at the closest grid cell to the shiptrack. Grey dashed lines represent the values of Hg(0) and O_3 depletion events ($<$1.0 ng m^{-3} and $<$10 ppb, respectively). Red-shaded areas represent the minimum and maximum values simulated by WRF-Chem around the shiptrack grid cell in a 3×3 and 5×5 grid. Dark grey-shaded areas represent the model spin-period excluded from the analysis.

model predicted estimates (r = 0.42, MBE = 9.78 ppt), with many periods of BrO below the detection limit and uncertainty typically below 1 pptv. The average concentrations in the lowest 1 km of our WRF-Chem simulation are, however, consistent with timing and relative abundance of BrO from the total tropospheric column retrieved from TROPOMI (**Figure 5c**). Putting these measurement data in the context of previous Arctic BrO observations, they are much lower than peak levels of around 50 pptv recorded from satellite and ground-based observations (Wagner et al., 2001; Hönninger and Platt, 2002; Peterson et al., 2017; Simpson et al., 2017). These observations of BrO during the MOSAiC spring season were made mainly during periods when ozone was near complete depletion. That reactive bromine can be present even when there are low BrO concentrations is well known, due to the fact that BrO formation cannot occur when O_3 is depleted.

There are several possible causes for the difference between modelled and observed BrO. The main loss of BrO is via reaction with hydroperoxyl radicals (HO_2), forming HOBr. Inaccurate HO_2 concentrations from VOC oxidation may result in insufficient HOBr production, which could maintain high concentrations of BrO. In addition, our description of bromine activation assumes an infinite bromide reservoir from snow on both first-year sea ice and multi-year sea ice (Herrmann et al., 2022). This assumption may overestimate bromine activation from multi-year ice regions, where measurements of bromide in snow on Arctic multi-year ice have recorded lower concentrations than on first-year ice (Krnavek et al., 2012; Peterson et al., 2019). Uncertainties related to the BrO retrievals that allow for calculation of the BrO concentrations from the MAX-DOAS observations may also contribute to these differences. Finally, heterogeneous recycling on aerosols may sustain reactive bromine concentrations above the surface, independently of snowpack activation (Peterson et al., 2017). An overestimation in modelled aerosol concentrations, or a high reactive uptake probability of bromine, may therefore contribute to an enhancement of bromine recycling and BrO concentrations at altitudes above the surface.

In summary, the model is able to simulate Hg(0) and O_3 depletion in the central Arctic, in good agreement with the observations. There is strong correlation between the Hg(0) and O_3 time series (observed and modelled), indicating oxidation of both species is driven by bromine. However, modelled BrO quantities are overestimated compared to the observations, which may positively bias

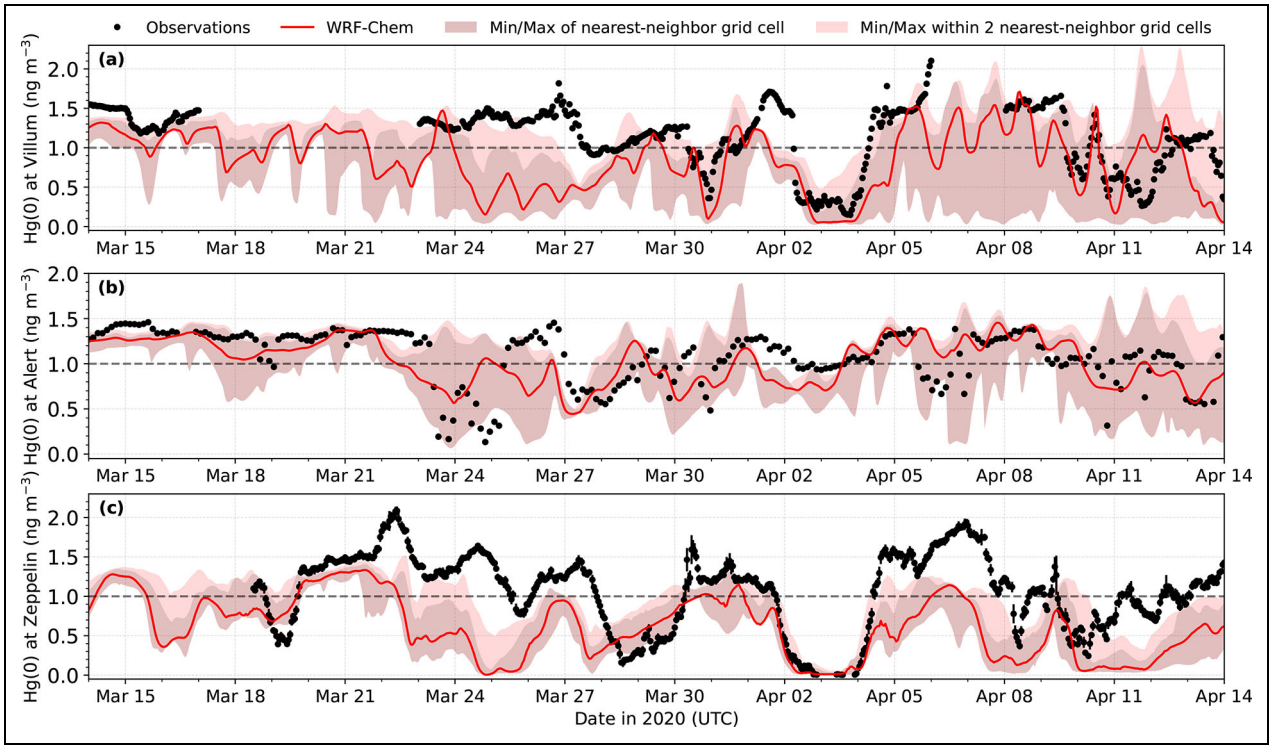

Figure 6. Model comparison of surface concentrations of elemental mercury, Hg(0), with observations from coastal Arctic stations. Surface Hg(0) observed (black) and simulated by WRF-Chem (red) at (a) Villum, Greenland (hourly average); (b) Alert, Canada (2-hour average); and (c) Zeppelin, Svalbard (hourly average). Grey dashed lines represent the value of Hg(0) depletion events ($<$1.0 ng m^{-3}). Red-shaded areas represent the minimum and maximum values simulated by WRF-Chem around the station grid cell in a 3×3 and 5×5 grid.

oxidation of Hg(0) and O_3 by bromine. A recent study, based on reactive bromine and iodine measurements, has attributed a large contribution of ozone destruction to iodine chemistry, on a level comparable with bromine (Benavent et al., 2022). These measurements were made during MOSAiC, at the same time and location modelled in this study, and are the first measurements of iodine monoxide (IO) in the central Arctic. In this work, we did not include iodine chemistry in our model, and our halogen descriptions are limited to bromine and chlorine cycling. Future investigations could aim to extend our model chemical mechanism to include descriptions of this chemistry and to explore its impact on ozone depletion. For this work focused on the mercury cycle, the impact of iodine chemistry is expected to be minimal on mercury oxidation and deposition.

5. Model evaluation of regional Arctic mercury, ozone, and bromine chemistry

5.1. Model evaluation at Arctic stations and with satellite retrievals

In addition to the model comparison with MOSAiC observations, we further evaluated the model with measurement data from other Arctic locations. Here, we compare the simulated surface Hg and O_3 concentrations to observations at Arctic stations, as well as modelled tropospheric BrO vertical column density with satellite-derived measurements. An additional comparison of meteorology at 3 Arctic stations is also provided in Figures S6–S8.

5.1.1. Hg(0) at Arctic stations

Figure 6 compares modelled surface Hg(0) to hourly averaged observations at Villum (Greenland) and Zeppelin (Svalbard), and 3-hour averaged observations at Alert (Canada). Overall, we find relatively good agreement between the model and observations in capturing the timing of AMDEs at each measurement site. There is a general negative bias in the simulated Hg(0) time series compared to the observations (**Table 4**), suggesting either too much net Hg(0) oxidation (via high bromine concentrations) or low/missing sources (including re-emission from snow, open ocean sources, and transport from mid-latitudes).

At Villum (**Figure 6a**), the model is able to simulate key features of the observed Hg(0) time series ($r = 0.50$), with some discrepancies discussed below. During the simulated period, six AMDEs were observed (March 27, March 30–31, April 2–4, April 9–10, April 10–13, and April 14). The model is able to simulate most features (timing and intensity) of five of the six events. On April 2, a depletion event lasting approximately 2 days was observed, where Hg(0) concentrations fell below 0.5 ng m^{-3}. The intensity and duration of this event is captured by the model, although recovery to background levels in the model lags by approximately 1 day, possibly suggesting low re-emission from snow in the model. The model incorrectly predicts a depletion event between March 24 and March 29 which was not observed. These differences can partly be explained by the coarse horizontal resolution of the

Table 4. Goodness-of-fit statistics between model and observations for Hg and O_3 at Arctic sites

Station	Variable	r^a	RMSE[b]	MBE[c]
Villum	Hg(0)	0.50	0.53 ng m^{-3}	−0.35 ng m^{-3}
	O_3	0.54	19.1 ppb	−15.1 ppb
Alert	Hg(0)	0.54	0.27 ng m^{-3}	−0.05 ng m^{-3}
	Hg(II)	−0.08	59.0 pg m^{-3}	43.2 pg m^{-3}
	Hg(p)	0.26	150 pg m^{-3}	53.9 pg m^{-3}
	O_3	0.64	8.15 ppb	−2.49 ppb
Zeppelin	Hg(0)	0.53	0.64 ng m^{-3}	−0.49 ng m^{-3}
	O_3	0.56	14.4 ppb	−7.61 ppb
Utqiaġvik	O_3	0.52	16.6 ppb	−11.3 ppb
Summit	O_3	0.64	9.01 ppb	6.67 ppb
Eureka	O_3	0.52	11.9 ppb	−0.10 ppb

[a]Correlation coefficient.

[b]Root mean square error.

[c]Mean bias error.

model (100 km). Due to the proximity of Villum to sea ice, this grid cell may partly factor in emissions of bromine from sea ice. We therefore also show in **Figure 6** the minimum and maximum Hg(0) values within the two nearest neighbour grid cells (shaded regions). The large variability of Hg(0) concentration within neighbouring grid cells highlights the marked differences in emissions and chemistry of Hg(0) over land-based snow and sea ice.

At Alert (**Figure 6b**), Hg(0) is regularly close to background levels (approximately 1.4 ng m^{-3}), with some intermittent periods of Hg(0) depletion. Simulated Hg(0) shows reasonable agreement with the observations (r = 0.54) with a small negative bias (MBE = −0.05 ng m^{-3}). Speciated Hg measurements at Alert were also available during this period and are evaluated in more detail in Section 5.2. Observations at Zeppelin (**Figure 6c**) recorded several depletion events lasting 1–3 days. There is a broad underestimation of modelled Hg(0) compared to the observations (r = 0.53), which could be explained in part by low/missing land-based sources (including re-emission from snow). Limitations in model resolution may also contribute to this negative bias by poorly representing the local mountain meteorology at Zeppelin. Chemistry, emissions, and transport at this site can all be impacted as a consequence. Despite the mean negative bias (MBE = −0.49 ng m^{-3}), the timing of depletion and replenishment of Hg(0) are often captured by the model at Zeppelin.

Overall, the model is generally able to reproduce the behaviour of Hg(0) at these sites, with the timing of depletion events often simulated correctly by the model, but underestimating Hg(0) concentrations. The negative bias in modelled Hg(0) concentration is likely a factor of the coarse horizontal resolution of the model, resulting in high bromine oxidation and low Hg(0) re-emission at these sites. Higher resolution model runs are therefore desirable to discern the contributions of bromine oxidation and Hg(0) re-emission from land-based snow and from sea ice at coastal Arctic stations.

5.1.2. Ozone at Arctic stations

Figure 7 compares modelled and hourly averaged observations of surface O_3 at six Arctic stations: Villum (Greenland), Alert (Canada), Zeppelin (Svalbard), Utqiaġvik (Alaska), Summit (Greenland), and Eureka (Canada). Model performance metrics are listed in **Table 4**. At Villum (**Figure 7a**), observations of O_3 are correlated with the Hg(0) time series (r = 0.93) shown in **Figure 6a**. Modelled O_3 is in reasonable agreement with the observations (r = 0.54), with similar features and discrepancies as previously shown in the modelled Hg(0) time series. In particular, an ODE during April 2–4 was observed coinciding with depletion of Hg(0), which is reproduced by the model. However, the model also incorrectly predicts depletion of O_3 between March 23 and March 31, indicating an overestimation of bromine. Modelled O_3 at Alert (**Figure 7b**) is relatively well captured by the model (r = 0.64). The observed time series of O_3 and Hg(0) also show very similar features, with a depletion event recorded for both species during March 23–25. At Zeppelin (**Figure 7c**), multiple ODEs were observed and O_3 concentrations correlate strongly with the Hg(0) measurements (r = 0.88). The timing and intensity of these ODEs are mostly captured by the model (r = 0.56). However, there is an overall mean negative bias in the model (MBE = −7.61 ppb), with a marked underestimation between March 23 and March 26 (as in the Hg(0) comparison). This bias is again suggestive of an overestimation in bromine activation during this period. Comparing the modelled O_3 and Hg(0) time series at these three stations, we find a very strong correlation at

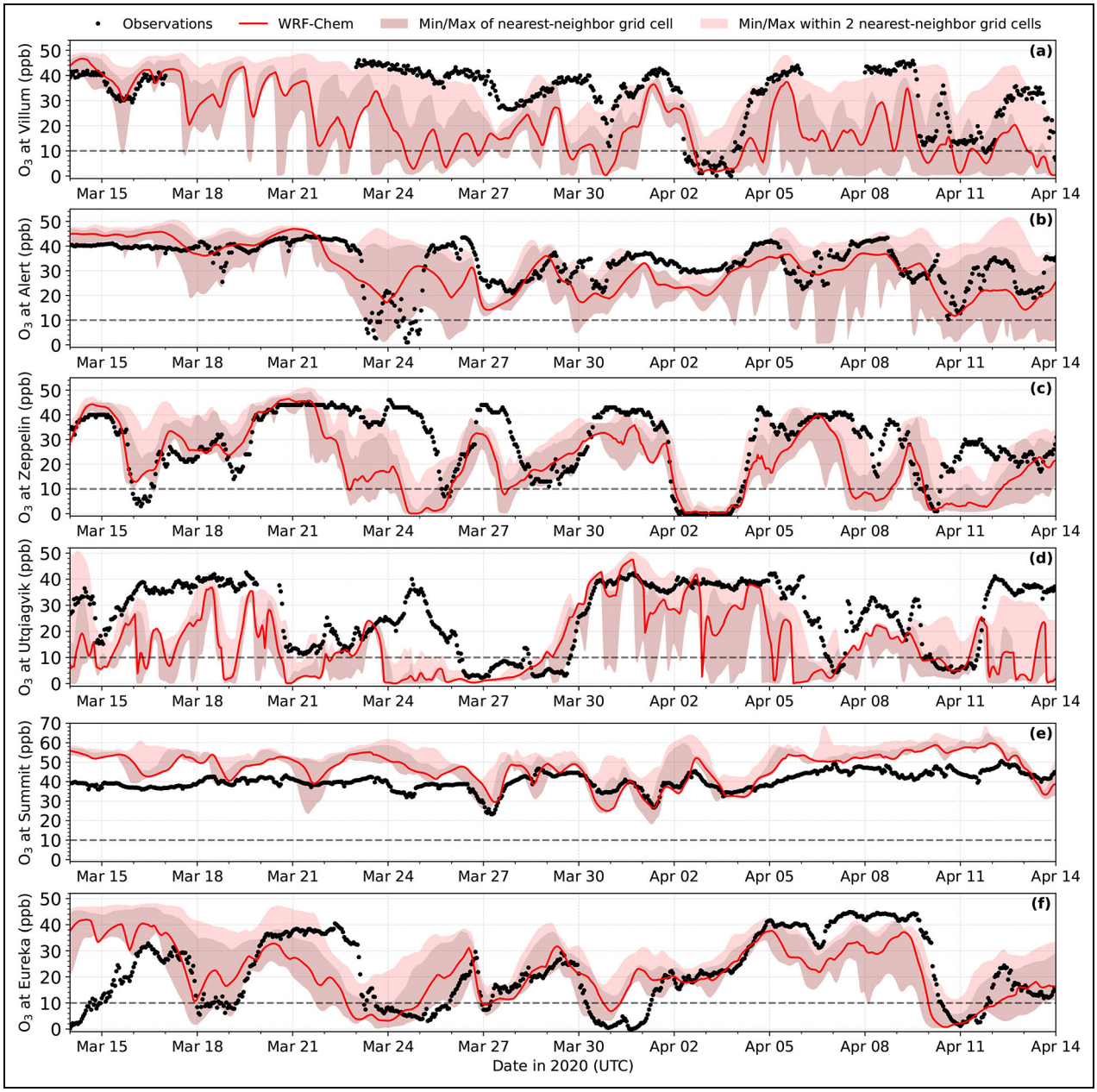

Figure 7. Model comparison of surface ozone concentrations with observations from Arctic stations. Hourly average of surface O_3 observations (black) and simulated O_3 by WRF-Chem (red) at (a) Villum, Greenland; (b) Alert, Canada; (c) Zeppelin, Svalbard; (d) Utqiaġvik, Alaska; (e) Summit, Greenland; and (f) Eureka, Canada. Grey dashed lines represent the value of O_3 depletion events (<10 ppb). Red-shaded areas represent the minimum and maximum values simulated by WRF-Chem around the station grid cell in a 3×3 and 5×5 grid.

each site (Villum $r = 0.73$, Alert $r = 0.88$, and Zeppelin $r = 0.99$), indicating that bromine is also the major Hg(0) oxidant in the coastal Arctic.

Ozone measurements at Utqiaġvik show several ODEs which the model is only partially able to capture (**Figure 7d**). In general, the model overpredicts ozone depletion indicating highly active bromine chemistry ($r = 0.52$, MBE = −11.3 ppb). At Summit (**Figure 7e**), no depletion events were observed or simulated by the model due to the location of the station ($r = 0.64$). Summit is situated at a high altitude (3216 m above sea level) in central Greenland and is therefore largely unaffected by air masses originating over sea ice. There is an overall positive bias in modelled O_3 concentrations (MBE = 6.67 ppb), indicating that the difference may be due to local meteorology (e.g., boundary layer stability) rather than differences in chemistry. At Eureka station (**Figure 7f**), multiple ODEs were observed typically lasting 1–2 days. For most of the simulated period (March 18–April 14), the model performs very well to capture the timing and intensity of ODEs observed at this site ($r = 0.52$). However, ozone concentrations in the first week of the simulation are overpredicted and the depletion is completely missed by the model.

Figure 8 shows the average surface O_3 concentration during the simulation period. On the whole, we find good

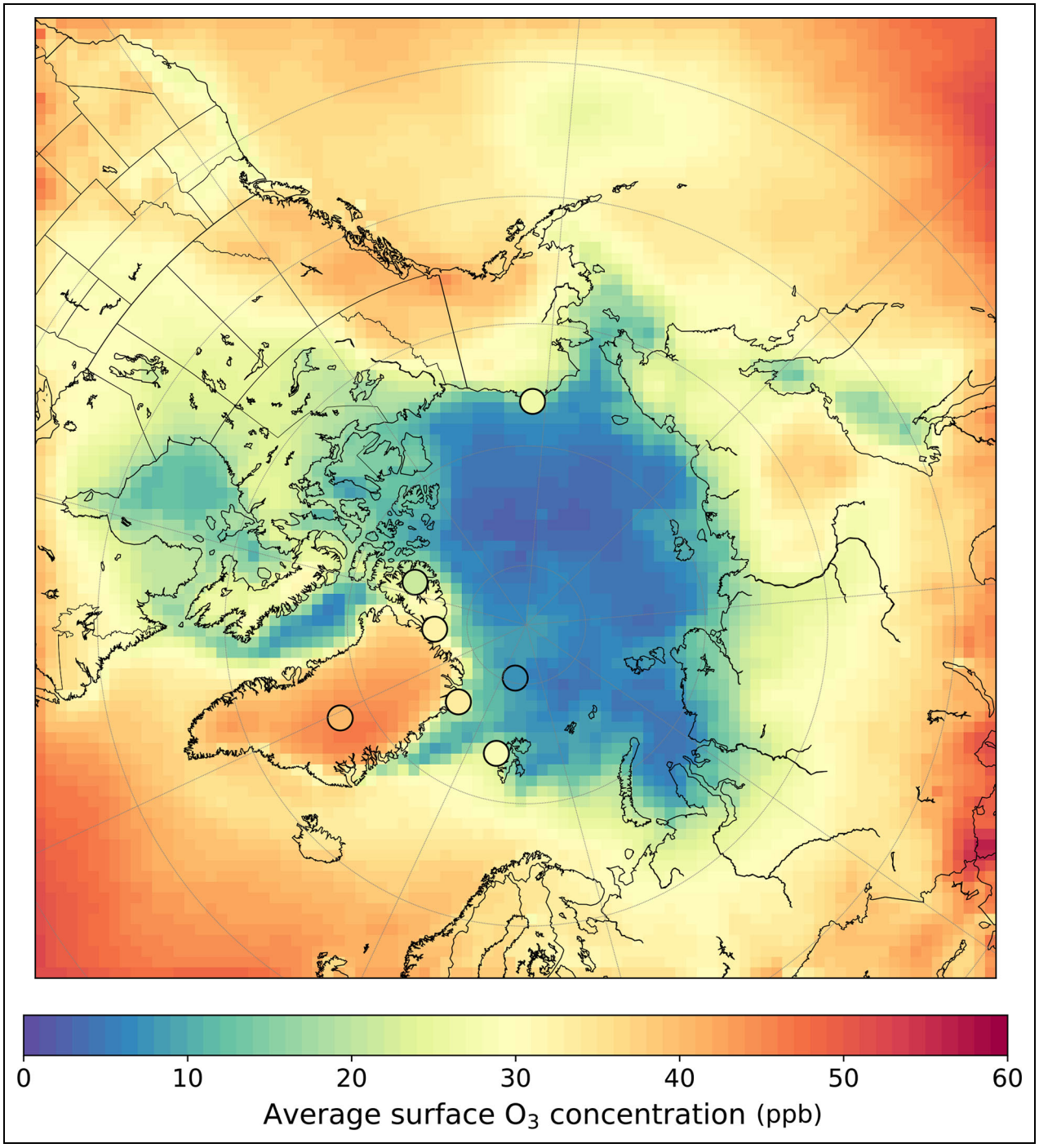

Figure 8. Simulated mean surface ozone concentration. Surface ozone concentration is averaged for the full simulation period (March 14 to April 14, 2020). Observational averages for the same period are shown by markers with the same colour scale.

representation of ozone in the model at several coastal and non-coastal Arctic stations. Most ODEs (including the timing, intensity, and duration) are captured by the model, with the exception of some events which are missed (e.g., at Eureka) or overpredicted by the model (e.g., at Villum). For coastal sites, there is a general negative bias in O_3 suggesting an overestimation in bromine-initiated oxidation. Increased horizontal resolution could again potentially address some of the disparities between model and observations at all sites.

5.1.3. BrO compared to TROPOMI satellite retrieval

We compare in **Figure 9** the modelled and observed mean tropospheric BrO vertical column densities for the simulation period. Satellite observations from TROPOMI on Sentinel-5p are corrected to exclude the stratospheric contribution (see Section 3.3). The first striking difference between TROPOMI (**Figure 9a**) and the modelled BrO (**Figure 9b**) is the different total columns outside the central Arctic over primarily open ocean regions (southeast of Greenland and between Alaska and Russia). This

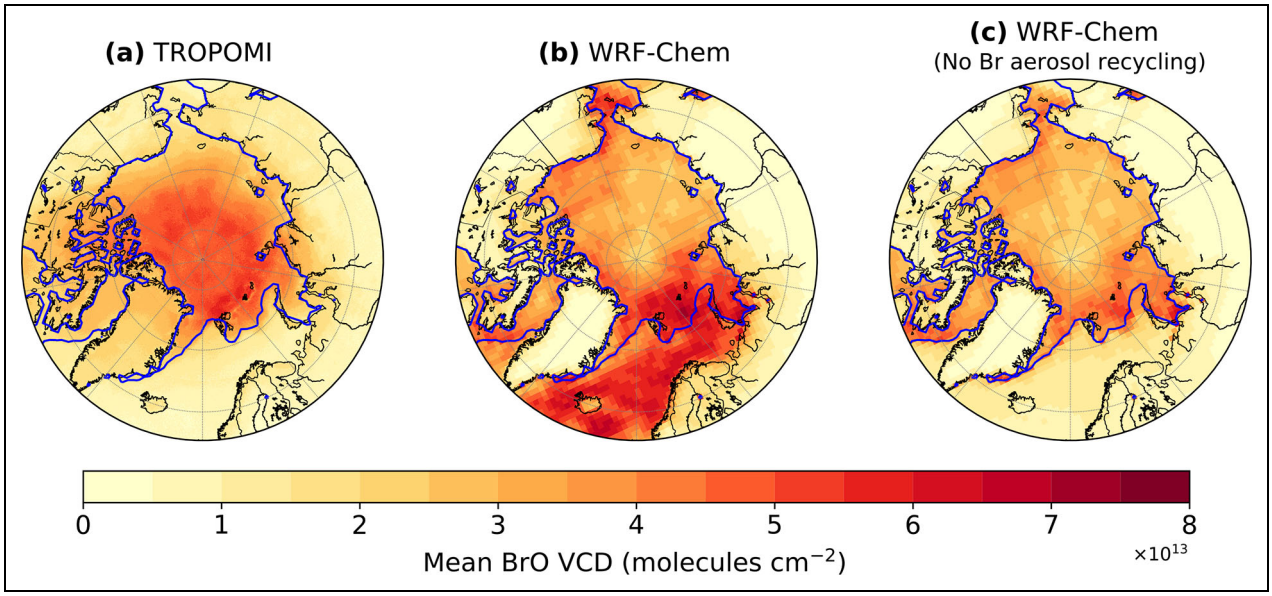

Figure 9. Observed and simulated mean BrO vertical column density (VCD). Mean BrO VCDs are averaged for the full the simulation period (March 14 to April 14, 2020) from (a) TROPOMI on Sentinel-5p and (b) WRF-Chem. (c) WRF-Chem BrO VCD with no heterogeneous recycling of reactive bromine on aerosols. Blue contour lines represent the sea ice fraction above 75% coverage at the beginning of the simulation.

finding can be partly explained by the fact that over open oceans, the sensitivity of satellite observations to boundary layer BrO is largely reduced due to low albedo and cloud effects (Seo et al., 2019), and therefore satellite columns may be too low. The difference also points to the fact that the BrO lifetime in our model may be too long and allows for transport outside the sea ice-covered source region for initial bromine activation or the fact that we have too much bromine recycling on surfaces outside sea ice-covered regions. Peterson et al. (2017) reported observations of BrO in the Arctic boundary layer sustained by heterogeneous recycling on aerosols, which is one way that reactive bromine can be sustained in air away from the surface. Reactive bromine concentrations are sustained on aerosols and transported to higher altitudes in the free troposphere where they can be transported longer distances away from the original emissions sources over sea ice-covered regions. However, the rate of recycling and re-emissions on aerosols remains uncertain. To explore the effect of recycling on aerosols away from the surface and its impact on sustaining BrO activation away from sea ice, we completed a sensitivity run with aerosol bromine recycling turned off. The result of this run (**Figure 9c**) is in better agreement with BrO VCD observed, with an underestimation in BrO abundances. This result is clearly not a realistic representation of bromine aerosol chemistry, but provides valuable information regarding the role of bromine activation and transport via recycling aerosols in the Arctic. It shows the need for future work on both evaluating modelled aerosol concentrations and/or inaccuracies in the treatment of heterogeneous bromine chemistry.

There are also differences in the central Arctic between TROPOMI (**Figure 9a**) and the modelled BrO (**Figure 9b**) VCDs, over the sea ice-covered regions, for example at the North Pole (90°N). Here and over other sea ice-covered regions the model underpredicts the total BrO column compared to the satellite VCD. There are several possible reasons for underprediction, including the fact that the model underpredicts total BrO due to uncertainties in emissions, vertical transport, and recycling on aerosols (discussed in the previous paragraph). A key issue that may control BrO abundance near the surface in the model is the ability to replenish ozone-rich air from above the surface down to the key bromine emission sources near the surface, which are snow on sea ice and sea salt aerosols. When ozone is depleted, BrO cannot form even if activated bromine radicals are present. The underprediction of central Arctic BrO VCDs by the model can also be due to the inaccurate representation of vertical transport of activated bromine away from the surface into the free troposphere, where large quantities of ozone are available for reaction to form BrO. The simulated boundary layer (Figure S9) was often below 700 m, which indicates the volume in which emitted bromine is in direct contact with the surface and can be recycled on surface snow and aerosols. BrO formed near the surface was found to be mixed above the boundary layer height (Figure S10), with ozone depletion extending up to 2 km above the surface (Figure S11). While aloft, recycling of bromine is limited to aerosol surfaces as shown in Peterson et al. (2017), resulting in less frequent events of elevated BrO aloft above the boundary layer height.

5.2. Mercury speciation in the Arctic

In **Figure 10**, we have plotted the modelled chemical speciation of surface Hg(0), Hg(II), and Hg(p) averaged over the simulation period. Observational averages from Arctic stations (where possible) and the MOSAiC shiptrack are also plotted for the same period. Modelled Hg(0)

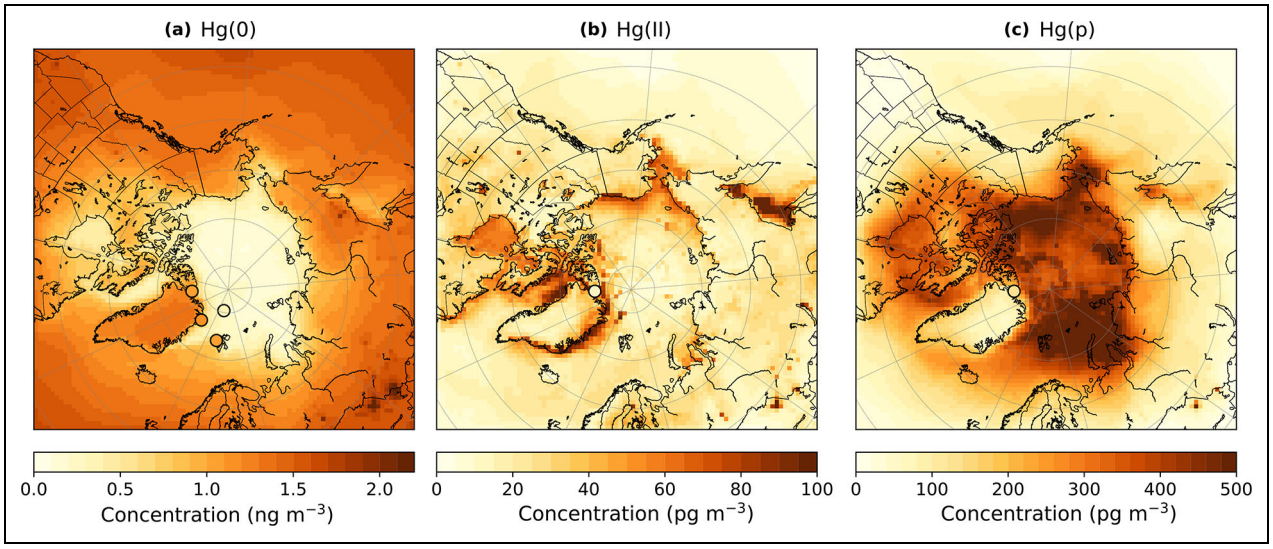

Figure 10. Simulated mean surface mercury speciation. Mercury concentrations are averaged for the full simulation period (March 14 to April 14, 2020) for surface concentrations of (a) elemental mercury, Hg(0), (b) gaseous oxidized mercury, Hg(II), and (c) particulate mercury, Hg(p). Observational averages for the same period are shown by markers with the same colour scale.

shows depletion in the central Arctic, due to bromine emissions from sea ice, with higher Hg(0) concentrations over land (**Figure 10a**). The simulated surface average is in good agreement with the available observations and predicts a latitudinal gradient with increasing Hg(0) concentrations at lower latitudes. Simulated surface gaseous Hg(II) concentrations are in the range of 0–100 pg m^{-3}, with the highest concentrations around the coasts and minima over the central Arctic (**Figure 10b**). The five major contributing species in the model are HgX (gaseous Hg(II) volatilized from aerosols), HgOHOH, HgBrOH, HgBrBrO, and $HgBr_2$, indicating high bromine oxidation (**Table 1**). Measurements at Alert report an average Hg(II) concentration of approximately 10 pg m^{-3} during this period, lower than the model average of 48 pg m^{-3}. Modelled Hg(p) concentrations (**Figure 10c**) are close to an order of magnitude greater than Hg(II). During the simulated period, the mean Hg(p) concentration observed at Alert was 125 pg m^{-3}, with the model average in close agreement (158 pg m^{-3}). The tropospheric budget of Hg (**Table 1**) shows that approximately 63% of all oxidized mercury in the model is present as Hg(p), indicating high aerosol processing. We note here that we do not include the photoreduction of Hg(p) on organic aerosols to Hg(0), as in previous Hg modelling studies (e.g., Shah et al., 2021; Zhang and Zhang, 2022), as this photolysis rate is still poorly constrained. By including this process we could expect to see a decrease in the modelled average Hg(p) concentration, and an increase in mean surface Hg(0) concentrations. Overall, the mean modelled Hg(0), Hg(II), and Hg(p) concentrations show reasonable agreement with Arctic observations, within the measurement uncertainty.

We next consider these results in the context of previous Hg speciation measurements in the Arctic during spring. Observations have consistently shown greater Hg(p) concentrations than gaseous Hg(II) in early spring, over both tundra and sea ice (Cobbett et al., 2007; Manca et al., 2013; Steffen et al., 2013; Steffen et al., 2014; MacSween et al., 2022). Long-term observations of Hg at Alert (2002–2011) reported average Hg(II) concentrations of 11 pg m^{-3} and 34 pg m^{-3} and Hg(p) concentrations of 137 pg m^{-3} and 150 pg m^{-3} during March and April, respectively (Steffen et al., 2014). These amounts are within the range of our model results, demonstrating a higher fraction of modelled Hg(p) during early spring. From the same long-term dataset, Hg(p) concentrations reached an annual maximum in April, while Hg(II) concentrations peaked during May. The reason for the springtime peak in Hg(p) has been investigated and associated with several variables. Low temperatures have been shown to increase the transition of gaseous Hg(II) to Hg(p), as well as a high fraction of organic and chloride containing aerosols (Amos et al., 2012; Steffen et al., 2014; Xu et al., 2020). In addition, the transport of air pollution from mid-latitudes to the Arctic during winter and spring (known as Arctic haze) brings high aerosol concentrations, contributing to the predominance of Hg(p) in spring. Our results are in agreement with these findings, with maximum Hg(p) simulated in the central Arctic, indicating the influence of high aerosol concentrations and low temperatures on Hg(II)/Hg(p) partitioning. Furthermore, Steffen et al. (2013) reported mean concentrations of 30 pg m^{-3} and 393 pg m^{-3} for Hg(II) and Hg(p), respectively, over Arctic sea ice in spring 2009. Observations of Hg(0) made concurrently over both snow-covered tundra and sea ice showed that Hg(0) was often significantly higher over tundra than over sea ice, indicating higher re-emission (Steffen et al., 2013). This finding is consistent with the observations in 2020 (**Figure 10a**) as well as the model prediction, where Hg(0) concentrations over continental snow are higher than over sea ice. Hg(0) re-emission over land-based snow and sea ice is discussed further in Section 5.4.

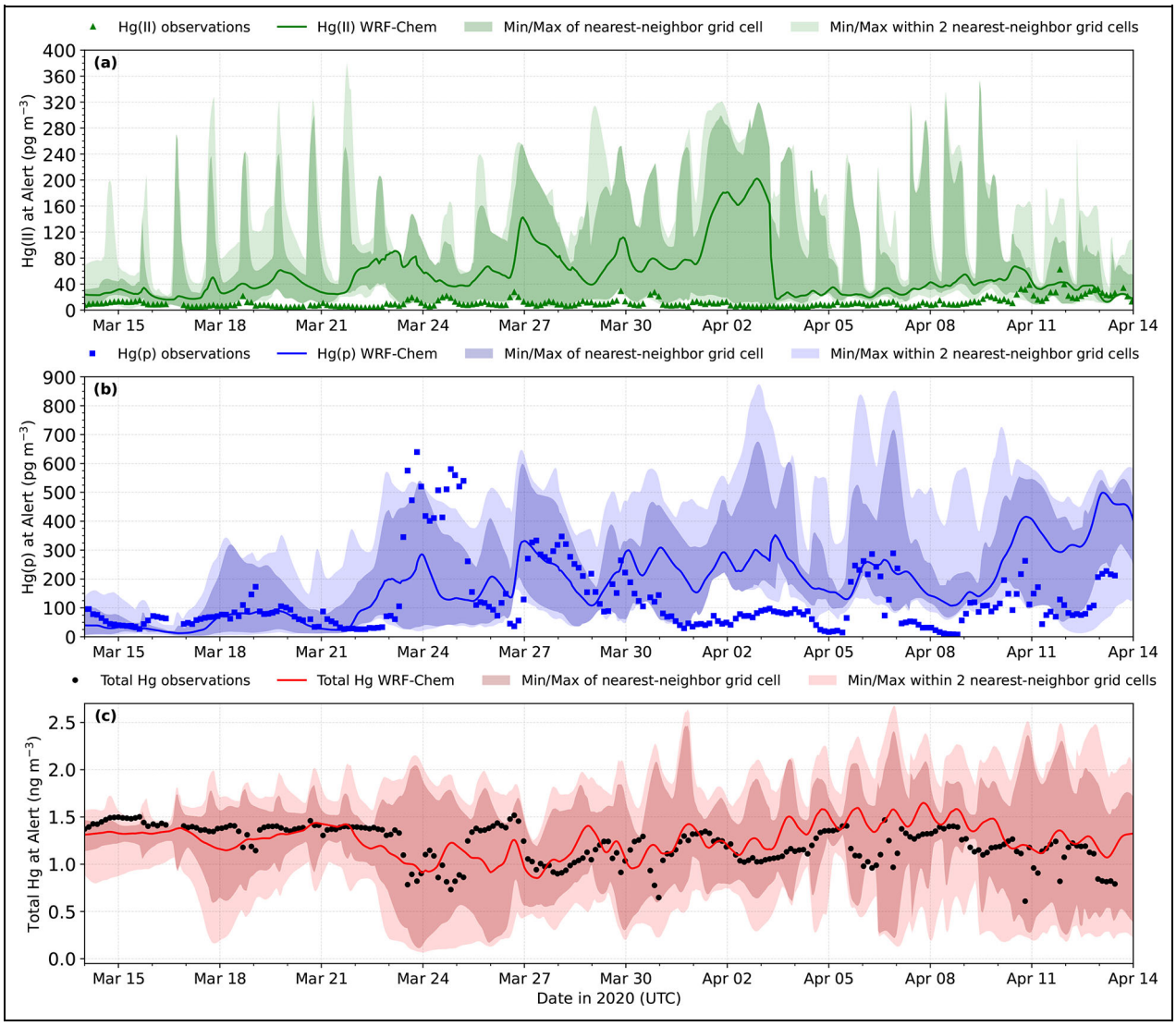

Figure 11. Model comparison of surface speciated mercury with observations from Alert, Canada. (a) Gaseous oxidized mercury, Hg(II), (b) particulate mercury, Hg(p), and (c) total atmospheric Hg, Hg(0)+Hg(II)+Hg(p) at Alert, Canada.

Figure 11 shows the time series of simulated and 3-hour averaged observations of gaseous Hg(II), Hg(p), and total Hg at Alert (Canada). The model overestimates Hg(II) at this site (**Figure 11a**), and for Hg(p), we find relatively good agreement with the observations during March, but overestimated Hg(p) concentrations in April (**Figure 11b**). Several factors may contribute to this overestimation. Firstly, uncertainties in the measurements may partially explain some of this difference (Gustin et al., 2015). There is growing evidence that Hg speciation measurements may be biased low by a factor of 1.5–12 (e.g., Gustin et al., 2013; Huang et al., 2013; Gustin et al., 2015; Osterwalder et al., 2021) due to analytical challenges. Whether measurements in high latitudes are biased low or not is, however, still a matter of discussion as relative humidity and ozone levels (both shown to influence the collection efficiency of the denuders) are typically low. Model inaccuracies in Hg gas-particle partitioning and other relevant processes are also likely to contribute. As shown in **Figure 6b**, modelled Hg(0) concentrations at Alert are in good agreement with the observations. Additionally, the total Hg concentration is well reproduced by the model (**Figure 11c**), suggesting that high Hg(II) and Hg(p) concentrations are unlikely to be caused solely by an overestimation in Hg(0) oxidation or re-emissions. Consequently, the overestimation of Hg(II) and Hg(p) indicates a potential underestimation in the loss of Hg(II) and Hg(p) via deposition. The relative amounts of atmospheric Hg(II) and Hg(p) have been shown to directly impact snow Hg concentrations in the Arctic (Steffen et al., 2014). Mercury deposition to snow and sea ice is discussed further in Section 5.3. Finally, we once again note the potential role of coarse model resolution on differences between the model and observations, with large variation shown for Hg(II) and Hg(p) in neighbouring grid cells (shaded regions in **Figure 6**).

Overall, the model is capable of simulating the average springtime speciation of Hg(0), Hg(II), and Hg(p) over snow and sea ice compared to observations. Hg(II)/Hg(p) partitioning at Alert was not fully captured by the model

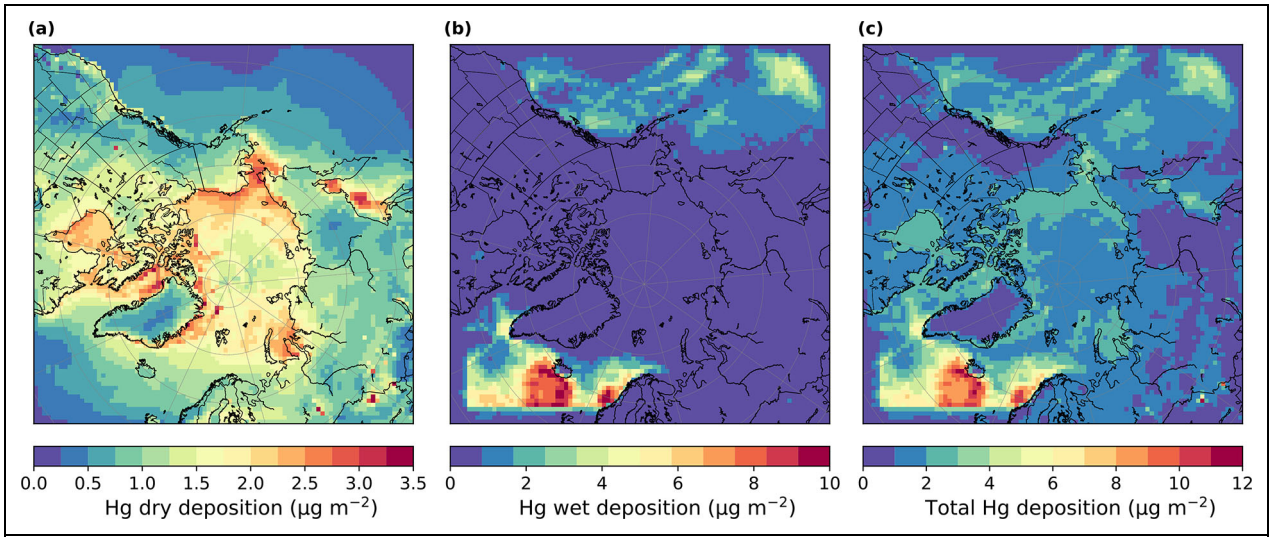

Figure 12. Accumulated model mercury deposition during the simulation period. (a) Hg dry deposition, (b) Hg wet deposition, and (c) total Hg deposition between March 14 and April 14, 2020.

and more work is needed to refine/test the relevant processes including Hg(II) and Hg(p) deposition, sensitivity of Hg(II) uptake to aerosols, photoreduction of Hg(p), and uncertainties in the gas-particle partitioning equilibrium. Recent analysis of trends in Arctic Hg speciation over the past 20 years suggests that the composition and timing of AMDEs are changing (MacSween et al., 2022). Therefore, more observations of speciated Hg at high latitudes are also necessary to better evaluate models and to monitor shifts in springtime Hg chemistry.

5.3. Mercury deposition in the Arctic

Modelled Hg deposition fluxes (dry and wet) are presented in **Figure 12**. We find that dry deposition (**Figure 12a**) is the main Hg deposition process over land and sea ice. The majority of dry-deposited Hg in the model is from Hg(II) and Hg(p), accounting for 88% of total Hg dry deposition, with only 12% from Hg(0). Over sea ice, the model predicts an even greater fraction of dry deposition from RM (approximately 98%). The percentage contribution of RM to dry deposition is consistent with the higher fraction of RM during spring, compared with other seasons. For wet removal (**Figure 12b**), the model predicts maximum wet deposition over the open ocean, consistent with previous Hg modelling studies (Holmes et al., 2010; Horowitz et al., 2017; Travnikov et al., 2017; Shah et al., 2021; Zhang and Zhang, 2022). We also find minimal wet deposition of Hg in the central Arctic and over land. This finding is unsurprising as the Arctic typically exhibits low precipitation rates (snow and rain) during spring, and consequently low wet deposition. To contextualize these results, we next compare our modelled deposition fluxes with previous observational and modelling results in the Arctic.

Annually averaged observations of Hg wet-deposition fluxes in the Arctic and sub-Arctic have been reported in the range of 0–5 g m^{-2} yr^{-1} (Sanei et al., 2010; Sprovieri et al., 2017; Pearson et al., 2019). In Alaska, mean annual Hg wet-deposition fluxes of 2–5 g m^{-2} yr^{-1} were recorded at 5 different locations, over several years (2008–2015; Pearson et al., 2019). Sprovieri et al. (2017) also reported multi-year (2012–2015) mean fluxes of Hg wet deposition of 0.8–1.7 g m^{-2} yr^{-1} at Ny-Ålesund, Svalbard. Furthermore, measurements from two Canadian sub-Arctic sites have shown wet deposition fluxes of 0.5–2.0 g m^{-2} yr^{-1} (Sanei et al., 2010). Direct comparison between the model and observations is not entirely feasible, as the simulation is not temporally consistent with the observations, thus ignoring seasonal variation in precipitation rates, chemistry, and deposition. Measurement challenges also introduce some uncertainty in these values as the collection efficiency of samplers can be affected by the type of precipitation (rain vs. snow; Prestbo and Gay, 2009; Rasmussen et al., 2012). However, these observations can still serve as a good indicator of general model performance.

Compared to the reported measurements above, the model underestimates Hg wet deposition over all these locations, predicting a negligible amount of Hg wet deposition. One explanation is the seasonal differences in precipitation rates, with trends showing an annual peak in the Arctic during summer, likely contributing to greater Hg wet deposition. During the simulated period, our model predicts low precipitation above 60°N, with a cumulative average of 78 mm. Cumulative snowfall measurements from MOSAiC reported estimates of 72–107 mm, between October 31, 2019, and April 26, 2020, giving evidence to the low precipitation rates in the central Arctic (Wagner et al., 2022). Another possibility is the model implementation of Hg(II) wet deposition, which is currently treated by considering the solubility of Hg(II) equal to that of HNO_3. However, this assumption is a broad simplification and should be addressed in future model developments. The model-predicted average of total Hg deposition in the Arctic (>60°N) is 1.65 g m^{-2} (**Figure 12c**). This value is on the lower range of the recent model-ensemble predictions (10.5 ± 5.0 g m^{-2} yr^{-1}, between March and May) of Dastoor et al. (2022a). However, our modelled deposition rates are not truly representative of the entire spring season, as we would expect

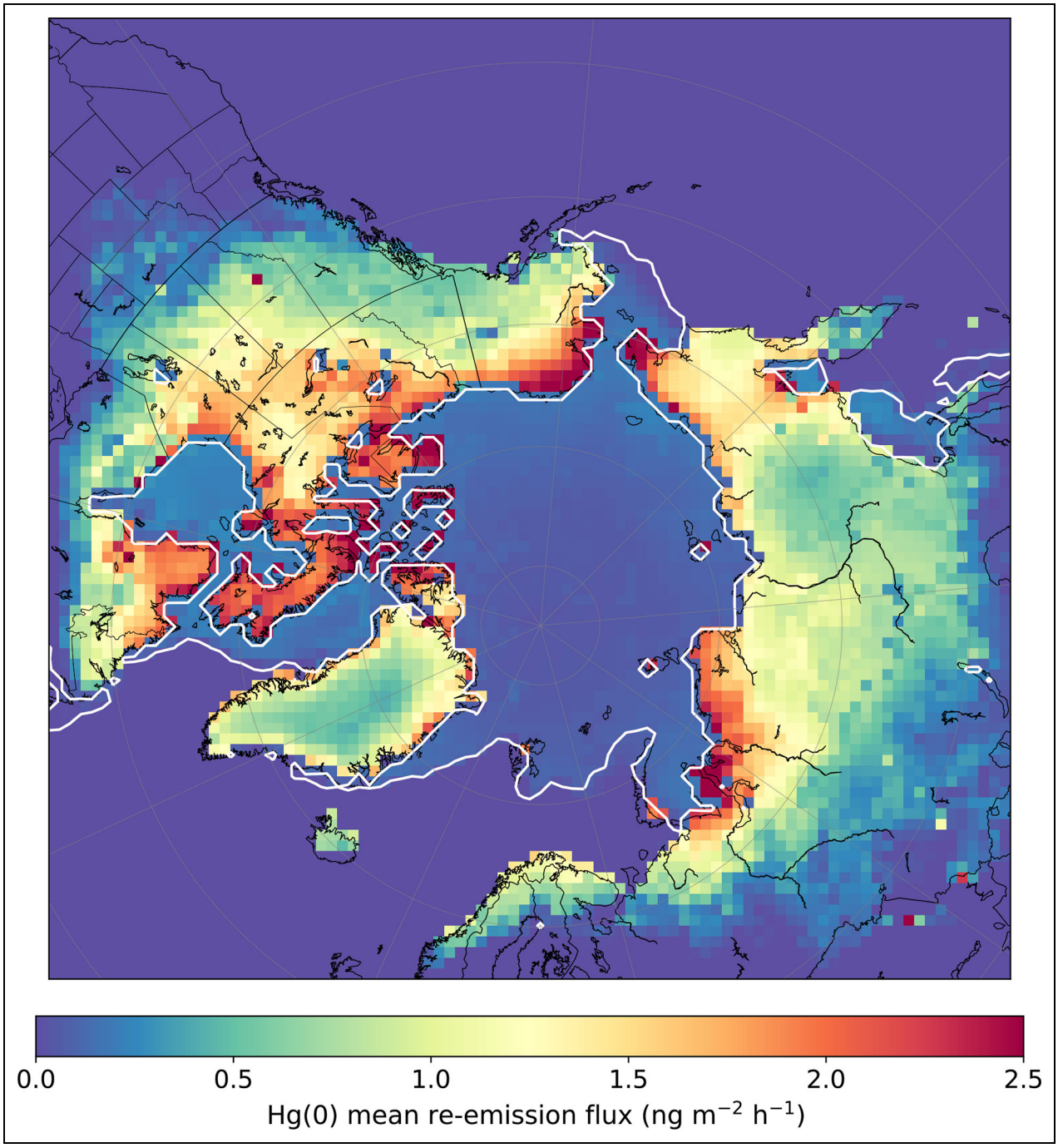

Figure 13. Simulated average re-emission flux of elemental mercury, Hg(0), from snow and sea ice. Simulated mercury re-emission flux is averaged for the full simulation period (March 14 to April 14, 2020). White contour line represents the sea ice fraction above 75% coverage at the beginning of the simulation.

higher deposition rates in late spring as a result of the transition from high Hg(p) to high Hg(II) in the Arctic (Steffen et al., 2014). There is also a large variability in simulated springtime deposition fluxes between models (e.g., Angot et al., 2016; Dastoor et al., 2022a) due to differences in model performance of simulating AMDEs. Further evaluation of modelled Hg deposition fluxes with springtime measurements are needed, particularly at Arctic sites where observations are limited. Alternatively, a year-long model simulation could provide a better comparison with observations; however, additional model developments would be required (e.g., improved description of Hg(II) and Hg(p) wet deposition) before this simulation can be performed.

5.4. Hg(0) re-emission from snow and sea ice

Figure 13 shows the simulated mean Hg(0) re-emission flux, based on deposited RM to snow and sea ice. Mean Hg(0) re-emission fluxes up to 2.5 ng m^{-2} h^{-1} are predicted over coastal snow-covered regions, whereas re-emission from sea ice is considerably lower (approximately 0.1 ng m^{-2} h^{-1}). In the context of Arctic

observations, Hg(0) re-emission fluxes from snow have been reported with large variability, ranging from mean net negative fluxes (e.g., Brooks et al., 2006; Cobbett et al., 2007; Steen et al., 2009; Manca et al., 2013) to mean positive fluxes up to 534 ng m^{-2} h^{-1} during spring (Schroeder et al., 2003; Ferrari et al., 2005; Sommar et al., 2007; Ferrari et al., 2008; Steen et al., 2009; Mann et al., 2015b; Kamp et al., 2018). Direct comparison between reported values and the modelled fluxes is difficult due to differences in measurement techniques, sampling locations, AMDE frequency, and time of year, resulting in different atmospheric conditions and snowpack properties. As a broad assessment, however, the simulated re-emission fluxes here (0–2.5 ng m^{-2} h^{-1}) are within the ranges reported by many Arctic and sub-Arctic measurement studies (Dommergue et al., 2003; Schroeder et al., 2003; Ferrari et al., 2005; Sommar et al., 2007; Ferrari et al., 2008; Mann et al., 2015b). Caution should also be taken when evaluating mean fluxes as studies have shown large re-emission fluxes immediately following AMDEs, often several times greater than the average springtime re-emission flux (e.g., Ferrari et al., 2008; Manca et al., 2013; Kamp et al., 2018). A subsequent investigation of Hg(0) re-emission following AMDEs in the model would therefore be useful to assess re-emission flux variability during the spring season, and, potentially complement location-based measurement studies. Measurement data of Hg(0) re-emission from sea ice are even more scarce, making it difficult to assess the model values against observations. Additional measurements of snowpack Hg(0) re-emission fluxes over sea ice are particularly desirable to better evaluate and refine the current Hg(0) re-emission parameterization in the central Arctic.

To understand the transfer of Hg between air and snow in the model, we calculated the fraction of deposited Hg re-emitted from snow and sea ice for the entire simulation period. Above 60°N, approximately 40% of deposited Hg is re-emitted back to the atmosphere, with 60% remaining within the snowpack. Over land-based snow, 74% of deposited Hg is re-emitted, whereas only 4% of deposited Hg over sea ice is released back into the atmosphere. We applied a smaller photoreduction rate (k_{red}) of RM on sea ice than for land-based snow (see Section 2.1.4), based on the hypothesis that Hg(0) re-emission is comparatively smaller over Arctic sea ice than the continental snowpack (Steffen et al., 2013). Hg(0) observations over Arctic tundra have shown large peaks following depletion which were not observed with the same intensity over sea ice, suggesting lower re-emission rates (Steffen et al., 2013). The presence of chloride in snow has also been hypothesized to increase Hg retention via stabilisation of Hg(II) and a suppression of photoreduction (Poulain et al., 2004; Hintelmann et al., 2007; Lehnherr and St Louis, 2009). Recent experimental evidence has supported this hypothesis, showing a negative relationship between chloride concentrations and the amount of photoreduced Hg in snow (Mann et al., 2018). In the context of the Arctic, snow on sea ice is overall more likely to retain mercury than land-based snow as sea ice regions are typically more enriched with chloride (Krnavek et al., 2012; Peterson et al., 2019). The exact mechanism of Hg stabilization by chloride in snow remains unclear, with theories proposing the formation of photostable chlorocomplexes, or by considering increased Hg(p) concentration in snow to be more stable against photoreduction (Brooks et al., 2006; Hintelmann et al., 2007; Poulain et al., 2007). For this study, we assumed deposited Hg(p) to be equally photoreducible as Hg(II); however, this assumption may need to be revisited as future work refines our knowledge of the fate of Hg in snow.

We also assessed the sensitivity of our assumption that 60% of deposited RM to snow and sea ice is available for re-emission by performing a simulation where 100% of deposited RM is assumed to be photoreducible (**Figure 14**). Results from this sensitivity test show minimal change to the re-emission fluxes from land-based snow, but re-emissions over sea ice increase by approximately 60–70%. The uncertainty associated with the rate and magnitude of RM photoreduction in snow remains large, motivating more observational and modelling studies to improve our understanding of these processes. Future model development could also aim to refine these parameterizations by testing for different seasons, particularly during summer when Hg(0) re-emissions are known reach their annual maximum (Araujo et al., 2022).

6. Summary and future perspectives

This study presents a comprehensive development of the WRF-Chem model, including Hg gas-phase and aerosol chemistry, deposition, and re-emission processes in the Arctic. The recently improved mercury chemical mechanism of Shah et al. (2021) was added to a version of WRF-Chem that includes polar bromine emissions from surface snow and blowing snow together (Marelle et al., 2021), and tested in a dedicated regional Arctic modelling study for the first time. This new model development allowed us to simulate springtime Arctic ozone and mercury depletion on an hourly timescale, with modelled oxidant concentrations calculated online. Model results were then evaluated with simultaneous measurements of Hg(0), O_3, and BrO from the central Arctic during MOSAiC and from Arctic stations. The main results of this study can be summarized as follows:

- Model predictions of Hg(0) and O_3 show extended periods of depletion in the central Arctic during spring, in agreement with observations from MOSAiC. Our model results also indicate that bromine is the major Hg(0) oxidant in the Arctic, driving springtime Hg(0) depletion.
- Oxidized mercury (Hg(II) and Hg(p)) in the model, evaluated to understand the speciation and spatial distribution of Hg, indicated high aerosol processing of Hg during spring, with Hg(p) accounting for approximately 63% of all Hg(II) species. Measurements of speciated Hg remain sparse and uncertain. A focus on reduced uncertainty in Hg(II) and Hg(p) observations, additional measurement campaigns, and long-term observations are needed to better evaluate the model.

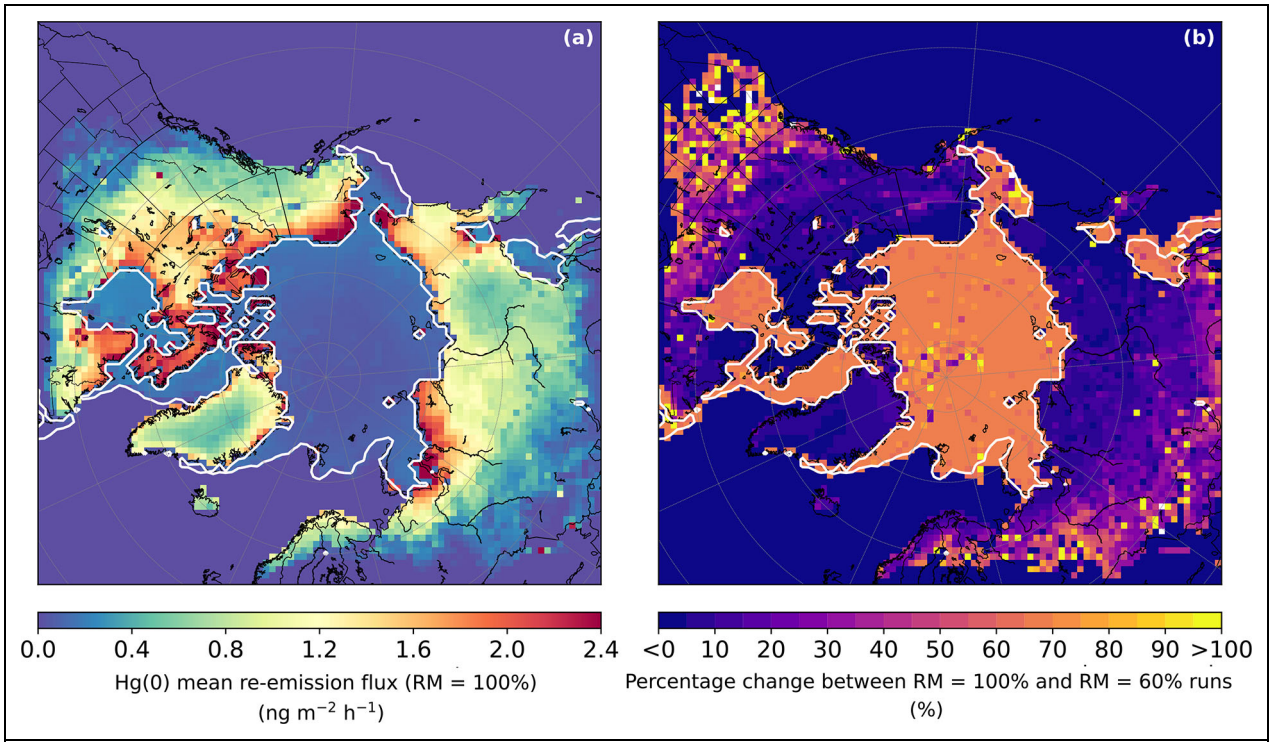

Figure 14. Simulated average re-emission flux of elemental mercury, Hg(0), in the re-emission sensitivity run. (a) Simulation average (March 14 to April 14, 2020) of Hg(0) re-emission flux from snow and sea ice of the sensitivity run, with 100% of deposited reactive mercury (RM) assumed to be photoreducible. (b) Percentage change of Hg(0) re-emission between the sensitivity run assuming 100% and run assuming 60% (**Figure 13**) of RM available for re-emission. White contour lines represent the sea ice fraction above 75% coverage at the beginning of the simulation.

- Both deposition fluxes of oxidized mercury and re-emission fluxes of Hg(0) from snow/ice remain uncertain. Despite this uncertainty, the balance of oxidation, deposition, and re-emission predicted here provides reasonable modelled quantities of gas-phase Hg(0) compared to measurements. Based on experimental evidence, we can expect an average systematic uncertainty of approximately 10%, and in extreme cases up to 20%, for Hg(0) measurements (Slemr et al., 2015).
- For our modelled period, only 4% of deposited Hg(II) and Hg(p) over the Arctic Ocean is re-emitted compared to 96% that remains trapped in snow/ice. Over snow-covered land, the percentage of re-emitted Hg(0) is higher (74% re-emitted vs. 26% retained in the snowpack). The implications of these findings for Arctic Hg(0) summertime re-emission (Araujo et al., 2022), and under long-term environmental changes (e.g., sea ice loss), are important to consider in future work.

This work serves as a basis for future studies to explore some key questions regarding Arctic Hg chemistry. For example, the contribution of the Arctic Ocean to summertime Hg(0) re-emission is an outstanding research question which could be tested using this model. Additionally, the broader impacts of future climate scenarios on Hg chemistry, emissions, and deposition in the Arctic may also be assessed. Overall, this work could enable better predictions of the long-term implications of climate change on Hg contamination of Arctic ecosystems. Finally, we note below the key processes for mercury included in the model that remain uncertain:

- **Chemical kinetics**—Identification of Hg(II) species is a top priority to improve our understanding of mercury redox chemistry. This goal requires additional theoretical, experimental, and modelling studies to reduce uncertainties in the reaction rates of mercury. In particular, photoreduction of Hg(II) and Hg(p) should be investigated further to better constrain the contribution of reduction kinetics to atmospheric Hg chemistry.
- **Dry and wet deposition**—Model descriptions of Hg dry and wet deposition should be revised in future work to more accurately determine the transfer of Hg to snow and ice surfaces.
- **Gas-particle partitioning**—Better understanding of the main model parameters (e.g., heterogeneous uptake rate, partitioning coefficient) that control Hg gas-particle partitioning is needed. An evaluation of modelled aerosol concentrations using observations is needed to refine bromine and mercury heterogeneous recycling on aerosols.
- **Re-emission fluxes from snow and snow on sea ice**—Hg(0) emissions from snow and ice remain difficult to constrain in models due to the complexity of processes that contribute to them and the

difficulty of measuring fluxes. Model assumptions (e.g., 60% reducible Hg in snow, photoreduction rate constants from snow and snow on sea ice) need additional testing. A more accurate representation of factors which influence Hg(0) re-emission (e.g., snowpack chloride concentration) will also likely be needed in future work.

Data accessibility statement

The updated WRF-Chem model code used in this study is available on Zenodo at Ahmed et al. (2022), https://doi.org/10.5281/zenodo.7137482. The surface meteorology measurements made onboard the *Polarstern* can be accessed at Schmithüsen (2021). The MOSAiC radiosonde data are available at Maturilli et al. (2021). The elemental mercury dataset from MOSAiC is available at Angot et al. (2022a). The merged ozone dataset from MOSAiC is available at Angot et al. (2022a). BrO MAX-DOAS measurement data are available at Mahajan (2022). Surface elemental mercury and ozone data at Villum (Greenland) and Zeppelin (Svalbard) are available at the EBAS website https://ebas.nilu.no/. The surface total gaseous mercury measurement dataset at Alert (Canada) is available at https://data-donnees.ec.gc.ca/data/air/monitor/monitoring-of-atmospheric-gases/total-gaseous-mercury-tgm/. The speciated mercury data at Alert (Canada) are available at https://data-donnees.ec.gc.ca/data/air/monitor/monitoring-of-combined-atmospheric-gases-and-particles/speciated-mercury. Surface ozone measurements from Alert (Canada) are provided from the Canadian Air and Precipitation Monitoring Network (CAPMoN) and are available at https://data-donnees.ec.gc.ca/data/air/monitor/monitoring-of-atmospheric-gases/ground-level-ozone/. Surface ozone data at Utqiaġvik (Alaska), Summit (Greenland), and Eureka (Canada) were provided by the NOAA Global Monitoring Laboratory (https://www.esrl.noaa.gov/gmd/ozwv/surfoz/data.html). Satellite BrO VCD data from TROPOMI are available on Zenodo at Zilker and Richter (2023), https://doi.org/10.5281/zenodo.7711532.

Supplemental files

The supplemental files for this article can be found as follows:

Figure S1–S11. Table S1. Available as a merged PDF.

Acknowledgments

We would like to thank the following individuals for their contributions during MOSAiC: Jacques Hueber, Matthew D. Shupe, Marion Maturilli, and Holger Schmithüsen. We also thank all those who contributed to MOSAiC and made this endeavour possible (Nixdorf et al., 2021). We thank all those involved in the operation and maintenance of the *Polarstern* research vessel (Knust, 2017). Computer analyses benefited from access to IDRIS HPC resources (GENCI allocation A011017141) and the IPSL mesoscale computing center. Some observations used here were provided by the Atmospheric Radiation Measurement (ARM) Climate Research Facility, a US Department of Energy (DOE) Office of Science User Facility sponsored by the Office of Biological and Environmental Research. We thank the many ARM operators who supported the field observations. We also thank the Dr. Neil Trivett Global Atmosphere Watch Observatory at Alert for technical support.

Funding

This work was supported by the Ecole Doctorale Sciences de la Terre, de l'Environnement et des Planètes (ED105) of Université Grenoble Alpes. JLT is funded by the European Union's Horizon 2020 research and innovation programme under grant agreement No. 101003826 via project CRiceS (Climate Relevant interactions and feedbacks: the key role of sea ice and Snow in the polar and global climate system). JLT and SA also acknowledge support by the CNRS INSU LEFE-CHAT program under the grant BROM-ARC. Some of the observational data reported in this manuscript were produced as part of the Multidisciplinary drifting Observatory for the Study of Arctic Climate (MOSAiC) expedition with the tag MOSAiC20192020, with activities supported by Polarstern expedition AWI_PS122_00. Data acquisition during the MOSAiC expedition was funded by the US National Science Foundation (NSF) (award OPP 1914781 and award OPP 1807163), the Swiss National Science Foundation (grant 200021_188478), the Swiss Polar Institute, the DOE Atmospheric System Research Program (DE-SC0019251), and the US National Oceanic and Atmospheric Administration (NOAA) Physical Sciences Laboratory. Part of this project was also funded by the European Research Council (ERC), H2020 European Research Council (GASPARCON; grant No. 714621), and the Academy of Finland Flagship funding (grant No. 337552). JS holds the Ingvar Kamprad chair for extreme environments research, sponsored by Ferring Pharmaceuticals. The measurements at Villum Research Station was financially supported by the Danish Environmental Protection Agency with Funds for Environmental Support to the Arctic Region (Project No. J.nr. 2021 – 60333). Measurements in Alert are supported by the Northern Contaminants Program (Crown-Indigenous Relations and Northern Affairs Canada). Satellite BrO data analysis was supported by the Deutsche Forschungsgemeinschaft (project no. 268020496 – TRR 172) within the Transregional Collaborative Research Center "ArctiC Amplification: Climate Relevant Atmospheric and SurfaCe Processes, and Feedback Mechanisms (AC)3" in subproject C03. AR at AWI was partly supported by the European Union's Horizon 2020 research and innovation framework programme under Grant agreement no. 101003590 (PolarRES).

Competing interests

Detlev Helmig (Editor-in-Chief), Hélène Angot (Associate Editor), and Byron Blomquist (Associate Editor) are part of the Editorial board of *Elementa: Science of the Anthropocene*. They were not involved at any step in the review process of this manuscript.

Author contributions

Conceptualization, design, and initial draft of the manuscript: SA, JLT, ADo, HA, RL, JSt.

Model developments: SA, JLT, LM.

Model simulations: SA.

Data acquisition: HA, SDA, A-MB, BB, IB, LB, MB, NB, JHC, ADa, SD, DHo, DHe, H-WJ, TJ, TL, ASM, KP, KAP, LLJQ, ARin, ARy, ARic, AS, AS-L, GS, HS, JSc, OT, BZ.

Editing and revision of the manuscript: All authors.

Approval of the final submitted manuscript for publication: All authors.

References

Abbatt, JPD, **Thomas, JL**, **Abrahamsson, K**, **Boxe, C**, **Granfors, A**, **Jones, AE**, **King, MD**, **Saiz-Lopez, A**, **Shepson, PB**, **Sodeau, J**, **Toohey, DW**, **Toubin, C**, **von Glasow, R**, **Wren, SN**, **Yang, X.** 2012. Halogen activation via interactions with environmental ice and snow in the polar lower troposphere and other regions. *Atmospheric Chemistry and Physics* **12**(14): 6237–6271. DOI: http://dx.doi.org/10.5194/acp-12-6237-2012.

Ahmed, S, **Thomas, JL**, **Marelle, L.** 2022 Regional-Modeling-LATMOS-IGE/WRF-Chem-Polar: WRF-Chem 4. 3.3 including mercury chemistry. Zenodo. DOI: http://dx.doi.org/10.5281/zenodo.7137482.

Amos, HM, **Jacob, DJ**, **Holmes, CD**, **Fisher, JA**, **Wang, Q**, **Yantosca, RM**, **Corbitt, ES**, **Galarneau, E**, **Rutter, AP**, **Gustin, MS**, **Steffen, A**, **Schauer, JJ**, **Graydon, JA**, **Louis, VLS**, **Talbot, RW**, **Edgerton, ES**, **Zhang, Y**, **Sunderland, EM.** 2012. Gas-particle partitioning of atmospheric Hg(II) and its effect on global mercury deposition. *Atmospheric Chemistry and Physics* **12**(1): 591–603. DOI: http://dx.doi.org/10.5194/acp-12-591-2012.

Angot, H, **Archer, S**, **Bariteau, L**, **Blomquist, B**, **Helmig, D**, **Howard, D**, **Hueber, J**, **Jacobi, HW**, **Posman, K.** 2022a. Gaseous elemental mercury concentrations measured in the University of Colorado container during the 2019-2020 MOSAiC (Multidisciplinary drifting Observatory for the Study of Arctic Climate) expedition. Arctic Data Center. DOI: http://dx.doi.org/10.18739/A2C824G3G.

Angot, H, **Blomquist, B**, **Howard, D**, **Archer, S**, **Bariteau, L**, **Beck, I**, **Boyer, M**, **Crotwell, M**, **Helmig, D**, **Hueber, J**, **Jacobi, HW**, **Jokinen, T**, **Kulmala, M**, **Lan, X**, **Laurila, T**, **Madronich, M**, **Neff, D**, **Petäjä, T**, **Posman, K**, **Quéléver, L**, **Shupe, MD**, **Vimont, I**, **Schmale, J.** 2022b. Year-round trace gas measurements in the central Arctic during the MOSAiC expedition. *Scientific Data* **9**(1): 723. DOI: http://dx.doi.org/10.1038/s41597-022-01769-6.

Angot, H, **Blomquist, B**, **Howard, D**, **Archer, S**, **Bariteau, L**, **Beck, I**, **Boyer, M**, **Helmig, D**, **Hueber, J**, **Jacobi, HW**, **Jokinen, T**, **Laurila, T**, **Posman, K**, **Quéléver, L**, **Shupe, MD**, **Schmale, J.** 2022c. Ozone dry air mole fractions measured during MOSAiC 2019/2020 (merged dataset). Pangaea. DOI: http://dx.doi.org/10.1594/PANGAEA.944393.

Angot, H, **Dastoor, A**, **De Simone, F**, **Gårdfeldt, K**, **Gencarelli, CN**, **Hedgecock, IM**, **Langer, S**, **Magand, O**, **Mastromonaco, MN**, **Nordstrøm, C**, **Pfaffhuber, KA**, **Pirrone, N**, **Ryjkov, A**, **Selin, NE**, **Skov, H**, **Song, S**, **Sprovieri, F**, **Steffen, A**, **Toyota, K**, **Travnikov, O**, **Yang, X**, **Dommergue, A.** 2016. Chemical cycling and deposition of atmospheric mercury in polar regions: Review of recent measurements and comparison with models. *Atmospheric Chemistry and Physics* **16**(16): 10735–10763. DOI: http://dx.doi.org/10.5194/acp-16-10735-2016.

Araujo, BF, **Osterwalder, S**, **Szponar, N**, **Lee, D**, **Petrova, MV**, **Pernov, JB**, **Ahmed, S**, **Heimbürger-Boavida, LE**, **Laffont, L**, **Teisserenc, R**, **Tananaev, N**, **Nordstrom, C**, **Magand, O**, **Stupple, G**, **Skov, H**, **Steffen, A**, **Bergquist, B**, **Pfaffhuber, KA**, **Thomas, JL**, **Scheper, S**, **Petäjä, T**, **Dommergue, A**, **Sonke, JE.** 2022. Mercury isotope evidence for Arctic summertime re-emission of mercury from the cryosphere. *Nature Communications* **13**(1): 4956. DOI: http://dx.doi.org/10.1038/s41467-022-32440-8.

Arctic Monitoring and Assessment Programme. 2011. *AMAP Assessment 2011: Mercury in the Arctic. Arctic Monitoring and Assessment Programme (AMAP).* Oslo, Norway: AMAP: 194.

Arctic Monitoring and Assessment Programme. 2021. *Arctic Monitoring and Assessment Programme (AMAP).* Tromsø, Norway: AMAP: 326.

Arctic Monitoring and Assessment Programme/UN Environment. 2019. *Technical Background Report for the Global Mercury Assessment 2018. Arctic Monitoring and Assessment Programme, Oslo, Norway/UN Environment Programme, Chemicals and Health Branch.* Geneva, Switzerland: AMAP/UN Environment: viii + 426.

Ariya, PA, **Amyot, M**, **Dastoor, A**, **Deeds, D**, **Feinberg, A**, **Kos, G**, **Poulain, A**, **Ryjkov, A**, **Semeniuk, K**, **Subir, M**, **Toyota, K.** 2015. Mercury physicochemical and biogeochemical transformation in the atmosphere and at atmospheric interfaces: A review and future directions. *Chemical Reviews* **115**(10): 3760–3802. DOI: http://dx.doi.org/10.1021/cr500667e.

Balabanov, NB, **Shepler, BC**, **Peterson, KA.** 2005. Accurate global potential energy surface and reaction dynamics for the ground state of $HgBr_2$. *The Journal of Physical Chemistry A* **109**(39): 8765–8773. DOI: http://dx.doi.org/10.1021/jp053415l.

Barrie, LA. 1986. Arctic air pollution: An overview of current knowledge. *Atmospheric Environment* **20**(4): 643–663. DOI: http://dx.doi.org/10.1016/0004-6981(86)90180-0.

Barrie, LA, **Bottenheim, JW**, **Schnell, RC**, **Crutzen, PJ**, **Rasmussen, RA.** 1988. Ozone destruction and photochemical reactions at polar sunrise in the lower Arctic atmosphere. *Nature* **334**(6178): 138–141. DOI: http://dx.doi.org/10.1038/334138a0.

Benavent, N. 2020. Desarrollo de un instrumento MAX-DOAS para medidas urbanas de calidad del aire y de gases traza en la atmósfera polar [PhD thesis]. Universidad Politécnica de Madrid Escuela. DOI: http://dx.doi.org/10.20868/UPM.thesis.65998.

Benavent, N, **Mahajan, AS**, **Li, Q**, **Cuevas, CA**, **Schmale, J**, **Angot, H**, **Jokinen, T**, **Quéléver, LLJ**, **Blechschmidt, AM**, **Zilker, B**, **Richter, A**, **Serna, JA**, **Garcia-**

Nieto, D, **Fernandez, RP**, **Skov, H**, **Dumitrascu, A**, **Simões Pereira, P**, **Abrahamsson, K**, **Bucci, S**, **Duetsch, M**, **Stohl, A**, **Beck, I**, **Laurila, T**, **Blomquist, B**, **Howard, D**, **Archer, SD**, **Bariteau, L**, **Helmig, D**, **Hueber, J**, **Jacobi, HW**, **Posman, K**, **Dada, L**, **Daellenbach, KR**, **Saiz-Lopez, A**. 2022. Substantial contribution of iodine to Arctic ozone destruction. *Nature Geoscience*. DOI: http://dx.doi.org/10.1038/s41561-022-01018-w.

Berg, LK, **Shrivastava, M**, **Easter, RC**, **Fast, JD**, **Chapman, EG**, **Liu, Y**, **Ferrare, RA.** 2015. A new WRF-Chem treatment for studying regional-scale impacts of cloud processes on aerosol and trace gases in parameterized cumuli. *Geoscientific Model Development* **8**(2): 409–429. DOI: http://dx.doi.org/10.5194/gmd-8-409-2015.

Berg, T, **Pfaffhuber, KA**, **Cole, AS**, **Engelsen, O**, **Steffen, A.** 2013. Ten-year trends in atmospheric mercury concentrations, meteorological effects and climate variables at Zeppelin, Ny-Ålesund. *Atmospheric Chemistry and Physics* **13**(13): 6575–6586. DOI: http://dx.doi.org/10.5194/acp-13-6575-2013.

Bottenheim, JW, **Barrie, LA**, **Atlas, E**, **Heidt, LE**, **Niki, H**, **Rasmussen, RA**, **Shepson, PB.** 1990. Depletion of lower tropospheric ozone during Arctic spring: The Polar Sunrise Experiment 1988. *Journal of Geophysical Research: Atmospheres* **95**(D11): 18555–18568. DOI: http://dx.doi.org/10.1029/JD095iD11p18555.

Brooks, SB, **Saiz-Lopez, A**, **Skov, H**, **Lindberg, SE**, **Plane, JMC**, **Goodsite, ME.** 2006. The mass balance of mercury in the springtime arctic environment. *Geo-Physical Research Letters* **33**(13). DOI: http://dx.doi.org/10.1029/2005GL025525.

Buchholz, RR, **Emmons, LK**, **Tilmes, S**, **The CESM2 Development Team**. 2019. CESM2.1/CAM-chem Instantaneous Output for Boundary Conditions. Subset used Lat: 0 to 90, Lon: 0 to 360, March 2020–May 2020. UCAR/NCAR–Atmospheric Chemistry Observations and Modeling Laboratory. DOI: http://dx.doi.org/10.5065/NMP7-EP60. Accessed May 1, 2020.

Carter, WPL. 2000. Documentation of the SAPRC-99 chemical mechanism for VOC reactivity assessment. *Final Report to California Air Resources Board* **92**(329): 95–308.

Clever, HL, **Johnson, SA**, **Derrick, ME.** 1985. The solubility of mercury and some sparingly soluble mercury salts in water and aqueous electrolyte solutions. *Journal of Physical and Chemical Reference Data* **14**(3): 631–680. DOI: http://dx.doi.org/10.1063/1.555732.

Cobbett, FD, **Steffen, A**, **Lawson, G**, **Van Heyst, BJ.** 2007. GEM fluxes and atmospheric mercury concentrations (GEM, RGM and Hgp) in the Canadian Arctic at Alert, Nunavut, Canada (February–June 2005). *Atmospheric Environment* **41**(31): 6527–6543. DOI: http://dx.doi.org/10.1016/j.atmosenv.2007.04.033.

Dada, L, **Angot, H**, **Beck, I**, **Baccarini, A**, **Quéléver, LLJ**, **Boyer, M**, **Laurila, T**, **Brasseur, Z**, **Jozef, G**, **de Boer, G**, **Shupe, MD**, **Henning, S**, **Bucci, S**, **Dütsch, M**, **Stohl, A**, **Petäjä, T**, **Daellenbach, KR**, **Jokinen, T**, **Schmale, J.** 2022. A central Arctic extreme aerosol event triggered by a warm air-mass intrusion. *Nature Communications* **13**(1): 5290.

Dastoor, A, **Angot, H**, **Bieser, J**, **Christensen, JH**, **Douglas, TA**, **Heimbürger-Boavida, LE**, **Jiskra, M**, **Mason, RP**, **McLagan, DS**, **Obrist, D**, **Outridge, PM**, **Petrova, MV**, **Ryjkov, A**, **St Pierre, KA**, **Schartup, AT**, **Soerensen, AL**, **Toyota, K**, **Travnikov, O**, **Wilson, SJ**, **Zdanowicz, C.** 2022a. Arctic mercury cycling. *Nature Reviews Earth & Environment* **3**(4): 270–286. DOI: http://dx.doi.org/10.1038/s43017-022-00269-w.

Dastoor, A, **Wilson, SJ**, **Travnikov, O**, **Ryjkov, A**, **Angot, H**, **Christensen, JH**, **Steenhuisen, F**, **Muntean, M.** 2022b. Arctic atmospheric mercury: Sources and changes. *Science of The Total Environment* **839**: 156213. DOI: http://dx.doi.org/10.1016/j.scitotenv.2022.156213.

Dibble, TS, **Tetu, HL**, **Jiao, Y**, **Thackray, CP**, **Jacob, DJ.** 2020. Modeling the OH-initiated oxidation of mercury in the global atmosphere without violating physical laws. *The Journal of Physical Chemistry A* **124**(2): 444–453. DOI: http://dx.doi.org/10.1021/acs.jpca.9b10121.

Dibble, TS, **Zelie, MJ**, **Mao, H.** 2012. Thermodynamics of reactions of ClHg and BrHg radicals with atmospherically abundant free radicals. *Atmospheric Chemistry and Physics* **12**(21): 10271–10279. DOI: http://dx.doi.org/10.5194/acp-12-10271-2012.

Dommergue, A, **Bahlmann, E**, **Ebinghaus, R**, **Ferrari, C**, **Boutron, C.** 2007. Laboratory simulation of Hg(0) emissions from a snowpack. *Analytical and Bioanalytical Chemistry* **388**(2): 319–327. DOI: http://dx.doi.org/10.1007/s00216-007-1186-2.

Dommergue, A, **Ferrari, CP**, **Poissant, L**, **Gauchard, PA**, **Boutron, CF.** 2003. Diurnal cycles of gaseous mercury within the snowpack at Kuujjuarapik/Whapmagoostui, Québec, Canada. *Environmental Science & Technology* **37**(15): 3289–3297. DOI: http://dx.doi.org/10.1021/es026242b.

Dommergue, A, **Larose, C**, **Fan, X**, **Clarisse, O**, **Foucher, D**, **Hintelmann, H**, **Schneider, D**, **Ferrari, CP.** 2010. Deposition of mercury species in the Ny-Ålesund area (79°N) and their transfer during snowmelt. *Environmental Science & Technology* **44**(3): 901–907. DOI: http://dx.doi.org/10.1021/es902579m.

Douglas, TA, **Blum, JD.** 2019. Mercury isotopes reveal atmospheric gaseous mercury deposition directly to the Arctic coastal snowpack. *Environmental Science & Technology Letters* **6**(4): 235–242. DOI: http://dx.doi.org/10.1021/acs.estlett.9b00131.

Douglas, TA, **Loseto, LL**, **Macdonald, RW**, **Outridge, P**, **Dommergue, A**, **Poulain, A**, **Amyot, M**, **Barkay, T**, **Berg, T**, **Chételat, J**, **Constant, P**, **Evans, M**, **Ferrari, C**, **Gantner, N**, **Johnson, MS**, **Kirk, J**, **Kroer, N**, **Larose, C**, **Lean, D**, **Nielsen, TG**, **Poissant, L**, **Rognerud, S**, **Skov, H**, **Sørensen, S**, **Wang, F**, **Wilson, S**, **Zdanowicz, CM.** 2012. The fate of mercury in

Arctic terrestrial and aquatic ecosystems, a review. *Environmental Chemistry* **9**(4): 321–355.

Driscoll, CT, **Mason, RP**, **Chan, HM**, **Jacob, DJ**, **Pirrone, N.** 2013. Mercury as a global pollutant: Sources, pathways, and effects. *Environmental Science & Technology* **47**(10): 4967–4983. DOI: http://dx.doi.org/10.1021/es305071v.

Durnford, D, **Dastoor, A.** 2011. The behavior of mercury in the cryosphere: A review of what we know from observations. *Journal of Geophysical Research: Atmospheres* **116**(D6). DOI: http://dx.doi.org/10.1029/2010JD014809.

Durnford, D, **Dastoor, A**, **Figueras-Nieto, D**, **Ryjkov, A.** 2010. Long range transport of mercury to the Arctic and across Canada. *Atmospheric Chemistry and Physics* **10**(13): 6063–6086.

Durnford, D, **Dastoor, A**, **Ryzhkov, A**, **Poissant, L**, **Pilote, M**, **Figueras-Nieto, D.** 2012. How relevant is the deposition of mercury onto snowpacks?—Part 2: A modeling study. *Atmospheric Chemistry and Physics* **12**(19): 9251–9274. DOI: http://dx.doi.org/10.5194/acp-12-9251-2012.

Emmons, LK, **Schwantes, RH**, **Orlando, JJ**, **Tyndall, G**, **Kinnison, D**, **Lamarque, JF**, **Marsh, D**, **Mills, MJ**, **Tilmes, S**, **Bardeen, C**, **Buchholz, RR**, **Conley, A**, **Gettelman, A**, **Garcia, R**, **Simpson, I**, **Blake, DR**, **Meinardi, S**, **Pétron, G**. 2020. The chemistry mechanism in the community earth system model version 2 (CESM2). *Journal of Advances in Modeling Earth Systems* **12**(4): e2019MS001882. DOI: http://dx.doi.org/10.1029/2019MS001882.

EU Copernicus Marine Service Information. 2022. Arctic Ocean Physics Reanalysis. DOI: http://dx.doi.org/10.48670/moi-00007.

Falk, S, **Sinnhuber, BM.** 2018. Polar boundary layer bromine explosion and ozone depletion events in the chemistry–climate model EMAC v2.52: Implementation and evaluation of AirSnow algorithm. *Geoscientific Model Development* **11**(3): 1115–1131. DOI: http://dx.doi.org/10.5194/gmd-11-1115-2018.

Fayt, C, **De Smedt, I**, **Letocart, V**, **Merlaud, A**, **Pinardi, G**, **Van Roozendael, M**. 2011. *QDOAS 1.00 Software user manual*. Belgian Institute for Space Aeronomy.

Fernandez, RP, **Carmona-Balea, A**, **Cuevas, CA**, **Barrera, JA**, **Kinnison, DE**, **Lamarque, JF**, **Blaszczak-Boxe, C**, **Kim, K**, **Choi, W**, **Hay, T**, **Blechschmidt, AM**, **Schönhardt, A**, **Burrows, JP**, **Saiz-Lopez, A.** 2019. Modeling the sources and chemistry of polar tropospheric halogens (Cl, Br, and I) using the CAM-Chem global chemistry-climate model. *Journal of Advances in Modeling Earth Systems* **11**(7): 2259–2289.

Ferrari, CP, **Gauchard, PA**, **Aspmo, K**, **Dommergue, A**, **Magand, O**, **Bahlmann, E**, **Nagorski, S**, **Temme, C**, **Ebinghaus, R**, **Steffen, A**, **Banic, C**, **Berg, T**, **Planchon, F**, **Barbante, C**, **Cescon, P**, **Boutron, CF.** 2005. Snow-to-air exchanges of mercury in an Arctic seasonal snow pack in Ny-Ålesund, Svalbard. *Atmospheric Environment* **39**(39): 7633–7645. DOI: http://dx.doi.org/10.1016/j.atmosenv.2005.06.058.

Ferrari, CP, **Padova, C**, **Fan, X**, **Gauchard, PA**, **Dommergue, A**, **Aspmo, K**, **Berg, T**, **Cairns, W**, **Barbante, C**, **Cescon, P**, **Kaleschke, L**, **Richter, A**, **Wittrock, F**, **Boutron, C.** 2008. Atmospheric mercury depletion event study in Ny-Ålesund (Svalbard) in spring 2005. Deposition and transformation of Hg in surface snow during springtime. *Science of The Total Environment* **397**(1): 167–177. DOI: http://dx.doi.org/10.1016/j.scitotenv.2008.01.064.

Fisher, JA, **Jacob, DJ**, **Soerensen, AL**, **Amos, HM**, **Corbitt, ES**, **Streets, DG**, **Wang, Q**, **Yantosca, RM**, **Sunderland, EM.** 2013. Factors driving mercury variability in the Arctic atmosphere and ocean over the past 30 years. *Global Biogeochemical Cycles* **27**(4): 1226–1235. DOI: http://dx.doi.org/10.1002/2013GB004689.

Fisher, JA, **Jacob, DJ**, **Soerensen, AL**, **Amos, HM**, **Steffen, A**, **Sunderland, EM.** 2012. Riverine source of Arctic Ocean mercury inferred from atmospheric observations. *Nature Geoscience* **5**(7): 499–504. DOI: http://dx.doi.org/10.1038/ngeo1478.

Francés-Monerris, A, **Carmona-Garca, J**, **Acuña, AU**, **Dávalos, JZ**, **Cuevas, CA**, **Kinnison, DE**, **Francisco, JS**, **Saiz-Lopez, A**, **Roca-Sanjuán, D.** 2020. Photodissociation mechanisms of major mercury(II) species in the atmospheric chemical cycle of mercury. *Angewandte Chemie International Edition* **59**(19): 7605–7610. DOI: http://dx.doi.org/10.1002/anie.201915656.

Gencarelli, CN, **De Simone, F**, **Hedgecock, IM**, **Sprovieri, F**, **Pirrone, N.** 2014. Development and application of a regional-scale atmospheric mercury model based on WRF/Chem: A Mediterranean area investigation. *Environmental Science and Pollution Research* **21**(6): 4095–4109. DOI: http://dx.doi.org/10.1007/s11356-013-2162-3.

Gómez Martn, JC, **Lewis, TR**, **Douglas, KM**, **Blitz, MA**, **Saiz-Lopez, A**, **Plane, JMC.** 2022. The reaction between HgBr and O_3: Kinetic study and atmospheric implications. *Physical Chemistry Chemical Physics* **24**: 12419–12432. DOI: http://dx.doi.org/10.1039/D2CP00754A.

Goodsite, ME, **Plane, JMC**, **Skov, H.** 2004. A theoretical study of the oxidation of Hg0 to $HgBr_2$ in the troposphere. *Environmental Science & Technology* **38**(6): 1772–1776. DOI: http://dx.doi.org/10.1021/es034680s.

Goodsite, ME, **Plane, JMC**, **Skov, H.** 2012. Correction to a theoretical study of the oxidation of Hg0 to $HgBr_2$ in the troposphere. *Environmental Science & Technology* **46**(9): 5262–5262. DOI: http://dx.doi.org/10.1021/es301201c.

Graham, RM, **Cohen, L**, **Ritzhaupt, N**, **Segger, B**, **Graversen, RG**, **Rinke, A**, **Walden, VP**, **Granskog, MA**, **Hudson, SR.** 2019. Evaluation of six atmospheric reanalyses over Arctic sea ice from winter to early summer. *Journal of Climate* **32**(14): 4121–4143. DOI: http://dx.doi.org/10.1175/JCLI-D-18-0643.1.

Guenther, AB, **Jiang, X**, **Heald, CL**, **Sakulyanontvittaya, T**, **Duhl, T**, **Emmons, LK**, **Wang, X.** 2012. The

Model of Emissions of Gases and Aerosols from Nature version 2.1 (MEGAN2.1): An extended and updated framework for modeling biogenic emissions. *Geoscientific Model Development* **5**(6): 1471–1492. DOI: http://dx.doi.org/10.5194/gmd-5-1471-2012.

Gustin, MS, **Amos, HM**, **Huang, J**, **Miller, MB**, **Heidecorn, K.** 2015. Measuring and modeling mercury in the atmosphere: A critical review. *Atmospheric Chemistry and Physics* **15**(10): 5697–5713. DOI: http://dx.doi.org/10.5194/acp-15-5697-2015.

Gustin, MS, **Huang, J**, **Miller, MB**, **Peterson, C**, **Jaffe, DA**, **Ambrose, J**, **Finley, BD**, **Lyman, SN**, **Call, K**, **Talbot, R**, **Feddersen, D**, **Mao, H**, **Lindberg, SE.** 2013. Do we understand what the mercury speciation instruments are actually measuring? Results of RAMIX. *Environmental Science & Technology* **47**(13): 7295–7306. DOI: http://dx.doi.org/10.1021/es3039104.

Halfacre, JW, **Knepp, TN**, **Shepson, PB**, **Thompson, CR**, **Pratt, KA**, **Li, B**, **Peterson, PK**, **Walsh, SJ**, **Simpson, WR**, **Matrai, PA**, **Bottenheim, JW**, **Netcheva, S**, **Perovich, DK**, **Richter, A.** 2014. Temporal and spatial characteristics of ozone depletion events from measurements in the Arctic. *Atmospheric Chemistry and Physics* **14**(10): 4875–4894. DOI: http://dx.doi.org/10.5194/acp-14-4875-2014.

Herrmann, M, **Schöne, M**, **Borger, C**, **Warnach, S**, **Wagner, T**, **Platt, U**, **Gutheil, E.** 2022. Ozone depletion events in the Arctic spring of 2019: A new modeling approach to bromine emissions. *Atmospheric Chemistry and Physics* **22**(20): 13495–13526. DOI: http://dx.doi.org/10.5194/acp-22-13495-2022; https://acp.copernicus.org/articles/22/13495/2022/.

Herrmann, M, **Sihler, H**, **Frieß, U**, **Wagner, T**, **Platt, U**, **Gutheil, E.** 2021. Time-dependent 3D simulations of tropospheric ozone depletion events in the Arctic spring using the Weather Research and Forecasting model coupled with Chemistry (WRF-Chem). *Atmospheric Chemistry and Physics* **21**(10): 7611–7638. DOI: http://dx.doi.org/10.5194/acp-21-7611-2021.

Hintelmann, H, **Graydon, JA**, **Kirk, JL**, **Barker, J**, **Dimock, B**, **Sharp, MJ**, **Lehnherr, I.** 2007. Methylated mercury species in Canadian high Arctic marine surface waters and snowpacks. *Environmental Science & Technology* **41**(18): 6433–6441. DOI: http://dx.doi.org/10.1021/es070692s.

Holmes, CD, **Jacob, DJ**, **Corbitt, ES**, **Mao, J**, **Yang, X**, **Talbot, R**, **Slemr, F.** 2010. Global atmospheric model for mercury including oxidation by bromine atoms. *Atmospheric Chemistry and Physics* **10**(24): 12037–12057. DOI: http://dx.doi.org/10.5194/acp-10-12037-2010.

Hönninger, G, **Platt, U.** 2002. Observations of BrO and its vertical distribution during surface ozone depletion at Alert. *Atmospheric Environment* **36**(15): 2481–2489. DOI: http://dx.doi.org/10.1016/S1352-2310(02)00104-8.

Horowitz, HM, **Jacob, DJ**, **Zhang, Y**, **Dibble, TS**, **Slemr, F**, **Amos, HM**, **Schmidt, JA**, **Corbitt, ES**, **Marais, EA**, **Sunderland, EM.** 2017. A new mechanism for atmospheric mercury redox chemistry: Implications for the global mercury budget. *Atmospheric Chemistry and Physics* **17**(10): 6353–6371. DOI: http://dx.doi.org/10.5194/acp-17-6353-2017.

Huang, J, **Jaeglé, L.** 2017. Wintertime enhancements of sea salt aerosol in polar regions consistent with a sea ice source from blowing snow. *Atmospheric Chemistry and Physics* **17**(5): 3699–3712. DOI: http://dx.doi.org/10.5194/acp-17-3699-2017.

Huang, J, **Jaeglé, L**, **Chen, Q**, **Alexander, B**, **Sherwen, T**, **Evans, MJ**, **Theys, N**, **Choi, S.** 2020. Evaluating the impact of blowing-snow sea salt aerosol on springtime BrO and O_3 in the Arctic. *Atmospheric Chemistry and Physics* **20**(12): 7335–7358. DOI: http://dx.doi.org/10.5194/acp-20-7335-2020.

Huang, J, **Jaeglé, L**, **Shah, V.** 2018. Using CALIOP to constrain blowing snow emissions of sea salt aerosols over Arctic and Antarctic sea ice. *Atmospheric Chemistry and Physics* **18**(22): 16253–16269. DOI: http://dx.doi.org/10.5194/acp-18-16253-2018.

Huang, J, **Miller, MB**, **Weiss-Penzias, P**, **Gustin, MS.** 2013. Comparison of gaseous oxidized Hg measured by KCl-coated denuders, and nylon and cation exchange membranes. *Environmental Science & Technology* **47**(13): 7307–7316. DOI: http://dx.doi.org/10.1021/es4012349.

Hynes, AJ, **Donohoue, DL**, **Goodsite, ME**, **Hedgecock, IM.** 2009. *Our current understanding of major chemical and physical processes affecting mercury dynamics in the atmosphere and at the air-water/terrestrial interfaces*. Boston, MA: Springer US. DOI: http://dx.doi.org/10.1007/978-0-387-93958-2_14.

Iacono, MJ, **Delamere, JS**, **Mlawer, EJ**, **Shephard, MW**, **Clough, SA**, **Collins, WD.** 2008. Radiative forcing by long-lived greenhouse gases: Calculations with the AER radiative transfer models. *Journal of Geophysical Research: Atmospheres* **113**(D1303). DOI: http://dx.doi.org/10.1029/2008JD009944.

Jacob, DJ. 2000. Heterogeneous chemistry and tropospheric ozone. *Atmospheric Environment* **34**(12): 2131–2159. DOI: http://dx.doi.org/10.1016/S1352-2310(99)00462-8.

Kalnay, E, **Kanamitsu, M**, **Kistler, R**, **Collins, W**, **Deaven, D**, **Gandin, L**, **Iredell, M**, **Saha, S**, **White, G**, **Woollen, J**, **Zhu, Y**, **Chelliah, M**, **Ebisuzaki, W**, **Higgins, W**, **Janowiak, J**, **Mo, KC**, **Ropelewski, C**, **Wang, J**, **Leetmaa, A**, **Reynolds, R**, **Jenne, R**, **Joseph, D.** 1996. The NCEP/NCAR 40-Year Reanalysis Project. *Bulletin of the American Meteorological Society* **77**(3): 437–472. DOI: http://dx.doi.org/10.1175/1520-0477(1996)077<0437:TNYRP>2.0.CO;2.

Kamp, J, **Skov, H**, **Jensen, B**, **Sørensen, LL.** 2018. Fluxes of gaseous elemental mercury (GEM) in the high Arctic during atmospheric mercury depletion events (AMDEs). *Atmospheric Chemistry and Physics* **18**(9):

6923–6938. DOI: http://dx.doi.org/10.5194/acp-18-6923-2018.

Khiri, D, **Louis, F**, **Černušák, I**, **Dibble, TS**. 2020. BrHgO*+ CO: Analogue of OH + CO and reduction path for Hg(II) in the atmosphere. *ACS Earth and Space Chemistry* **4**(10): 1777–1784. DOI: http://dx.doi.org/10.1021/acsearthspacechem.0c00171.

Kirk, JL, **St Louis, VL**, **Sharp, MJ.** 2006. Rapid reduction and reemission of mercury deposited into snowpacks during atmospheric mercury depletion events at Churchill, Manitoba, Canada. *Environmental Science & Technology* **40**(24): 7590–7596. DOI: http://dx.doi.org/10.1021/es061299+.

Klimont, Z, **Kupiainen, K**, **Heyes, C**, **Purohit, P**, **Cofala, J**, **Rafaj, P**, **Borken-Kleefeld, J**, **Schöpp, W.** 2017. Global anthropogenic emissions of particulate matter including black carbon. *Atmospheric Chemistry and Physics* **17**(14): 8681–8723. DOI: http://dx.doi.org/10.5194/acp-17-8681-2017.

Knepp, TN, **Bottenheim, J**, **Carlsen, M**, **Carlson, D**, **Donohoue, D**, **Friederich, G**, **Matrai, PA**, **Netcheva, S**, **Perovich, DK**, **Santini, R**, **Shepson, PB**, **Simpson, W**, **Valentic, T**, **Williams, C**, **Wyss, PJ.** 2010. Development of an autonomous sea ice tethered buoy for the study of ocean-atmosphere-sea ice-snow pack interactions: The O-buoy. *Atmospheric Measurement Techniques* **3**(1): 249–261. DOI: http://dx.doi.org/10.5194/amt-3-249-2010.

Knust, R. 2017. Polar research and supply vessel POLARSTERN operated by the Alfred-Wegener-Institute. *Journal of Large-Scale Research Facilities* **3**: A119. DOI: http://dx.doi.org/10.17815/jlsrf-3-163.

Krnavek, L, **Simpson, WR**, **Carlson, D**, **Domine, F**, **Douglas, TA**, **Sturm, M.** 2012. The chemical composition of surface snow in the Arctic: Examining marine, terrestrial, and atmospheric influences. *Atmospheric Environment* **50**: 349–359. DOI: http://dx.doi.org/10.1016/j.atmosenv.2011.11.033.

Lalonde, JD, **Amyot, M**, **Doyon, MR**, **Auclair, JC.** 2003. Photo-induced Hg(II) reduction in snow from the remote and temperate Experimental Lakes Area (Ontario, Canada). *Journal of Geophysical Research: Atmospheres* **108**(D6). DOI: http://dx.doi.org/10.1029/2001JD001534.

Lalonde, JD, **Poulain, AJ**, **Amyot, M.** 2002. The role of mercury redox reactions in snow on snow-to-air mercury transfer. *Environmental Science & Technology* **36**(2): 174–178. DOI: http://dx.doi.org/10.1021/es010786g.

Lehnherr, I, **St Louis, VL.** 2009. Importance of ultraviolet radiation in the photodemethylation of methylmercury in freshwater ecosystems. *Environmental Science & Technology* **43**(15): 5692–5698. DOI: http://dx.doi.org/10.1021/es9002923.

Lindberg, SE, **Brooks, S**, **Lin, CJ**, **Scott, KJ**, **Landis, MS**, **Stevens, RK**, **Goodsite, M**, **Richter, A.** 2002. Dynamic oxidation of gaseous mercury in the Arctic troposphere at polar sunrise. *Environmental Science & Technology* **36**(6): 1245–1256. DOI: http://dx.doi.org/10.1021/es0111941.

Lindberg, SE, **Brooks, S**, **Lin, CJ**, **Scott, K**, **Meyers, T**, **Chambers, L**, **Landis, M**, **Stevens, R.** 2001. Formation of reactive gaseous mercury in the Arctic: Evidence of oxidation of Hg^{o} to gas-phase Hg-II compounds after Arctic sunrise. *Water, Air and Soil Pollution: Focus* **1**(5): 295–302. DOI: http://dx.doi.org/10.1023/A:1013171509022.

Lindberg, SE, **Stratton, WJ.** 1998. Atmospheric mercury speciation: Concentrations and behavior of reactive gaseous mercury in ambient air. *Environmental Science & Technology* **32**(1): 49–57. DOI: http://dx.doi.org/10.1021/es970546u.

Lindqvist, O, **Rodhe, H.** 1985. Atmospheric mercury—A review. *Tellus B* **37B**(3): 136–159. DOI: http://dx.doi.org/10.1111/j.1600-0889.1985.tb00062.x.

Lohberger, F, **Hönninger, G**, **Platt, U.** 2004. Ground-based imaging differential optical absorption spectroscopy of atmospheric gases. *Applied Optics* **43**(24): 4711–4717. DOI: http://dx.doi.org/10.1364/AO.43.004711.

Lu, JY, **Schroeder, WH**, **Barrie, LA**, **Steffen, A**, **Welch, HE**, **Martin, K**, **Lockhart, L**, **Hunt, RV**, **Boila, G**, **Richter, A.** 2001. Magnification of atmospheric mercury deposition to polar regions in springtime: The link to tropospheric ozone depletion chemistry. *Geophysical Research Letters* **28**(17): 3219–3222. DOI: http://dx.doi.org/10.1029/2000GL012603.

MacSween, K, **Stupple, G**, **Aas, W**, **Kyllönen, K**, **Pfaffhuber, KA**, **Skov, H**, **Steffen, A**, **Berg, T**, **Mastromonaco, MN.** 2022. Updated trends for atmospheric mercury in the Arctic: 1995–2018. *Science of The Total Environment* **837**: 155802. DOI: http://dx.doi.org/10.1016/j.scitotenv.2022.155802.

Mahajan, AS. 2022. Substantial contribution of iodine to Arctic ozone destruction–data. Mendeley Data, V1. DOI: http://dx.doi.org/10.17632/bn7ytz4mfz.1.

Manca, G, **Ammoscato, I**, **Esposito, G**, **Ianniello, A**, **Nardino, M**, **Sprovieri, F.** 2013. Dynamics of snow-air mercury exchange at Ny Ålesund during springtime 2011. *E3 S Web of Conferences* **1**: 03010. DOI: http://dx.doi.org/10.1051/e3sconf/20130103010.

Mann, E, **Mallory, M**, **Ziegler, S**, **Tordon, R**, **O'Driscoll, N.** 2015a. Mercury in Arctic snow: Quantifying the kinetics of photochemical oxidation and reduction. *Science of The Total Environment* **509–510**: 115–132. DOI: http://dx.doi.org/10.1016/j.scitotenv.2014.07.056.

Mann, E, **Mallory, ML**, **Ziegler, SE**, **Avery, TS**, **Tordon, R**, **O'Driscoll, N.** 2015b. Photoreducible mercury loss from Arctic snow is influenced by temperature and snow age. *Environmental Science & Technology* **49**(20): 12120–12126. DOI: http://dx.doi.org/10.1021/acs.est.5b01589.

Mann, E, **Ziegler, S**, **Steffen, A**, **O'Driscoll, N.** 2018. Increasing chloride concentration causes retention of mercury in melted Arctic snow due to changes in photoreduction kinetics. *Journal of Environmental Sciences* **68**: 122–129. DOI: http://dx.doi.org/10.1016/j.jes.2018.01.006.

Marelle, L, **Raut, JC**, **Law, KS**, **Berg, LK**, **Fast, JD**, **Easter, RC**, **Shrivastava, M**, **Thomas, JL.** 2017. Improvements to the WRF-Chem 3.5.1 model for quasihemispheric simulations of aerosols and ozone in the Arctic. *Geoscientific Model Development* **10**(10): 3661–3677. DOI: http://dx.doi.org/10.5194/gmd-10-3661-2017.

Marelle, L, **Thomas, JL**, **Ahmed, S**, **Tuite, K**, **Stutz, J**, **Dommergue, A**, **Simpson, WR**, **Frey, MM**, **Baladima, F**. 2021. Implementation and impacts of surface and blowing snow sources of Arctic bromine activation within WRF-Chem 4.1.1. *Journal of Advances in Modeling Earth Systems* **13**: e2020MS002391. DOI: http://dx.doi.org/10.1029/2020MS002391.

Maturilli, M, **Holdridge, DJ**, **Dahlke, S**, **Graeser, J**, **Sommerfeld, A**, **Jaiser, R**, **Deckelmann, H**, **Schulz, A.** 2021. Initial radiosonde data from 2019-10 to 2020-09 during project MOSAiC. PANGAEA. DOI: http://dx.doi.org/10.1594/PANGAEA.928656.

Morrison, H, **Thompson, G**, **Tatarskii, V.** 2009. Impact of cloud microphysics on the development of trailing stratiform precipitation in a simulated squall line: Comparison of one- and two-moment schemes. *Monthly Weather Review* **137**(3): 991–1007. DOI: http://dx.doi.org/10.1175/2008MWR2556.1.

Nakanishi, M, **Niino, H.** 2009. Development of an improved turbulence closure model for the atmospheric boundary layer. *Journal of the Meteorological Society of Japan* **87**(5): 895–912. DOI: http://dx.doi.org/10.2151/jmsj.87.895.

National Centers for Environmental Prediction. 2000. *NCEP FNL Operational Model Global Tropospheric Analyses, Continuing from July 1999*. Boulder, CO: Research Data Archive at the National Center for Atmospheric Research, Computational and Information Systems Laboratory. DOI: http://dx.doi.org/10.5065/D6M043C6.

Nicolaus, M, **Perovich, DK**, **Spreen, G**, **Granskog, MA**, **von Albedyll, L**, **Angelopoulos, M**, **Anhaus, P**, **Arndt, S**, **Belter, HJ**, **Bessonov, V**, **Birnbaum, G**, **Brauchle, J**, **Calmer, R**, **Cardellach, E**, **Cheng, B**, **Clemens-Sewall, D**, **Dadic, R**, **Damm, E**, **de Boer, G**, **Demir, O**, **Dethloff, K**, **Divine, DV**, **Fong, AA**, **Fons, S**, **Frey, MM**, **Fuchs, N**, **Gabarró, C**, **Gerland, S**, **Goessling, HF**, **Gradinger, R**, **Haapala, J**, **Haas, C**, **Hamilton, J**, **Hannula, HR**, **Hendricks, S**, **Herber, A**, **Heuzé, C**, **Hoppmann, M**, **Høyland, KV**, **Huntemann, M**, **Hutchings, JK**, **Hwang, B**, **Itkin, P**, **Jacobi, HW**, **Jaggi, M**, **Jutila, A**, **Kaleschke, L**, **Katlein, C**, **Kolabutin, N**, **Krampe, D**, **Kristensen, SS**, **Krumpen, T**, **Kurtz, N**, **Lampert, A**, **Lange, BA**, **Lei, R**, **Light, B**, **Linhardt, F**, **Liston, GE**, **Loose, B**, **Macfarlane, AR**, **Mahmud, M**, **Matero, IO**, **Maus, S**, **Morgenstern, A**, **Naderpour, R**, **Nandan, V**, **Niubom, A**, **Oggier, M**, **Oppelt, N**, **Pätzold, F**, **Perron, C**, **Petrovsky, T**, **Pirazzini, R**, **Polashenski, C**, **Rabe, B**, **Raphael, IA**, **Regnery, J**, **Rex, M**, **Ricker, R**, **Riemann-Campe, K**, **Rinke, A**, **Rohde, J**, **Salganik, E**, **Scharien, RK**, **Schiller, M**, **Schneebeli, M**, **Semmling, M**, **Shimanchuk, E**, **Shupe, MD**, **Smith, MM**, **Smolyanitsky, V**, **Sokolov, V**, **Stanton, T**, **Stroeve, J**, **Thielke, L**, **Timofeeva, A**, **Tonboe, RT**, **Tavri, A**, **Tsamados, M**, **Wagner, DN**, **Watkins, D**, **Webster, M**, **Wendisch, M**. 2022. Overview of the MOSAiC expedition: Snow and sea ice. *Elementa: Science of the Anthropocene* **10**(1). DOI: http://dx.doi.org/10.1525/elementa.2021.000046.

Nixdorf, U, **Dethloff, K**, **Rex, M**, **Shupe, M**, **Sommerfeld, A**, **Perovich, D**, **Nicolaus, M**, **Heuzé, C**, **Rabe, B**, **Loose, B**, **Damm, E**, **Gradinger, R**, **Fong, A**, **Maslowski, W**, **Rinke, A**, **Kwok, R**, **Spreen, G**, **Wendisch, M**, **Herber, A**, **Hirsekorn, M**, **Mohaupt, V**, **Frickenhaus, S**, **Immerz, A**, **Weiss-Tuider, K**, **König, B**, **Mengedoht, D**, **Regnery, J**, **Gerchow, P**, **Ransby, D**, **Krumpen, T**, **Morgenstern, A**, **Haas, C**, **Kanzow, T**, **Rack, FR**, **Saitzev, V**, **Sokolov, V**, **Makarov, A**, **Schwarze, S**, **Wunderlich, T**, **Wurr, K**, **Antje, B**. 2021. MOSAiC Extended Acknowledgement. Zenodo. DOI: http://dx.doi.org/10.5281/zenodo.5541624.

Oltmans, SJ. 1981. Surface ozone measurements in clean air. *Journal of Geophysical Research: Oceans* **86**(C2): 1174–1180. DOI: http://dx.doi.org/10.1029/JC086iC02p01174.

Osterwalder, S, **Dunham-Cheatham, SM**, **Ferreira Araujo, B**, **Magand, O**, **Thomas, JL**, **Baladima, F**, **Pfaffhuber, KA**, **Berg, T**, **Zhang, L**, **Huang, J**, **Dommergue, A**, **Sonke, JE**, **Gustin, MS**. 2021. Fate of springtime atmospheric reactive mercury: Concentrations and deposition at Zeppelin, Svalbard. *ACS Earth and Space Chemistry* **5**(11): 3234–3246. DOI: http://dx.doi.org/10.1021/acsearthspacechem.1c00299.

Pearson, C, **Howard, D**, **Moore, C**, **Obrist, D**. 2019. Mercury and trace metal wet deposition across five stations in Alaska: Controlling factors, spatial patterns, and source regions. *Atmospheric Chemistry and Physics* **19**(10): 6913–6929. DOI: http://dx.doi.org/10.5194/acp-19-6913-2019.

Petäjä, T, **Duplissy, EM**, **Tabakova, K**, **Schmale, J**, **Altstädter, B**, **Ancellet, G**, **Arshinov, M**, **Balin, Y**, **Baltensperger, U**, **Bange, J**, **Beamish, A**, **Belan, B**, **Berchet, A**, **Bossi, R**, **Cairns, WRL**, **Ebinghaus, R**, **El Haddad, I**, **Ferreira-Araujo, B**, **Franck, A**, **Huang, L**, **Hyvärinen, A**, **Humbert, A**, **Kalogridis, AC**, **Konstantinov, P**, **Lampert, A**, **MacLeod, M**, **Magand, O**, **Mahura, A**, **Marelle, L**, **Masloboev, V**, **Moisseev, D**, **Moschos, V**, **Neckel, N**, **Onishi, T**, **Osterwalder, S**, **Ovaska, A**, **Paasonen, P**, **Panchenko, M**, **Pankratov, F**, **Pernov, JB**, **Platis, A**, **Popovicheva, O**, **Raut, JC**, **Riandet, A**, **Sachs, T**, **Salvatori, R**, **Salzano, R**, **Schröder, L**, **Schön, M**, **Shevchenko, V**, **Skov, H**, **Sonke, JE**, **Spolaor, A**, **Stathopoulos, VK**, **Strahlendorff, M**, **Thomas, JL**, **Vitale, V**, **Vratolis, S**, **Barbante, C**, **Chabrillat, S**, **Dommergue, A**, **Eleftheriadis, K**, **Heilimo, J**, **Law, KS**, **Massling, A**, **Noe, SM**, **Paris, JD**, **Prévôt, ASH**, **Riipinen, I**, **Wehner, B**, **Xie, Z**, **Lappalainen, HK**. 2020. Overview: Integrative and

Comprehensive Understanding on Polar Environments (iCUPE)—Concept and initial results. *Atmospheric Chemistry and Physics* **20**(14): 8551–8592. DOI: http://dx.doi.org/10.5194/acp-20-8551-2020.

Peterson, PK, **Hartwig, M**, **May, NW**, **Schwartz, E**, **Rigor, I**, **Ermold, W**, **Steele, M**, **Morison, JH**, **Nghiem, SV**, **Pratt, KA**. 2019. Snowpack measurements suggest role for multi-year sea ice regions in Arctic atmospheric bromine and chlorine chemistry. *Elementa: Science of the Anthropocene* **7**(14). DOI: http://dx.doi.org/10.1525/elementa.352.

Peterson, PK, **Pöhler, D**, **Sihler, H**, **Zielcke, J**, **General, S**, **Frieß, U**, **Platt, U**, **Simpson, WR**, **Nghiem, SV**, **Shepson, PB**, **Stirm, BH**, **Dhaniyala, S**, **Wagner, T**, **Caulton, DR**, **Fuentes, JD**, **Pratt, KA**. 2017. Observations of bromine monoxide transport in the Arctic sustained on aerosol particles. *Atmospheric Chemistry and Physics* **17**(12): 7567–7579. DOI: http://dx.doi.org/10.5194/acp-17-7567-2017.

Plane, JM, **Saiz-Lopez, A**. 2006. *UV-Visible Differential Optical Absorption Spectroscopy (DOAS)*. New York, NY: John Wiley & Sons, Ltd. DOI: http://dx.doi.org/10.1002/9780470988510.ch3.

Platt, SM, **Hov, Ø**, **Berg, T**, **Breivik, K**, **Eckhardt, S**, **Eleftheriadis, K**, **Evangeliou, N**, **Fiebig, M**, **Fisher, R**, **Hansen, G**, **Hansson, HC**, **Heintzenberg, J**, **Hermansen, O**, **Heslin-Rees, D**, **Holmén, K**, **Hudson, S**, **Kallenborn, R**, **Krejci, R**, **Krognes, T**, **Larssen, S**, **Lowry, D**, **Lund Myhre, C**, **Lunder, C**, **Nisbet, E**, **Nizzetto, PB**, **Park, KT**, **Pedersen, CA**, **Aspmo Pfaffhuber, K**, **Röckmann, T**, **Schmidbauer, N**, **Solberg, S**, **Stohl, A**, **Ström, J**, **Svendby, T**, **Tunved, P**, **Tørnkvist, K**, **van der Veen, C**, **Vratolis, S**, **Yoon, YJ**, **Yttri, KE**, **Zieger, P**, **Aas, W**, **Tørseth, K**. 2022. Atmospheric composition in the European Arctic and 30 years of the Zeppelin Observatory, Ny-Ålesund. *Atmospheric Chemistry and Physics* **22**(5): 3321–3369. DOI: http://dx.doi.org/10.5194/acp-22-3321-2022.

Platt, U, **Hönninger, G**. 2003. The role of halogen species in the troposphere. *Chemosphere* **52**(2): 325–338. DOI: http://dx.doi.org/10.1016/S0045-6535(03)00216-9.

Platt, U, **Stutz, J**. 2008. *Differential Absorption Spectroscopy*. Berlin, Heidelberg: Springer Berlin Heidelberg. DOI: http://dx.doi.org/10.1007/978-3-540-75776-4_6.

Poissant, L, **Pilote, M**, **Xu, X**, **Zhang, H**, **Beauvais, C**. 2004. Atmospheric mercury speciation and deposition in the Bay St. François wetlands. *Journal of Geophysical Research: Atmospheres* **109**(D11). DOI: http://dx.doi.org/10.1029/2003JD004364.

Poulain, AJ, **Garcia, E**, **Amyot, M**, **Campbell, PG**, **Ariya, PA**. 2007. Mercury distribution, partitioning and speciation in coastal vs. inland high Arctic snow. *Geochimica et Cosmochimica Acta* **71**(14): 3419–3431. DOI: http://dx.doi.org/10.1016/j.gca.2007.05.006.

Poulain, AJ, **Lalonde, JD**, **Amyot, M**, **Shead, JA**, **Raofie, F**, **Ariya, PA**. 2004. Redox transformations of mercury in an Arctic snowpack at springtime. *Atmospheric Environment* **38**(39): 6763–6774. DOI: http://dx.doi.org/10.1016/j.atmosenv.2004.09.013.

Prados-Roman, C, **Cuevas, CA**, **Hay, T**, **Fernandez, RP**, **Mahajan, AS**, **Royer, SJ**, **Gal, M**, **Simó, R**, **Dachs, J**, **Großmann, K**, **Kinnison, DE**, **Lamarque, JF**, **Saiz-Lopez, A**. 2015. Iodine oxide in the global marine boundary layer. *Atmospheric Chemistry and Physics* **15**(2). DOI: http://dx.doi.org/10.5194/acp-15-583-2015.

Prestbo, EM, **Gay, DA**. 2009. Wet deposition of mercury in the U.S. and Canada, 1996–2005: Results and analysis of the NADP mercury deposition network (MDN). *Atmospheric Environment* **43**(27): 4223–4233. DOI: http://dx.doi.org/10.1016/j.atmosenv.2009.05.028.

Rabe, B, **Heuzé, C**, **Regnery, J**, **Aksenov, Y**, **Allerholt, J**, **Athanase, M**, **Bai, Y**, **Basque, C**, **Bauch, D**, **Baumann, TM**, **Chen, D**, **Cole, ST**, **Craw, L**, **Davies, A**, **Damm, E**, **Dethloff, K**, **Divine, DV**, **Doglioni, F**, **Ebert, F**, **Fang, YC**, **Fer, I**, **Fong, AA**, **Gradinger, R**, **Granskog, MA**, **Graupner, R**, **Haas, C**, **He, H**, **He, Y**, **Hoppmann, M**, **Janout, M**, **Kadko, D**, **Kanzow, T**, **Karam, S**, **Kawaguchi, Y**, **Koenig, Z**, **Kong, B**, **Krishfield, RA**, **Krumpen, T**, **Kuhlmey, D**, **Kuznetsov, I**, **Lan, M**, **Laukert, G**, **Lei, R**, **Li, T**, **Torres-Valdés, S**, **Lin, L**, **Lin, L**, **Liu, H**, **Liu, N**, **Loose, B**, **Ma, X**, **McKay, R**, **Mallet, M**, **Mallett, RDC**, **Maslowski, W**, **Mertens, C**, **Mohrholz, V**, **Muilwijk, M**, **Nicolaus, M**, **O'Brien, JK**, **Perovich, D**, **Ren, J**, **Rex, M**, **Ribeiro, N**, **Rinke, A**, **Schaffer, J**, **Schuffenhauer, I**, **Schulz, K**, **Shupe, MD**, **Shaw, W**, **Sokolov, V**, **Sommerfeld, A**, **Spreen, G**, **Stanton, T**, **Stephens, M**, **Su, J**, **Sukhikh, N**, **Sundfjord, A**, **Thomisch, K**, **Tippenhauer, S**, **Toole, JM**, **Vredenborg, M**, **Walter, M**, **Wang, H**, **Wang, L**, **Wang, Y**, **Wendisch, M**, **Zhao, J**, **Zhou, M**, **Zhu, J**. 2022. Overview of the MOSAiC expedition: Physical oceanography. *Elementa: Science of the Anthropocene* **10**(1). DOI: http://dx.doi.org/10.1525/elementa.2021.00062.

Rasmussen, R, **Baker, B**, **Kochendorfer, J**, **Meyers, T**, **Landolt, S**, **Fischer, AP**, **Black, J**, **Thériault, JM**, **Kucera, P**, **Gochis, D**, **Smith, C**, **Nitu, R**, **Hall, M**, **Ikeda, K**, **Gutmann, E**. 2012. How well are we measuring snow: The NOAA/FAA/NCAR winter precipitation test bed. *Bulletin of the American Meteorological Society* **93**(6): 811–829. DOI: http://dx.doi.org/10.1175/BAMS-D-11-00052.1.

Rhodes, RH, **Yang, X**, **Wolff, EW**, **McConnell, JR**, **Frey, MM**. 2017. Sea ice as a source of sea salt aerosol to Greenland ice cores: A model-based study. *Atmospheric Chemistry and Physics* **17**(15): 9417–9433. DOI: http://dx.doi.org/10.5194/acp-17-9417-2017.

Saiz-Lopez, A, **Acuña, AU**, **Trabelsi, T**, **Carmona-Garca, J**, **Dávalos, JZ**, **Rivero, D**, **Cuevas, CA**, **Kinnison, DE**, **Sitkiewicz, SP**, **Roca-Sanjuán, D**, **Francisco, JS**. 2019. Gas-phase photolysis of Hg(I) radical species: A new atmospheric mercury reduction process. *Journal of the American Chemical Society* **141**(22):

8698–8702. DOI: http://dx.doi.org/10.1021/jacs.9b02890.

Saiz-Lopez, A, **Sitkiewicz, SP**, **Roca-Sanjuán, D**, **Oliva-Enrich, JM**, **Dávalos, JZ**, **Notario, R**, **Jiskra, M**, **Xu, Y**, **Wang, F**, **Thackray, CP**, **Sunderland, EM**, **Jacob, DJ**, **Travnikov, O**, **Cuevas, CA**, **Acuña, AU**, **Rivero, D**, **Plane, JMC**, **Kinnison, DE**, **Sonke, JE**. 2018. Photoreduction of gaseous oxidized mercury changes global atmospheric mercury speciation, transport and deposition. *Nature Communications* **9**(1): 4796. DOI: http://dx.doi.org/10.1038/s41467-018-07075-3.

Sandu, A, **Sander, R**. 2006. Technical note: Simulating chemical systems in Fortran90 and Matlab with the Kinetic PreProcessor KPP-2.1. *Atmospheric Chemistry and Physics* **6**(1): 187–195. DOI: http://dx.doi.org/10.5194/acp-6-187-2006.

Sanei, H, **Outridge, P**, **Goodarzi, F**, **Wang, F**, **Armstrong, D**, **Warren, K**, **Fishback, L**. 2010. Wet deposition mercury fluxes in the Canadian sub-Arctic and southern Alberta, measured using an automated precipitation collector adapted to cold regions. *Atmospheric Environment* **44**(13): 1672–1681. DOI: http://dx.doi.org/10.1016/j.atmosenv.2010.01.030.

Schmithüsen, H. 2021. Continuous meteorological surface measurement during POLARSTERN cruise PS122/3. PANGAEA. DOI: http://dx.doi.org/10.1594/PANGAEA.935223.

Schroeder, WH, **Anlauf, KG**, **Barrie, LA**, **Lu, JY**, **Steffen, A**, **Schneeberger, DR**, **Berg, T**. 1998. Arctic springtime depletion of mercury. *Nature* **394**(6691): 331–332. DOI: http://dx.doi.org/10.1038/28530.

Schroeder, WH, **Steffen, A**, **Scott, K**, **Bender, T**, **Prestbo, E**, **Ebinghaus, R**, **Lu, JY**, **Lindberg, SE**. 2003. Summary report: First international Arctic atmospheric mercury research workshop. *Atmospheric Environment* **37**(18): 2551–2555. DOI: http://dx.doi.org/10.1016/S1352-2310(03)00153-5.

Schwartz, SE. 1986. Mass-transport considerations pertinent to aqueous phase reactions of gases in liquid-water clouds, in Jaeschke, W ed., *Chemistry of multiphase atmospheric systems*. Berlin, Heidelberg: Springer Berlin Heidelberg: 415–471.

Seigneur, C, **Vijayaraghavan, K**, **Lohman, K**, **Karamchandani, P**, **Scott, C**. 2004. Global source attribution for mercury deposition in the United States. *Environmental Science & Technology* **38**(2): 555–569. DOI: http://dx.doi.org/10.1021/es034109t.

Selin, NE. 2009. Global biogeochemical cycling of mercury: A review. *Annual Review of Environment and Resources* **34**(1): 43–63. DOI: http://dx.doi.org/10.1146/annurev.environ.051308.084314.

Selin, NE, **Jacob, DJ**, **Yantosca, RM**, **Strode, S**, **Jaeglé, L**, **Sunderland, EM**. 2008. Global 3-D land-ocean-atmosphere model for mercury: Present-day versus preindustrial cycles and anthropogenic enrichment factors for deposition. *Global Biogeochemical Cycles* **22**(2). DOI: http://dx.doi.org/10.1029/2007GB003040.

Seo, S, **Richter, A**, **Blechschmidt, AM**, **Bougoudis, I**, **Burrows, JP**. 2019. First high-resolution BrO column retrievals from TROPOMI. *Atmospheric Measurement Techniques* **12**(5): 2913–2932. DOI: http://dx.doi.org/10.5194/amt-12-2913-2019.

Shah, V, **Jacob, DJ**, **Thackray, CP**, **Wang, X**, **Sunderland, EM**, **Dibble, TS**, **Saiz-Lopez, A**, **Černušák, I**, **Kellö, V**, **Castro, PJ**, **Wu, R**, **Wang, C**. 2021. Improved mechanistic model of the atmospheric redox chemistry of mercury. *Environmental Science & Technology* **55**(21): 14445–14456. DOI: http://dx.doi.org/10.1021/acs.est.1c03160.

Shupe, MD, **Rex, M**, **Blomquist, B**, **Persson, POG**, **Schmale, J**, **Uttal, T**, **Althausen, D**, **Angot, H**, **Archer, S**, **Bariteau, L**, **Beck, I**, **Bilberry, J**, **Bucci, S**, **Buck, C**, **Boyer, M**, **Brasseur, Z**, **Brooks, IM**, **Calmer, R**, **Cassano, J**, **Castro, V**, **Chu, D**, **Costa, D**, **Cox, CJ**, **Creamean, J**, **Crewell, S**, **Dahlke, S**, **Damm, E**, **de Boer, G**, **Deckelmann, H**, **Dethloff, K**, **Dütsch, M**, **Ebell, K**, **Ehrlich, A**, **Ellis, J**, **Engelmann, R**, **Fong, AA**, **Frey, MM**, **Gallagher, MR**, **Ganzeveld, L**, **Gradinger, R**, **Graeser, J**, **Greenamyer, V**, **Griesche, H**, **Griffiths, S**, **Hamilton, J**, **Heinemann, G**, **Helmig, D**, **Herber, A**, **Heuzé, C**, **Hofer, J**, **Houchens, T**, **Howard, D**, **Inoue, J**, **Jacobi, HW**, **Jaiser, R**, **Jokinen, T**, **Jourdan, O**, **Jozef, G**, **King, W**, **Kirchgaessner, A**, **Klingebiel, M**, **Krassovski, M**, **Krumpen, T**, **Lampert, A**, **Landing, W**, **Laurila, T**, **Lawrence, D**, **Lonardi, M**, **Loose, B**, **Lüpkes, C**, **Maahn, M**, **Macke, A**, **Maslowski, W**, **Marsay, C**, **Maturilli, M**, **Mech, M**, **Morris, S**, **Moser, M**, **Nicolaus, M**, **Ortega, P**, **Osborn, J**, **Pätzold, F**, **Perovich, DK**, **Petäjä, T**, **Pilz, C**, **Pirazzini, R**, **Posman, K**, **Powers, H**, **Pratt, KA**, **Preußer, A**, **Quéléver, L**, **Radenz, M**, **Rabe, B**, **Rinke, A**, **Sachs, T**, **Schulz, A**, **Siebert, H**, **Silva, T**, **Solomon, A**, **Sommerfeld, A**, **Spreen, G**, **Stephens, M**, **Stohl, A**, **Svensson, G**, **Uin, J**, **Viegas, J**, **Voigt, C**, **von der Gathen, P**, **Wehner, B**, **Welker, JM**, **Wendisch, M**, **Werner, M**, **Xie, Z**, **Yue, F**. 2022. Overview of the MOSAiC expedition: Atmosphere. *Elementa: Science of the Anthropocene* **10**(1). DOI: http://dx.doi.org/10.1525/elementa.2021.00060.

Simpson, WR, **Brown, SS**, **Saiz-Lopez, A**, **Thornton, JA**, **von Glasow, R**. 2015. Tropospheric halogen chemistry: Sources, cycling, and impacts. *Chemical Reviews* **115**(10): 4035–4062. DOI: http://dx.doi.org/10.1021/cr5006638.

Simpson, WR, **Peterson, P**, **Frieß, U**, **Sihler, H**, **Lampel, J**, **Platt, U**, **Moore, C**, **Pratt, K**, **Shepson, P**, **Halfacre, J**, **Nghiem, S**. 2017. Horizontal and vertical structure of reactive bromine events probed by bromine monoxide MAX-DOAS. *Atmospheric Chemistry and Physics* **17**(15): 9291–9309. DOI: http://dx.doi.org/10.5194/acp-17-9291-2017.

Simpson, WR, **von Glasow, R**, **Riedel, K**, **Anderson, P**, **Ariya, P**, **Bottenheim, J**, **Burrows, J**, **Carpenter, LJ**, **Frieß, U**, **Goodsite, ME**, **Heard, D**, **Hutterli, M**, **Jacobi, HW**, **Kaleschke, L**, **Neff, B**, **Plane, J**, **Platt, U**, **Richter, A**, **Roscoe, H**, **Sander, R**, **Shepson, P**,

Sodeau, J, **Steffen, A**, **Wagner, T**, **Wolff, E.** 2007. Halogens and their role in polar boundary-layer ozone depletion. *Atmospheric Chemistry and Physics* **7**(16): 4375–4418. DOI: http://dx.doi.org/10.5194/acp-7-4375-2007.

Sitkiewicz, SP, **Rivero, D**, **Oliva-Enrich, JM**, **Saiz-Lopez, A**, **Roca-Sanjuán, D**. 2019. Ab *initio* quantum-chemical computations of the absorption cross sections of HgX_2 and HgXY (X, Y = Cl, Br, and I): Molecules of interest in the Earth's atmosphere. *Physical Chemistry Chemical Physics* **21**: 455–467. DOI: http://dx.doi.org/10.1039/C8CP06160B.

Skov, H, **Brooks, SB**, **Goodsite, ME**, **Lindberg, SE**, **Meyers, TP**, **Landis, MS**, **Larsen, MR**, **Jensen, B**, **McConville, G**, **Christensen, J**. 2006. Fluxes of reactive gaseous mercury measured with a newly developed method using relaxed eddy accumulation. *Atmospheric Environment* **40**(28): 5452–5463. DOI: http://dx.doi.org/10.1016/j.atmosenv.2006.04.061.

Skov, H, **Christensen, JH**, **Goodsite, ME**, **Heidam, NZ**, **Jensen, B**, **Wåhlin, P**, **Geernaert, G**. 2004. Fate of elemental mercury in the Arctic during atmospheric mercury depletion episodes and the load of atmospheric mercury to the Arctic. *Environmental Science & Technology* **38**(8): 2373–2382. DOI: http://dx.doi.org/10.1021/es030080h.

Skov, H, **Hjorth, J**, **Nordstrøm, C**, **Jensen, B**, **Christoffersen, C**, **Bech Poulsen, M**, **Baldtzer Liisberg, J**, **Beddows, D**, **Dall'Osto, M**, **Christensen, JH**. 2020. Variability in gaseous elemental mercury at Villum Research Station, Station Nord, in North Greenland from 1999 to 2017. *Atmospheric Chemistry and Physics* **20**(21): 13253–13265. DOI: http://dx.doi.org/10.5194/acp-20-13253-2020.

Slemr, F, **Angot, H**, **Dommergue, A**, **Magand, O**, **Barret, M**, **Weigelt, A**, **Ebinghaus, R**, **Brunke, EG**, **Pfaffhuber, KA**, **Edwards, G**, **Howard, D**, **Powell, J**, **Keywood, M**, **Wang, F**. 2015. Comparison of mercury concentrations measured at several sites in the Southern Hemisphere. *Atmospheric Chemistry and Physics* **15**(6): 3125–3133. DOI: http://dx.doi.org/10.5194/acp-15-3125-2015.

Sommar, J, **Wängberg, I**, **Berg, T**, **Gårdfeldt, K**, **Munthe, J**, **Richter, A**, **Urba, A**, **Wittrock, F**, **Schroeder, WH**. 2007. Circumpolar transport and air-surface exchange of atmospheric mercury at Ny-Ålesund (79° N), Svalbard, spring 2002. *Atmospheric Chemistry and Physics* **7**(1): 151–166. DOI: http://dx.doi.org/10.5194/acp-7-151-2007.

Song, S, **Selin, NE**, **Soerensen, AL**, **Angot, H**, **Artz, R**, **Brooks, S**, **Brunke, EG**, **Conley, G**, **Dommergue, A**, **Ebinghaus, R**, **Holsen, TM**, **Jaffe, DA**, **Kang, S**, **Kelley, P**, **Luke, WT**, **Magand, O**, **Marumoto, K**, **Pfaffhuber, KA**, **Ren, X**, **Sheu, GR**, **Slemr, F**, **Warneke, T**, **Weigelt, A**, **Weiss-Penzias, P**, **Wip, DC**, **Zhang, Q**. 2015. Top-down constraints on atmospheric mercury emissions and implications for global biogeochemical cycling. *Atmospheric Chemistry and Physics* **15**(12): 7103–7125. DOI: http://dx.doi.org/10.5194/acp-15-7103-2015.

Sprovieri, F, **Pirrone, N**, **Bencardino, M**, **D'Amore, F**, **Angot, H**, **Barbante, C**, **Brunke, EG**, **Arcega-Cabrera, F**, **Cairns, W**, **Comero, S**, **Diéguez, MDC**, **Dommergue, A**, **Ebinghaus, R**, **Feng, XB**, **Fu, X**, **Garcia, PE**, **Gawlik, BM**, **Hageström, U**, **Hansson, K**, **Horvat, M**, **Kotnik, J**, **Labuschagne, C**, **Magand, O**, **Martin, L**, **Mashyanov, N**, **Mkololo, T**, **Munthe, J**, **Obolkin, V**, **Ramirez Islas, M**, **Sena, F**, **Somerset, V**, **Spandow, P**, **Vardè, M**, **Walters, C**, **Wängberg, I**, **Weigelt, A**, **Yang, X**, **Zhang, H**. 2017. Five-year records of mercury wet deposition flux at GMOS sites in the Northern and Southern hemispheres. *Atmospheric Chemistry and Physics* **17**(4): 2689–2708. DOI: http://dx.doi.org/10.5194/acp-17-2689-2017.

Steen, AO, **Berg, T**, **Dastoor, AP**, **Durnford, DA**, **Hole, LR**, **Pfaffhuber, KA**. 2009. Dynamic exchange of gaseous elemental mercury during polar night and day. *Atmospheric Environment* **43**(25): 5604–5610. DOI: http://dx.doi.org/10.1016/j.atmosenv.2009.07.069.

Steenhuisen, F, **Wilson, S**. 2019. Development and application of an updated geospatial distribution model for gridding 2015 global mercury emissions. *Atmospheric Environment* **211**: 138–150. DOI: http://dx.doi.org/10.1016/j.atmosenv.2019.05.003.

Steenhuisen, F, **Wilson, SJ**. 2022. Geospatially distributed (gridded) global mercury emissions to air from anthropogenic sources in 2015. DataverseNL. DOI: http://dx.doi.org/10.34894/SZ2KOI.

Steffen, A, **Bottenheim, J**, **Cole, A**, **Douglas, TA**, **Ebinghaus, R**, **Friess, U**, **Netcheva, S**, **Nghiem, S**, **Sihler, H**, **Staebler, R**. 2013. Atmospheric mercury over sea ice during the OASIS-2009 campaign. *Atmospheric Chemistry and Physics* **13**(14): 7007–7021. DOI: http://dx.doi.org/10.5194/acp-13-7007-2013.

Steffen, A, **Bottenheim, J**, **Cole, A**, **Ebinghaus, R**, **Lawson, G**, **Leaitch, WR**. 2014. Atmospheric mercury speciation and mercury in snow over time at Alert, Canada. *Atmospheric Chemistry and Physics* **14**(5): 2219–2231. DOI: http://dx.doi.org/10.5194/acp-14-2219-2014.

Steffen, A, **Schroeder, W**, **Bottenheim, J**, **Narayan, J**, **Fuentes, JD**. 2002. Atmospheric mercury concentrations: Measurements and profiles near snow and ice surfaces in the Canadian Arctic during Alert 2000. *Atmospheric Environment* **36**(15): 2653–2661. DOI: http://dx.doi.org/10.1016/S1352-2310(02)00112-7.

Stephens, CR, **Shepson, PB**, **Steffen, A**, **Bottenheim, JW**, **Liao, J**, **Huey, LG**, **Apel, E**, **Weinheimer, A**, **Hall, SR**, **Cantrell, C**, **Sive, BC**, **Knapp, DJ**, **Montzka, DD**, **Hornbrook, RS**. 2012. The relative importance of chlorine and bromine radicals in the oxidation of atmospheric mercury at Barrow, Alaska. *Journal of Geophysical Research: Atmospheres* **117**(D14). DOI: http://dx.doi.org/10.1029/2011JD016649.

Subir, M, **Ariya, PA**, **Dastoor, AP**. 2011. A review of uncertainties in atmospheric modeling of mercury chemistry I. Uncertainties in existing kinetic parameters—Fundamental limitations and the importance of heterogeneous chemistry. *Atmospheric Environment* **45**(32): 5664–5676. DOI: http://dx.doi.org/10.1016/j.atmosenv.2011.04.046.

Subir, M, **Ariya, PA**, **Dastoor, AP**. 2012. A review of the sources of uncertainties in atmospheric mercury modeling II. Mercury surface and heterogeneous chemistry—A missing link. *Atmospheric Environment* **46**: 1–10. DOI: http://dx.doi.org/10.1016/j.atmosenv.2011.07.047.

Swanson, WF, **Holmes, CD**, **Simpson, WR**, **Confer, K**, **Marelle, L**, **Thomas, JL**, **Jaeglé, L**, **Alexander, B**, **Zhai, S**, **Chen, Q**, **Wang, X**, **Sherwen, T**. 2022. Comparison of model and ground observations finds snowpack and blowing snow aerosols both contribute to Arctic tropospheric reactive bromine. *Atmospheric Chemistry and Physics* **22**(22): 14467–14488. DOI: http://dx.doi.org/10.5194/acp-22-14467-2022.

Tewari, M, **Chen, F**, **Wang, W**, **Dudhia, J**, **LeMone, MA**, **Gayno, G**, **Wegiel, J**, **Cuenca, RH**. 2004. Implementation and verification of the unified Noah land surface model in the WRF model. 20th Conference on Weather Analysis and Forecasting/16th Conference on Numerical Weather Prediction, Seattle, WA.

Theys, N, **Van Roozendael, M**, **Hendrick, F**, **Yang, X**, **De Smedt, I**, **Richter, A**, **Begoin, M**, **Errera, Q**, **Johnston, PV**, **Kreher, K**, **De Mazière, M**. 2011. Global observations of tropospheric BrO columns using GOME-2 satellite data. *Atmospheric Chemistry and Physics* **11**(4): 1791–1811. DOI: http://dx.doi.org/10.5194/acp-11-1791-2011.

Toyota, K, **McConnell, JC**, **Lupu, A**, **Neary, L**, **McLinden, CA**, **Richter, A**, **Kwok, R**, **Semeniuk, K**, **Kaminski, JW**, **Gong, SL**, **Jarosz, J**, **Chipperfield, MP**, **Sioris, CE**. 2011. Analysis of reactive bromine production and ozone depletion in the Arctic boundary layer using 3-D simulations with GEM-AQ: Inference from synopticscale patterns. *Atmospheric Chemistry and Physics* **11**(8): 3949–3979. DOI: http://dx.doi.org/10.5194/acp-11-3949-2011.

Toyota, K, **McConnell, JC**, **Staebler, RM**, **Dastoor, AP**. 2014. Air–snowpack ex-change of bromine, ozone and mercury in the springtime Arctic simulated by the 1-D model PHANTAS—Part 1: In-snow bromine activation and its impact on ozone. *Atmospheric Chemistry and Physics* **14**(8): 4101–4133. DOI: http://dx.doi.org/10.5194/acp-14-4101-2014.

Travnikov, O, **Angot, H**, **Artaxo, P**, **Bencardino, M**, **Bieser, J**, **D'Amore, F**, **Dastoor, A**, **De Simone, F**, **Diéguez, MDC**, **Dommergue, A**, **Ebinghaus, R**, **Feng, XB**, **Gencarelli, CN**, **Hedgecock, IM**, **Magand, O**, **Martin, L**, **Matthias, V**, **Mashyanov, N**, **Pirrone, N**, **Ramachandran, R**, **Read, KA**, **Ryjkov, A**, **Selin, NE**, **Sena, F**, **Song, S**, **Sprovieri, F**, **Wip, D**, **Wängberg, I**, **Yang, X**. 2017. Multi-model study of mercury dispersion in the atmosphere: Atmospheric processes and model evaluation. *Atmospheric Chemistry and Physics* **17**(8): 5271–5295. DOI: http://dx.doi.org/10.5194/acp-17-5271-2017.

Wagner, DN, **Shupe, MD**, **Cox, C**, **Persson, OG**, **Uttal, T**, **Frey, MM**, **Kirchgaessner, A**, **Schneebeli, M**, **Jaggi, M**, **Macfarlane, AR**, **Itkin, P**, **Arndt, S**, **Hendricks, S**, **Krampe, D**, **Nicolaus, M**, **Ricker, R**, **Regnery, J**, **Kolabutin, N**, **Shimanshuck, E**, **Oggier, M**, **Raphael, I**, **Stroeve, J**, **Lehning, M**. 2022. Snowfall and snow accumulation during the MOSAiC winter and spring seasons. *The Cryosphere* **16**(6): 2373–2402. DOI: http://dx.doi.org/10.5194/tc-16-2373-2022.

Wagner, T, **Leue, C**, **Wenig, M**, **Pfeilsticker, K**, **Platt, U**. 2001. Spatial and temporal distribution of enhanced boundary layer BrO concentrations measured by the GOME instrument aboard ERS-2. *Journal of Geophysical Research: Atmospheres* **106**(D20): 24225–24235. DOI: http://dx.doi.org/10.1029/2000JD000201.

Wang, S, **McNamara, SM**, **Moore, CW**, **Obrist, D**, **Steffen, A**, **Shepson, PB**, **Staebler, RM**, **Raso, ARW**, **Pratt, KA**. 2019. Direct detection of atmospheric atomic bromine leading to mercury and ozone depletion. *Proceedings of the National Academy of Sciences* **116**(29): 14479–14484. DOI: http://dx.doi.org/10.1073/pnas.1900613116.

Wesely, M. 1989. Parameterization of surface resistances to gaseous dry deposition in regional-scale numerical models. *Atmospheric Environment* **23**(6): 1293–1304. DOI: http://dx.doi.org/10.1016/0004-6981(89)90153-4.

Wiedinmyer, C, **Akagi, SK**, **Yokelson, RJ**, **Emmons, LK**, **Al-Saadi, JA**, **Orlando, JJ**, **Soja, AJ**. 2011. The Fire INventory from NCAR (FINN): A high resolution global model to estimate the emissions from open burning. *Geoscientific Model Development* **4**(3): 625–641. DOI: http://dx.doi.org/10.5194/gmd-4-625-2011.

Wiedinmyer, C, **Kimura, Y**, **McDonald-Buller, EC**, **Emmons, LK**, **Buchholz, RR**, **Tang, W**, **Seto, K**, **Joseph, MB**, **Barsanti, KC**, **Carlton, AG**, **Yokelson, R**. 2023. The Fire Inventory from NCAR version 2.5: An updated global fire emissions model for climate and chemistry applications. *EGUsphere.* DOI: http://dx.doi.org/10.5194/egusphere-2023-124.

Wild, O, **Zhu, X**, **Prather, MJ**. 2000. Fast-J: Accurate simulation of in- and below-cloud photolysis in tropospheric chemical models. *Journal of Atmospheric Chemistry* **37**(3): 245–282. DOI: http://dx.doi.org/10.1023/A:1006415919030.

Xu, L, **Zhang, Y**, **Tong, L**, **Chen, Y**, **Zhao, G**, **Hong, Y**, **Xiao, H**, **Chen, J**. 2020. Gas-particle partitioning of atmospheric reactive mercury and its contribution to particle bound mercury in a coastal city of the Yangtze River Delta, China. *Atmospheric Environment* **239**: 117744. DOI: http://dx.doi.org/10.1016/j.atmosenv.2020.117744.

Yang, X, **Blechschmidt, AM**, **Bognar, K**, **McClure-Begley, A**, **Morris, S**, **Petropavlovskikh, I**, **Richter, A**,

Skov, H, **Strong, K**, **Tarasick, D**, **Uttal, T**, **Vestenius, M**, **Zhao, X**. 2020. Pan-Arctic surface ozone: Modelling vs measurements. *Atmospheric Chemistry and Physics* **20**(4): 15937–15967. DOI: http://dx.doi.org/10.5194/acp-20-15937-2020.

Yang, X, **Frey, MM**, **Rhodes, RH**, **Norris, SJ**, **Brooks, IM**, **Anderson, PS**, **Nishimura, K**, **Jones, AE**, **Wolff, EW**. 2019. Sea salt aerosol production via sublimating wind-blown saline snow particles over sea ice: Parameterizations and relevant microphysical mechanisms. *Atmospheric Chemistry and Physics* **19**(13): 8407–8424. DOI: http://dx.doi.org/10.5194/acp-19-8407-2019.

Yang, X, **Pyle, JA**, **Cox, RA**. 2008. Sea salt aerosol production and bromine release: Role of snow on sea ice. *Geophysical Research Letters* **35**(16). DOI: http://dx.doi.org/10.1029/2008GL034536.

Yang, X, **Pyle, JA**, **Cox, RA**, **Theys, N**, **Van Roozendael, M**. 2010. Snow-sourced bromine and its implications for polar tropospheric ozone. *Atmospheric Chemistry and Physics* **10**(16): 7763–7773. DOI: http://dx.doi.org/10.5194/acp-10-7763-2010.

Zaveri, RA, **Easter, RC**, **Fast, JD**, **Peters, LK**. 2008. Model for simulating aerosol interactions and chemistry (MOSAIC). *Journal of Geophysical Research: Atmospheres* **113**(D13). DOI: http://dx.doi.org/10.1029/2007JD008782.

Zhang, L, **Blanchard, P**, **Gay, DA**, **Prestbo, EM**, **Risch, MR**, **Johnson, D**, **Narayan, J**, **Zsolway, R**, **Holsen, TM**, **Miller, EK**, **Castro, MS**, **Graydon, JA**, **Louis, VLS**, **Dalziel, J**. 2012. Estimation of speciated and total mercury dry deposition at monitoring locations in eastern and central North America. *Atmospheric Chemistry and Physics* **12**(9): 4327–4340. DOI: http://dx.doi.org/10.5194/acp-12-4327-2012.

Zhang, L, **Wright, LP**, **Blanchard, P**. 2009. A review of current knowledge concerning dry deposition of atmospheric mercury. *Atmospheric Environment* **43**(37): 5853–5864. DOI: http://dx.doi.org/10.1016/j.atmosenv.2009.08.019.

Zhang, P, **Zhang, Y**. 2022. Earth system modeling of mercury using CESM2—Part 1: Atmospheric model CAM6-Chem/Hg v1.0. *Geoscientific Model Development* **15**(9): 3587–3601. DOI: http://dx.doi.org/10.5194/gmd-15-3587-2022.

Zilker, B, **Richter, A**. 2023. TROPOMI tropospheric vertical column densities of BrO in the Arctic region for spring 2020. Zenodo. DOI: http://dx.doi.org/10.5281/zenodo.7711532.

How to cite this article: Ahmed, S, Thomas, JL, Angot, H, Dommergue, A, Archer, SD, Bariteau, L, Beck, I, Benavent, N, Blechschmidt, A-M, Blomquist, B, Boyer, M, Christensen, JH, Dahlke, S, Dastoor, A, Helmig, D, Howard, D, Jacobi, H-W, Jokinen, T, Lapere, R, Laurila, T, Quéléver, LLJ, Richter, A, Ryjkov, A, Mahajan, AS, Marelle, L, Pfaffhuber, KA, Posman, K, Rinke, A, Saiz-Lopez, A, Schmale, J, Skov, H, Steffen, A, Stupple, G, Stutz, J, Travnikov, O, Zilker, B. 2023. Modelling the coupled mercury-halogen-ozone cycle in the central Arctic during spring. *Elementa: Science of the Anthropocene* 11(1). DOI: https://doi.org/10.1525/elementa.2022.00129

Domain Editor-in-Chief: Jody W. Deming, University of Washington, Seattle, WA, USA

Guest Editor: Matthew Shupe, Cooperative Institute for Research in Environmental Sciences, University of Colorado Boulder, Boulder, CO, USA

Knowledge Domain: Ocean Science

Part of an Elementa Special Feature: The Multidisciplinary Drifting Observatory for the Study of Arctic Climate (MOSAiC)

Published: May 11, 2023 **Accepted:** March 17, 2023 **Submitted:** October 11, 2022

ELEMENTA Science of the Anthropocene

Elem Sci Anth is a peer-reviewed open access journal published by University of California Press.

OPEN ACCESS